ALL-FIBER FREQUENCY COMB EMPLOYING A SINGLE WALLED CARBON NANOTUBE SATURABLE ABSORBER FOR OPTICAL FREQUENCY METROLOGY IN NEAR INFRARED

by

JINKANG LIM

B. S., Kwangwoon University, 2005

AN ABSTRACT OF A DISSERTATION

submitted in partial fulfillment of the requirements for the degree

DOCTOR OF PHILOSOPHY

Department of Physics
College of Arts and Science

KANSAS STATE UNIVERSITY
Manhattan, Kansas

2011

Abstract

Optical frequency combs produced by mode-locked fiber lasers are us eful tools for high precision frequency metrology and molecular spectroscopy in a robust and portable format. We have specifically investigated erbium doped fiber mode-locked lasers that use single-walled carbon nanotubes as a saturable absorber. We have, for the first time, developed and phase-stabilized a carbon nanotube fiber laser (CNFL) frequency comb. The carbon nanotube saturable absorber, which was fabricated using an optically driven deposition method, permits a high repetition frequency (>150 MHz) since an optical nonlinearity of fibers is not used for mode-locking. The CNFL comb combined with a parabolic pulse erbium doped fiber amplifier (EDFA) has shown a compact, robust, and cost-effective supercontinuum source. The amplified pulse from the parabolic pulse EDFA was compressed with a hollow-core photonic bandgap fiber, which produced a wave-breaking-free pulse with an all-fiber set-up. The stabilized comb has demonstrated a fractional instability of 1.2×10^{-11} at 1 sec averaging time, the reference-limited instability. We have performed optical frequency metrology with the CNFL comb and have measured an optical frequency, P(13) which is a molecular overtone transition of C_2H_2. The measured frequency has shown a good agreement with the known value within an uncertainty of 10 kHz.

In order to extend the application of the CNFL comb such as multi-heterodyne dual comb spectroscopy, we have investigated the noise of the CNFL comb and particularly, the broad carrier envelope offset frequency (f_0) linewidth of the CNFL comb. The primary noise source is shown to be white amplitude noise on the oscillator pump laser combined with the sensitivity of the mode-locked laser to pump power fluctuations. The control bandwidth of f_0 was limited by the response dynamics of the CNFL comb. The significant reduction of comb noise has been observed by implementing a phase-lead compensation to extend control bandwidth of the comb and by reducing the pump relative intensity noise simultaneously. Therefore the f_0 linewidth has been narrower from 850 kHz to 220 kHz. The integrated phase noise for the f_0 lock is 1.6 radians from 100 Hz to 102 kHz.

ALL-FIBER FREQUENCY COMB EMPLOYING A SINGLE WALLED CARBON NANOTUBE SATURABLE ABSORBER FOR OPTICAL FREQUENCY METROLOGY IN NEAR INFRARED

by

JINKANG LIM

B. S., Kwangwoon University, 2005

A DISSERTATION

submitted in partial fulfillment of the requirements for the degree

DOCTOR OF PHILOSOPHY

Department of Physics
College of Arts and Science

KANSAS STATE UNIVERSITY
Manhattan, Kansas

2011

Approved by:

Major Professor
Brian R. Washburn

Copyright

Abstract

Optical frequency combs produced by mode-locked fiber lasers are useful tools for high precision frequency metrology and molecular spectroscopy in a robust and portable format. We have specifically investigated erbium doped fiber mode-locked lasers that use single-walled carbon nanotubes as a saturable absorber. We have, for the first time, developed and phase-stabilized a carbon nanotube fiber laser (CNFL) frequency comb. The carbon nanotube saturable absorber, which was fabricated using an optically driven deposition method, permits a high repetition frequency (>150 MHz) since an optical nonlinearity of fibers is not used for mode-locking. The CNFL comb combined with a parabolic pulse erbium doped fiber amplifier (EDFA) has shown a compact, robust, and cost-effective supercontinuum source. The amplified pulse from the parabolic pulse EDFA was compressed with a hollow-core photonic bandgap fiber, which produced a wave-breaking-free pulse with an all-fiber set-up. The stabilized comb has demonstrated a fractional instability of 1.2×10^{-11} at 1 sec averaging time, the reference-limited instability. We have performed optical frequency metrology with the CNFL comb and have measured an optical frequency, P(13) which is a molecular overtone transition of C_2H_2. The measured frequency has shown a good agreement with the known value within an uncertainty of 10 kHz.

In order to extend the application of the CNFL comb such as multi-heterodyne dual comb spectroscopy, we have investigated the noise of the CNFL comb and particularly, the broad carrier envelope offset frequency (f_0) linewidth of the CNFL comb. The primary noise source is shown to be white amplitude noise on the oscillator pump laser combined with the sensitivity of the mode-locked laser to pump power fluctuations. The control bandwidth of f_0 was limited by the response dynamics of the CNFL comb. The significant reduction of comb noise has been observed by implementing a phase-lead compensation to extend control bandwidth of the comb and by reducing the pump relative intensity noise simultaneously. Therefore the f_0 linewidth has been narrower from 850 kHz to 220 kHz. The integrated phase noise for the f_0 lock is 1.6 radians from 100 Hz to 102 kHz.

Table of Contents

List of Figures

List of Tables

Acknowledgements

First of all, I am very grateful to my advisor Dr. Brian Washburn for giving me an opportunity to study in such an exciting research area. In fact, I did not fully understand how fantastic my research is when I started to work. I have been very happy during my graduate school years at Kansas State University because I have been able to work with him. He is a passionate researcher, a great mentor, and also my role model as a scientist. I remember that when I was new in our lab, he tried to stop by the lab everyday and help me do research and carefully listen to my stories. The conversation with him is always pleasant and encourages me. Without his guidance and support, this thesis could never be completed. I also thank Dr. Kristan Corwin. I remember that she had a brilliant solution or a great idea for every problem in our research. She was always willing to help me with her distinguished insight. I would like to thank Dr. Tillman. I was able to learn a lot of technical skills from his research experiences. He is also a good guitarist and I like listening to his guitar playing. I would love to thank Kevin Knabe, Andrew Jones, Shun Wu, Chenchen Wang, and Rajesh Kadel. Kevin has shown a good leadership as a senior student. He often invited us to his house and cooked delicious food. I like the hotdog he cooked in his yard. Andrew is nice and humble but is hard-working researcher in our lab. I really enjoyed talking and hanging out with him in CLEO 2010 at San Jose and will not forget it. Shun does always her best in the research which stimulates me to work harder. Chenchen is very positive and enjoys her research. She may think the research is similar to play soccer. Rajesh Kadel is my good friend in the lab. I also thank Rajesh Thapa, Daniel Nickel, Daniel Moeder, May Ebbeni, and Will Hageman for working together.

I deeply appreciate my classmates 2005 and friends for giving me good memories during my school years. I would like to thank He Wang who is my best friend. He has helped and encouraged me in many ways. I especially thank Hannah S. Kim. Her wise encouragements have really touched me. I have to thank department and JRM staffs for supporting me to do high quality research. There is no doubt that my family was a big and warm support for me.

I do thank my committee members and outside chair who are Dr. Chang, Dr. Corwin, Dr. Chikan, and Dr. Morcos for helping and serving me for my Ph. D. thesis. They were willing to

accept my defense schedule in spite of their busy schedule. I would like to thank them again in heart.

Finally, I thank my Lord for His unfailing love to me through my whole life. He is the light shining my way, so that I do not stumble and fail now and forever.

Dedication

To my parents

Seungrock Lim and Jeongsook Kim

Chapter 1 - Introduction

1.1 Precision measurement and optical frequency metrology

For more than a century, the precision spectroscopy of atoms and molecules has allowed physicists to study their structures and to discover and prove the laws of quantum mechanics. For instance, the value of the Rydberg constant and the 1S-Lamb shift [1-3] in the hydrogen atom have been able to be precisely measured. Furthermore, the precise measurement of time and frequency (*i. e*. optical frequency metrology [4, 5]) has been a critical tool to determine fundamental constants such as the fine structure constant and the ratio of Planck's constant to electron mass (h/m_e), and to realize standards for time and frequency [6, 7]. The recent research has claimed that the temporal variation of the fine structure constant could be $(-1.6 \pm 2.3)\times 10^{-17}$ / *year* [8, 9]. Since the value of the speed of light in vacuum was precisely defined to be 299,792,458 ms^{-1} in 1983 by the Conférence Générale des Poids et Measures (CGPM), the accuracy of a frequency measurement can also be exactly transferred to a length measurement by the dispersion relation.

1.1.1 Optical frequency metrology before optical frequency comb

The advent of very narrow-linewidth and tunable lasers and techniques for Doppler-free spectroscopy in the early 1970s had a remarkable impact on precision spectroscopy. Physicists are able to trap atoms, molecules, or single ions and to observe extremely narrow optical resonances with resolutions ranging from 10^{-13} to 10^{-15} and therefore they predicted that the line center of such an optical resonance might be measured in accuracy of a few parts in 10^{18} [10, 11]. However, the physicist has been faced with the problem to measure the optical frequency precisely because most spectroscopic experiments have been relying on a measurement of optical wavelengths instead of frequencies. Therefore, it was difficult to avoid the distortion in the geometric wavefront, diffraction corrections, and imperfections of the optics, so that the accuracy measurement from wavelengths was limited to a few parts in 10^{10} with a laboratory-sized wavelength interferometer [4]. In order to achieve the optical resonance frequency accurately, it is required to measure the frequency rather than its wavelength because frequency

(or time: time is derived from frequency by counting the oscillations) can be essentially measured with much more precision than any other physical quantity. The accuracy of measurable time was increased as shown in Figure 1.1. Obviously the more oscillations increase the clock accuracy and this is simply because a higher oscillation frequency divides time scale into smaller pieces. Since 1967, the definition of the second has currently been the duration of 9,192,631,770 periods of the microwave radiation produced by the transition between two hyperfine levels of the ground state of the ^{133}Cs atom. However, the highly precise measurement of frequencies was restricted to the microwave frequency (up to 100 GHz) domain because there is no electronic counter to measure such fast oscillations in the range of several hundreds of terahertz (1 THz = 10^{12} Hz).

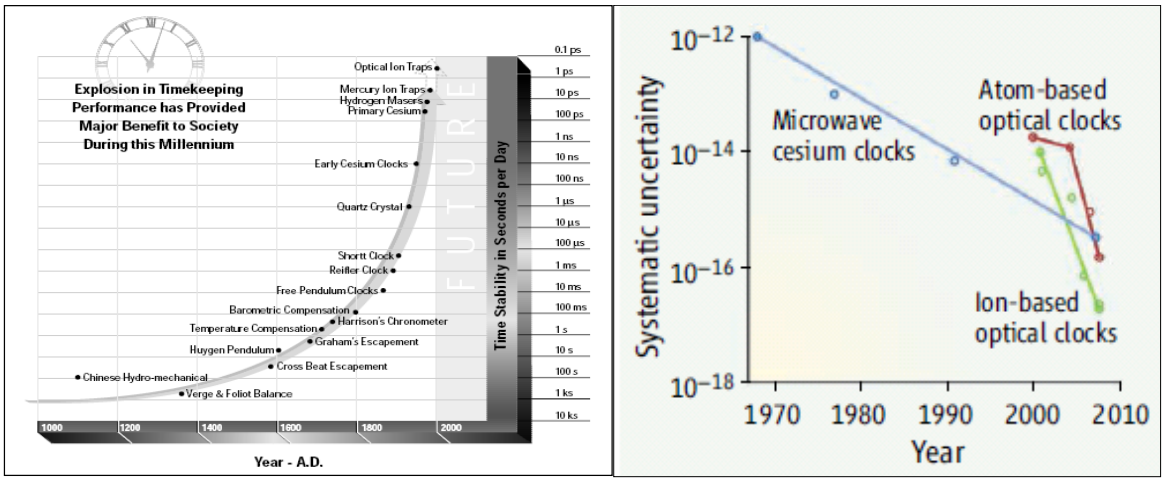

Figure 1.1 (a) Progress of clock accuracy before the optical clock Reproduced from Ref [149]. (b) Atom or ion based optical clock improved the systematic uncertainty than that of a Cs microwave atomic clock, whose measurement was realized with the stabilized optical frequency comb. Reproduced from Ref. [12].

The earlier method to address this issue was to make phase-coherent harmonic frequency chains [13, 14]. The schematic set-up realized at Physikalisch Technische Bundesanstalt (PTB) is depicted in Figure 1.2. The set-up was developed to measure the frequency of a CW laser stabilized to laser-cooled Ca (f_{Ca} ~ 456 THz). To measure the optical frequency, the Cs frequency standard at 9.2 GHz that is a microwave frequency was extended to the visible part of electromagnetic spectrum using the chain. The Cs clock defines the frequency at the lower end of the chain and then the higher harmonics are generated using nonlinear diode mixers, crystals, and other nonlinear devices. In addition, phase-locked loops (PLL) are required for each step. These

configurations made the harmonic frequency chain complicated and required substantial resources and effort to build and operate, and therefore only limited research laboratories afforded to do that measurement. Particularly, its complexity potentially increased measurement errors and the system was able to last only for minutes. Another problem of this method is that the harmonic chains are designed for measuring only one single optical frequency. Difference laboratories had to make different frequency chain set-ups and therefore this method was not universal to measure the optical frequencies until a new approach (the optical frequency comb) came into reach. The frequency measurement accuracy of the harmonic frequency chain by PTB was a few hundreds hertz out of an optical frequency about 400 THz and its fractional accuracy ($\Delta f_{Ca} / f_{Ca}$) in the range of 10^{-13} [5, 15].

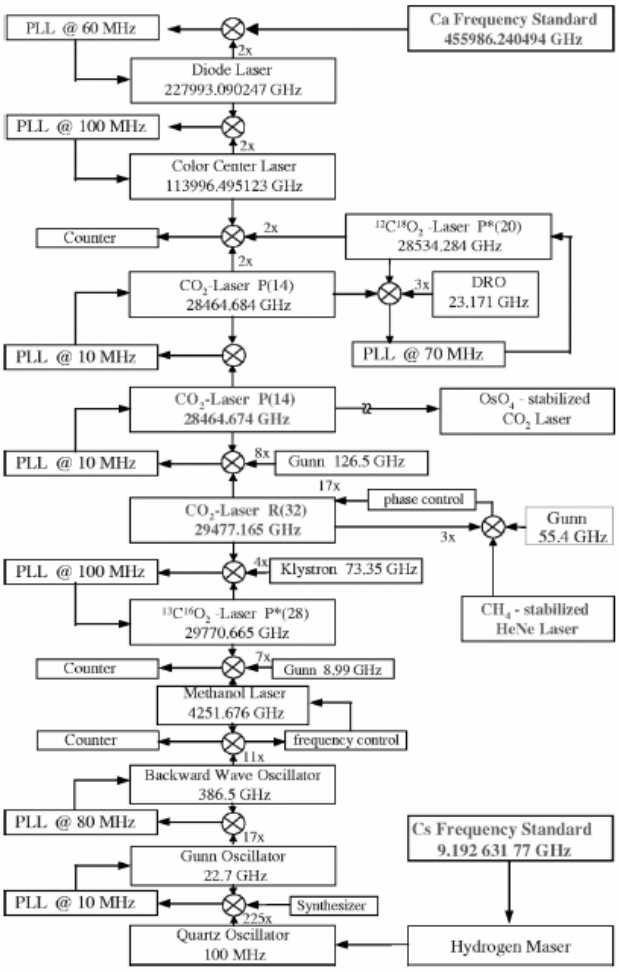

Figure 1.2 A harmonic frequency chain. The chain was started from a Cs frequency standard and went to the 456 THz, Ca optical frequency standard at PTB. Reproduced form Ref. [15].

1.1.2 The advent of an octave spanning self-referenced frequency comb

Advances in ultrafast optics and laser stabilization techniques have brought a new research tool for making precision frequency measurements called the frequency comb. The frequency comb is a set of equally spaced spectral lines produced by a femtosecond mode-locked laser (See details in Section 1.1.3). Since the fully stabilized self-referenced frequency comb was introduced to the research field in 2000 [16], it has revolutionized time and frequency measurements in precision spectroscopy and optical frequency metrology for the last decade with its superior stability and accuracy. The frequency comb has also been applied to many other scientific research areas as a reliable instrument [17-26].

Most important advantage of the frequency comb is a number of comb teeth acting like many CW laser sources over a broad bandwidth, possessing an extremely narrow linewidth, and those spectral lines are controllable by the well-established electronic feedback. Therefore, an optical frequency within the spectral gain bandwidth can be measured by beating the comb against the optical frequency we want to measure. As a result, they create a measurable radio frequency (RF) signal. The stabilized frequency comb provides a number of separable narrow linewidth optical frequencies in the broad spectral range and therefore the frequency comb is an ideal tool for measuring optical frequencies generated from atoms and molecules by transforming optical frequencies to detectable RF signals. We will explain the optical frequency measurement in detail in Section 1.1.4 and in Chapter 6. At the current stage, frequency combs cover many spectral ranges from the extreme ultraviolet (EUV) [27] to the mid-infrared [28] making them useful for many possible applications. At the same time, the frequency comb has also made a transition from a laboratory instrument to a field-usable and turn-key research device [128].

In summary, the invention of the stabilized frequency comb is due to the development of femtosecond mode-locked laser sources, elaborate laser stabilization techniques, and nonlinear and fiber optics research as illustrated in Figure 1.3.

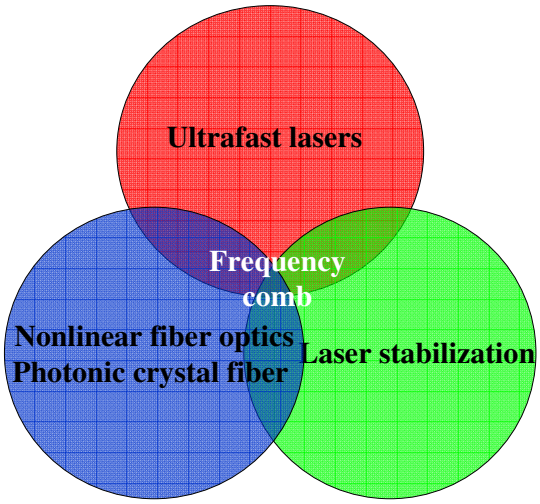

Figure 1.3 Frequency comb research. The research in general includes development of a femtosecond mode-locked laser source, elaborate laser stabilization techniques, and nonlinear and fiber optics research.

1.1.2.1 Historical review of the frequency comb

The initial conception of the frequency comb was developed in the 1970's and the first comb has already been experimentally used by T. W. Hänsch and colleagues at Stanford University. They used the comb produced from a pulsed dye laser to do spectroscopy and discovered that its linewidth was extremely narrow for exciting the sodium 4d fine-structure [29]. However, the first fully stabilized frequency comb was introduced with the beginning of the 21st century. A common question raised, as address in the Nobel lecture of T. W. Hänsch, is "why did it take so long?" [127]. The answer comes with the maturity of ultrafast laser science, laser stabilization techniques, and the availability of highly nonlinear fibers needed for phase stabilization. The invention of Kerr lens mode-locking in 1990 made it possible to produce ultrashort pulses of sub-100 fs with the high pulse energy [30]. This allowed for the high peak intensity which facilitated nonlinear optics research. Those researches mutually reacted and brought significant improvements in both fields with the laser stabilized techniques that have been well established through the decades for optical frequency metrology.

The first fully self-referenced stabilized frequency comb project was proposed by T. W. Hänsch in 1997. In the project he first tried to verify the interference of a white light source generated from CaF_2 crystal using a Ti:Sapphire mode-locked laser in order to implement it to an octave spanning self-referenced frequency comb. Meanwhile, J. K. Ranka and colleagues

presented the micro-structured fiber generating an octave spanning spectral source at the post-deadline session in Conference for Laser and Electro-Optics (CLEO) 1999 [31] and this offered the opportunity to develop the first fully self-referenced stabilized frequency comb using a Ti:Sapphire mode-locked laser to J. Hall and his colleagues at JILA in Boulder, Colorado. After this first demonstration of the frequency comb, there has been an explosion of research in this area to apply it to optical frequency metrology, precision spectroscopy, optical clock work, and more. The first fiber based self-referenced frequency comb using an Er^{3+} doped fiber mode-locked laser was also demonstrated in 2003 by B. R. Washburn, N. R. Newbury and their team at the National Institute for Standards and Technology (NIST) in Boulder, Colorado [32]. The excellent contributions of the frequency comb to the fundamental sciences and applied fields were recognized and two contributors, T. W. Hänsch and J. Hall won one half of the Nobel Prize in 2005. The frequency comb has dramatically simplified the optical frequency measurement and we will discuss it in the following sections.

1.1.3 Properties of the optical frequency comb

In order to understand how to use the optical frequency comb for optical frequency metrology, precision spectroscopy, and other possible applications, we should first grasp the properties of optical frequency comb. In this section, we will discuss the key to understanding the frequency comb and then explain how to measure the optical frequency using the frequency comb. In addition, we will briefly mention the current applications of the frequency comb in other fields in following sections.

1.1.3.1 Time and frequency domain description

A mode locked laser produces a train of pulses whose repetition frequency is determined by the laser's cavity length. Due to the difference between the group velocity (v_g) and phase velocity (v_p) of pulses in the cavity, in order words, the pulse envelope travels with the group velocity but the carrier travels with the phase velocity, therefore the phase slip is introduced to each pulse. Specifically, the phase shift per pulse ($\Delta\varphi$) will be $\Delta\varphi = (1/v_g - 1/v_p)\ \omega_c L_{cav}$, where L_{cav} is the round-trip length of the laser cavity and ω_c is the carrier angular frequency.

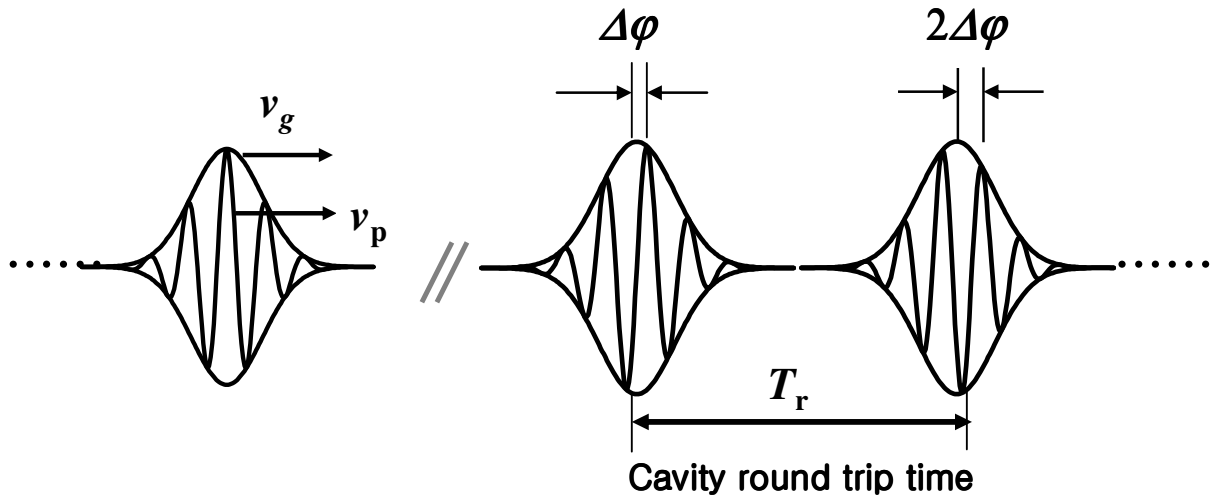

Figure 1.4 A train of pulses generated from a mode locked laser. The periodicity of pulse is defined by laser cavity length. T_r is the cavity round trip time of a pulse. The pulse envelope propagates with the group velocity (v_g) but the carrier frequency propagates with the phase velocity (v_p). The pulse repetition time is determined by the length of cavity and a pulse has a phase slip between the envelope and the carrier frequency due to the difference between the phase and the group velocity in the cavity.

In Figure 1.2, a pulse train is depicted from a mode-locked laser. The pulse is generally generated from a mode locked laser. The pulse round trip time (T_r) is defined by $T_r = 2L\, n/c$ for a linear cavity or $T_r = p\, n/c$ for a ring cavity, where L is a linear cavity length, p is a ring cavity length, n is the refractive index, and c is the speed of light. Mathematically, the train of pulses is described by the convolution of a pulse and infinite series of Dirac delta functions (known as Shah or comb function) in the time domain. Therefore the infinite pulses, $\tilde{E}(t)$ (the tilde was used to stand for the complex electric field) is represented using a convolution between the complex electric field of a single transform-limited pulse, $\tilde{A}(t)$ and the comb function as shown below

$$\tilde{E}(t) = \tilde{A}(t) \otimes \sum_{m=-\infty}^{\infty} \delta(t - m/f_r)\, e^{-im\Delta\varphi},\ m\text{=integer} \tag{1.1}$$

$$\text{and } \tilde{A}(t) = A_0(t)\, e^{i(\omega_c t + \varphi_0)}, \tag{1.2}$$

where $A_0(t)$ is the envelope of a pulse in the time domain, ω_c is the carrier angular frequency ($\omega = 2\pi\nu$, *where* ν *is the frequency*), f_r is the repetition frequency defined by $1/T_r$, φ_0 is the initial temporal phase, and $\Delta\varphi$ is the phase slip introduced by difference between the phase and group velocity which is called the carrier envelope offset (CEO) phase. Every adjacent pulse has the phase increment by $\Delta\varphi$ in the time domain. If we take the Fourier transform of the train of pulses, $\tilde{E}(t)$,in order to look at it in the frequency domain then,

$$\mathrm{FT}\{\tilde{E}(t)\} = \mathrm{FT}\{A_0(t)e^{i(\omega_c t+\varphi_0)} \otimes \sum_{m=-\infty}^{\infty} \delta(t - m/f_r)\, e^{-im\Delta\varphi}\}$$

$$= \mathrm{FT}\{A_0(t)e^{i(\omega_c t+\varphi_0)}\} \times \mathrm{FT}\{\delta(t - m/f_r)\, e^{-im\Delta\varphi}\}$$

$$\boxed{\tilde{E}(\omega) = e^{i\varphi_0} A_0(\omega - \omega_c) \sum_{m=-\infty}^{\infty} \delta(\omega - 2\pi(mf_r + f_0))} \qquad (1.3)$$

where FT stands for the Fourier Transformation. By definition of the Fourier transform of a train of pulses, it becomes a series of regularly spaced frequencies. $A_0(\omega-\omega_c)$ is the pulse envelope in the frequency domain. The f_0 is called the CEO frequency defined by

$$f_0 = \frac{\Delta\varphi}{2\pi} f_r, \qquad (1.4)$$

This set of regularly spaced frequencies is called the frequency comb. The n^{th} comb tooth is determined by the simple algebraic equation, $\nu_n = n f_r + f_0$, where n is the mode number (integer) and the frequency comb is shifted by the CEO frequency. The optical frequency comb is depicted in Figure 1.3. As we can see here, the actual number of comb teeth is limited by the optical gain bandwidth of the mode locked laser and n is typically on the order of 10^5-10^6 for optical frequencies.

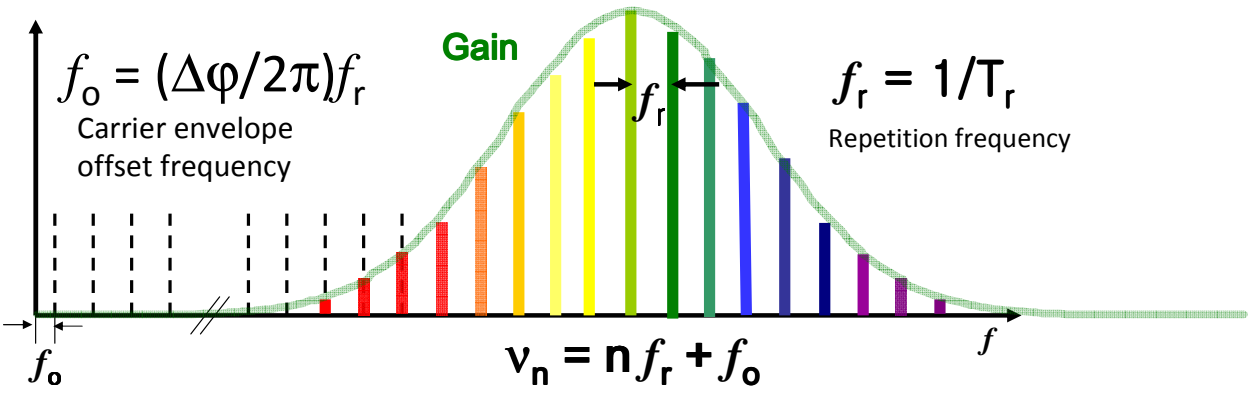

Figure 1.5 Optical frequency comb. f_r: repetition frequency, f_0: carrier envelope offset frequency. The n^{th} comb tooth is determined by the simple algebraic equation $\nu_n = n f_r + f_0$ where n is the mode number. The available comb teeth are determined by the gain of the mode locked laser.

Note that generally measurement instruments show the intensity or called the irradiance which is a time average of the square of the electric field per unit area. Therefore, the temporal intensity and phase of the pulse are by definition

$$I(t) \equiv \frac{1}{2} c\varepsilon_0 n \tilde{E}(t)\tilde{E}(t)^* \text{ and } \varphi(t) = \arctan[\mathrm{Im}\{\tilde{E}(t)\}/\mathrm{Re}\{\tilde{E}(t)\}], \quad (1.5)$$

where * denotes the complex conjugate. Meanwhile the spectral intensity and phase of the pulse are given by

$$I(\omega) \equiv \frac{1}{2} c\varepsilon_0 n \tilde{E}(\omega)\tilde{E}(\omega)^* \text{ and } \varphi(\omega) = \arctan[\mathrm{Im}\{\tilde{E}(\omega)\}/\mathrm{Re}\{\tilde{E}(\omega)\}], \quad (1.6)$$

respectively.

1.1.3.2 Coherence of the optical frequency comb

The coherence of optical frequency comb was observed by measuring the cross correlation between the j^{th} pulse and the $(j+2)^{th}$ pulse, which has shown an interference pattern. The relation between the relative phase ($\Delta\varphi$) and the CEO frequency divided by the repetition

frequency is linear as shown in Figure1.6 (b). The phase between two pulses has shown the linear relationship as we expected in Eq. (1.3)

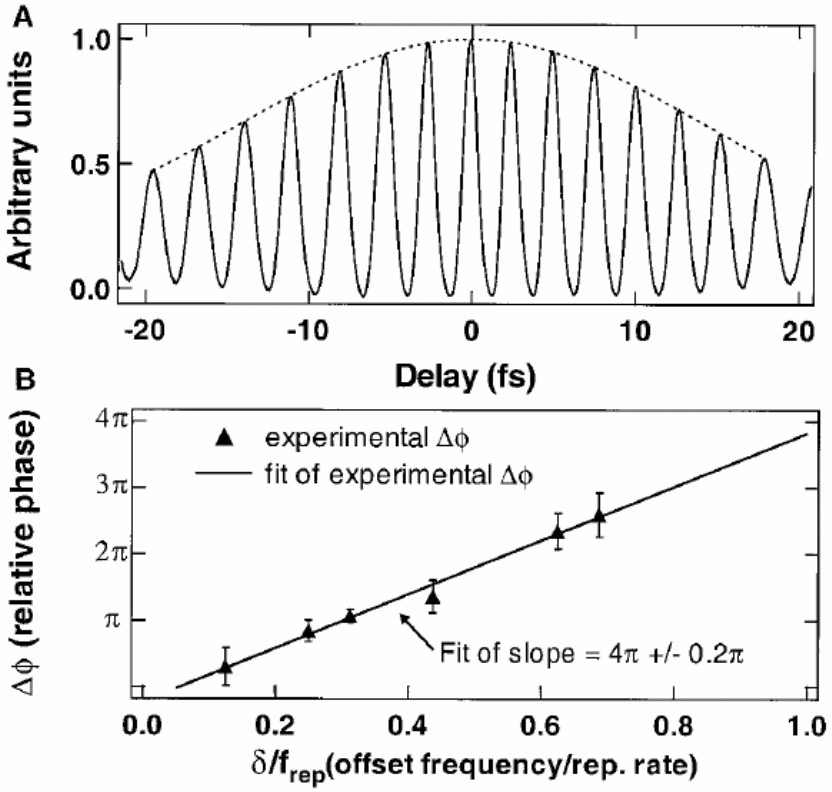

Figure 1.6 Correlation results. (a) Typical cross correlation (solid line) between the j^{th} pulse and the $(j+2)^{th}$ pulse along with a fit of the correlation envelope (dashed line). (b) Plot of the relative phase versus the offset frequency (normalized to the pulse repetition rate). Reproduced from Ref. [16].

1.1.3.3 Linewidth of the optical frequency comb

In theory, the lineshapes of the frequency comb teeth are delta functions corresponding to the constructive interference of infinite number of pulses. This can be readily proven using the Fourier transform theory in the previous sections. We introduce, however, a simple analogy to understand the linewidth of the comb. This gives much more intuitive picture about the comb linewidth. Table 1.1 shows the similarity between the grating equation and the frequency comb. The grating equation can be understood as a phase array produced by *N* regularly spaced holes which create a spatial distribution. Likewise the frequency comb is a frequency distribution generated by *N* equally spaced pulses in the time domain.

	Grating equation	Frequency comb
Number	Opening holes (N_h)	Pulses (N_p)
Phase angle (δ)	$\delta = 2\pi/\lambda(d\sin\theta)$ d: distance between adjacent holes	$\delta = \omega T$ T: repetition rate
Constructive interference	When $\delta = 0, 2\pi, 4\pi, \ldots$	
Linewidth	$\sim\lambda/N_h d$	$\sim 2\pi/N_p T$

Table 1.1 Analogy between a grating equation and a train of pulses.

As seen in Table 1.1, the linewidth is proportional to $1/N_p$, where N_p is the number of pulses. Figure 1.7 shows the relationship between N_p and the corresponding linewidth. One can clearly see that the linewidth becomes narrower when the N_p increases.

In practice, the comb teeth have a finite linewidth originating from a variety of noise sources including quantum and technical noise. The noise causes the pulse-to-pulse timing jitter so that the pulse-to-pulse interval is not regular. The details for the linewidth and noise will be discussed in Chapter 5. The research has shown that the subhertz instrument limited linewidth is possible for a fiber comb [33] and this low noise of the comb is preserved even after experiencing the extreme nonlinearity of the supercontinuum generation [34].

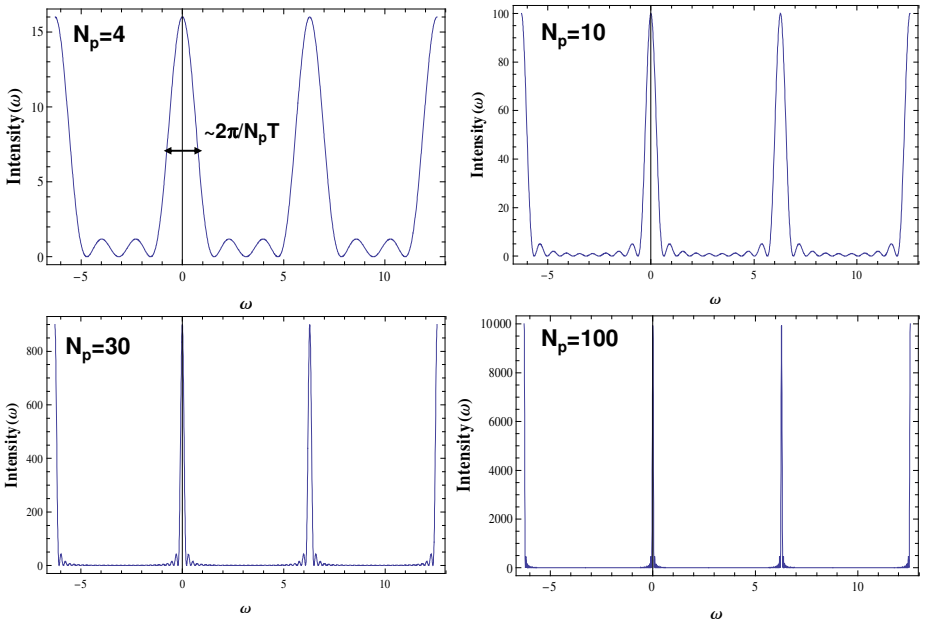

Figure 1.7 The linewidth of frequency comb with increasing the number of pulses (N_p). More pulses make the comb teeth narrower and the linewidth is proportional to $1/N_p$.

1.1.4 Optical frequency metrology with the optical frequency comb

As we reviewed in Section 1.1.1, the precision optical frequency measurement was a very complex process before the self-referenced optical frequency comb was introduced. Contrary to the harmonic frequency chains, the optical frequency comb offers very easy, accurate, and reliable measurement with much less complexity over a wider frequency range. Once you know how straight forward this approach is, you will definitely thank the optical frequency comb. The frequency comb can be stabilized to either microwave frequency references or optical frequency references. The stabilized frequency comb generates a bunch of stabilized and regularly spaced CW lasers within a broad spectral range with intrinsically narrow linewidths and these act like a frequency ruler, so that any optical frequency within the comb bandwidth can be measured as a RF beatnote signal by heterodyne-beating the optical frequency against a tooth of the comb. Thereafter the optical frequency can be calculated from the RF beatnote and the comb's mode number using a simple algebraic equation. The mode number can be directly found with a high resolution wave-meter or can be experimentally calculated from the Vernier method [35]. For both cases, the ambiguity in the number of comb modes is reduced by using the high repetition frequency comb. The other advantage of the high repetition frequency comb is that it allows more power per each comb tooth, and therefore the detection sensitivity is increased. Consequently, the high repetition frequency comb increases the resolving power for optical frequency measurements. The details will be explained in Chapter 6. The accuracy of the frequency measurement using a Ti:Sapphire laser frequency comb done by Th. Udem *et al.* was tens of hertz for the laser-cooled Hg^+ and the fractional uncertainty was on the order of 10^{-14} range [17].

1.1.5 Applications of the frequency comb up to date

The stabilized frequency comb is still being widely used in many fundamental and applied research areas such as optical frequency metrology, precision spectroscopy, optical clock work, [20, 36, 37] light detection and ranging (LIDAR), [38] optical waveform synthesis, [39-41] and astrophysical spectrograph [25, 42, 43]. The optical frequency comb also has significant impacts on the time domain applications such as timing synchronization, coherent control [44-49], atto-second science, [50-52] and more.

1.1.5.1 Direct frequency comb spectroscopy

One of interesting and straightforward applications of the frequency comb is direct frequency comb spectroscopy (DFCS) because the optical frequency comb possesses a large number of stabilized comb teeth which have allowed for performing high precision and broad spectral bandwidth spectroscopy in parallel. Since the first experiment using DFCS to study ^{87}Rb [53], the DFCS soon extended its application to molecular detections [22]. The use of DFCS has efficiently provided the simultaneous measurement of many transitions of several different molecules. The frequency comb was able to be efficiently coupled into the high finesse optical cavity due to its periodic pulse structure, and the DFCS combined with the optical cavity brought much more sensitive detection of atoms and molecules. The approach has found many potential applications in studying broadband molecular spectroscopy, atmospheric chemistry, pollution analysis, human breath analysis [54], and more with the rapid and sensitive detection over a broad spectral range.

1.1.5.2 Optical clock work

With the significant development of laser spectroscopy in the 1980s, physicists were able to trap atoms or single ions, such as Rb, Ca, CH_4, Hg^+, I_2, Sr^+, Yb^+, and In^+ [55-59], and observe very narrow resonances. Measuring the optical frequency using the harmonic frequency chain, they seriously started to think about an optical atomic clock. However, before the optical frequency comb was introduced, the harmonic frequency chain never came into reach for continuous operation even for minutes, and eventually the optical frequency comb provided the physicists a means of building a reliable all-optical atomic clock. The frequency comb provided the missing gap between microwave frequency standards and optical frequency standards.

For the optical clock work [20, 60], the frequency comb is stabilized to the optical frequency produced from laser-cooled atoms or single ions, and the accuracy and stability is transferred to the optical frequency comb. The research has shown that the performance of the optical atomic clock is limited not by the frequency comb but by technical difficulties during the photo-detection process [61]. As a result, the tracking fractional instability of the frequency comb, meaning how well the frequency comb follows the reference, was an order of 10^{-16} at 1 sec averaging time (τ) [62] an even better at longer gate times [63] but the actual stability transferred from optical to microwave signals was at the $1 \times 10^{-14}\ \tau^{-1}$ level at 1 sec averaging

time. Recently the instability of 5.2×10^{-17} at 1000 s averaging time was reported by T. Rosenband *et al.* in 2008 which is two orders of magnitude better than the current Cs microwave atomic frequency standard. A better definition of time is crucial not only for fundamental science but also for our daily life such as accurate *GPS* navigation and timing synchronization in the telecommunication system.

1.1.5.3 Astrophysical spectrograph

Astronomers use the periodic Doppler frequency shift of a binary system [64, 65] to detect stars and planets. Until recent, the wavelength calibration of the measured periodic Doppler shift has been done typically with thorium-argon lamps or iodine absorption cells but the resolution of those spectrographs was not enough to detect an earth-like planet. The stabilized optical frequency comb filtered with a Fabry-Pérot cavity has been developed as the calibration source for higher resolution spectrographs. C. -H. Li *et al.* [25] have recently reported that the resolution of the spectrograph has been improved by an order of magnitude by optical frequency comb in the near infrared wavelength compared to the previous method.

1.2 Thesis problem statement

Early frequency combs used for optical frequency metrology, precision spectroscopy, and applied research were based primarily on Ti:Sapphire laser comb because of the excellent properties of Ti:Sapphire crystal as a laser gain material, a low noise performance, the available high optical power, and the broad spectral bandwidth. However, it is still not only expensive and bulky but also requiring experiences and technical skills to operate it. Furthermore, Ti:Sapphire lasers do not cover the fiber-optic telecommunication wavelength region near 1550 nm (C-band). Over the most recent years, significant efforts and developments have been done to make the frequency comb a field-usable research instrument in the areas such as the calibration of frequencies in fiber-optic telecommunication and molecular spectroscopy. In that sense, the fiber laser comb has increased its attractiveness. The fiber laser frequency comb has already shown its stability and excellent performance comparable to the Ti:Sapphire laser comb [19] as shown in Figure 1.8 and the below the quantum-limit phase noise operation [33, 34].

Although the Ti:Sapphire laser comb is still an excellent comb source, the fiber-based frequency comb has important advantages because it can be a compact and turn-key integrated device. This direction seems to be natural to widely use the frequency comb not only in precision metrology laboratories but also in research laboratories or industry requiring frequency measurement or calibration, and the Er^{3+} doped fiber laser frequency comb has already been commercialized since 2005 by Menlo system [128]. In addition to that, it provides environmental and thermal robustness and cost-effectiveness, and Er^{3+} doped fiber lasers are able to cover the bandwidth of Ti:Sapphire comb (at 790 nm) by frequency-doubling it. In particular, it has shown better long term stability and easier signal dissemination using the existing fiber-optic telecommunication channels than that of solid state lasers, making fiber laser combs more suitable for optical clock work.

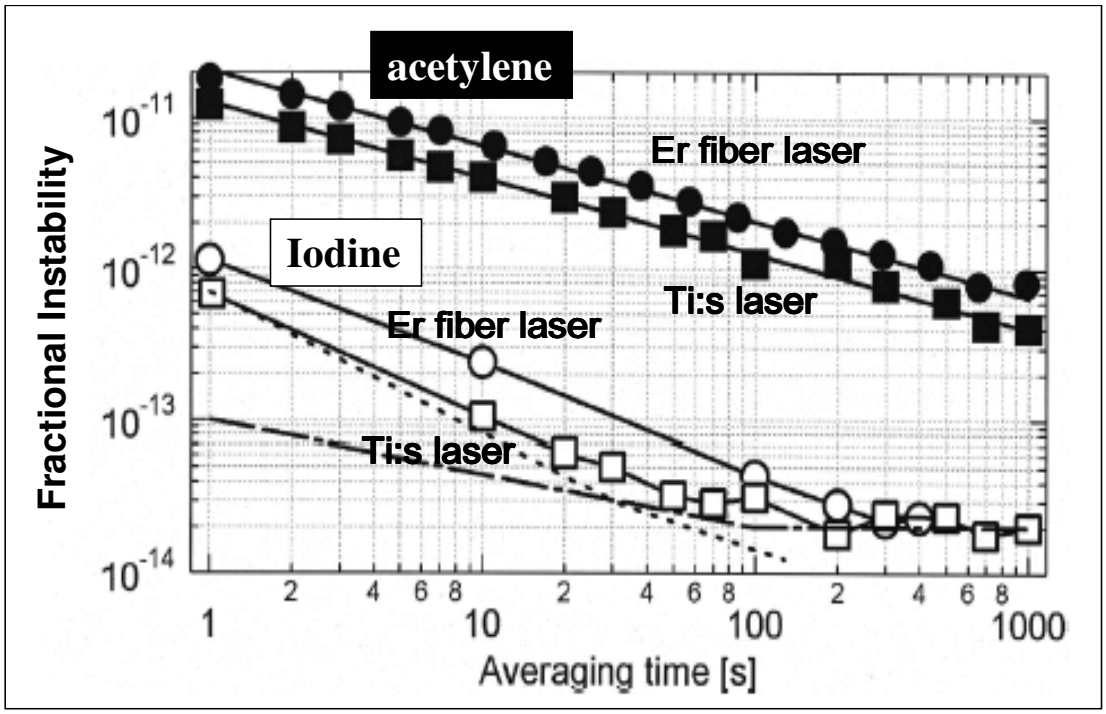

Figure 1.8 Fractional instabilities of the beat notes between the comb and the stabilized lasers. Filled circles: acetylene measured with the turnkey fiber system; filled squares: acetylene measured with the Ti:Sapphire system; open circles: iodine measured with the turnkey fiber system; open squares, iodine measured with the Ti:Sapphire laser; Dotted line: fractional instability of the Hydrogen maser used as a frequency reference for all the measurements; dashed–dotted line: Fractional instability [129] between two iodine-stabilized lasers of the same type. Reproduced from Ref. [19].

Our research has been performed based on the objectives to realize a compact and turn-key frequency comb with high repetition frequency (> 100MHz) in the near infrared wavelength range for optical frequency metrology both in fundamental academic research and in commercial industry research such as the calibration of frequencies in the fiber-optic telecommunication and navigation system. It will further be extended to precision molecular spectroscopy that is ongoing project in our laboratory.

For the purpose, we investigated Er^{3+} doped fiber lasers using a single walled carbon nanotube saturable absorber named as the CNFL in this thesis. The use of single walled carbon nanotubes (SWCNT) as a saturable absorber allowed for the compact, simple, and cost-effective laser cavity design with the high repetition frequency [66, 67] compared to the previously existing Er^{3+} doped fiber lasers using fiber nonlinearity as a saturable absorber. Furthermore, the CNFL has shown the environmentally stable mode-locking and self-sustainability.

Even though CNFL has a variety of advantages to make the compact and cost-effective frequency comb source, the noise and instability of the CNFL and its ability to serve as a reliable frequency comb source have not been verified before. Therefore we have scrutinized the properties of the CNFL frequency comb for precision near-IR frequency metrology and spectroscopy. In this thesis, we have investigated the noise of the CNFL frequency comb and have demonstrated the phase-stabilization of the CNFL frequency comb referenced by a microwave frequency standard and have reported its stability for the first time [68]. Furthermore we were able to measure an optical frequency of C_2H_2 molecular overtone transition, P(13), using our CNFL frequency comb within a uncertainty of 10 kHz [69].

1.3 Importance of this thesis

This is the first fully stabilized frequency comb to a microwave frequency reference based on a CNFL to our best knowledge. Therefore this thesis has a position as a guide for designing and understanding properties of a CNFL frequency comb. The important steps to generate the stabilized CNFL frequency comb were discussed, which included the noise and stability of the CNFL frequency comb and further noise reduction methods. In addition, an application of the CNFL frequency comb for optical frequency metrology in the conventional

band (C-band) was introduced, so that the thesis covers the CNFL frequency comb from its fabrication to the application. In general, the comb for optical frequency metrology is more useful if it has a high repetition frequency enhancing the resolving power between the comb teeth, and the comb that has a high repetition frequency with a high average power allows for greater power per comb tooth, which increases the detecting sensitivity of the comb. The CNFL frequency comb combined with a high power parabolic pulse erbium doped fiber amplifier successfully provided those keys. Moreover, it has shown cost-effectiveness, compactness in size, excellent mode-locking sustainability, power efficiency, and self-stating operation. Finally, the CNFL frequency comb can be stabilized for more than six hours without any active temperature control. These results allow for making a transition of the frequency comb into a field-usable turn-key research instrument for optical frequency metrology in near infrared and more applications.

1.4 Thesis outline

The structure of the rest of this thesis is arranged to help the reader understand how to generate and apply a low noise phase-stabilized fiber laser frequency comb. In Chapter 2, femtosecond Er^{3+} doped mode-locked fiber lasers and saturable absorbers are discussed because they are sources of the frequency comb. The important properties of fibers, passive mode locking mechanisms using fiber nonlinearity, and the design strategies to make an Er^{3+} doped fiber mode-locked laser are discussed. In Chapter 3, the single walled carbon nanotube (SWCNT) saturable absorber is discussed to make a high repetition frequency mode-locked fiber Er^{3+} doped CNFL. The physical mechanism and properties of SWCNT saturable absorber are discussed. Ultrashort pulse amplification using a dispersion managed EDFA is studied in Chapter 4. The pulse amplification is required to generate a supercontinuum spectrum with which to detect the carrier envelope offset frequency (f_0) by the f to $2f$ self-referencing method. The details for detecting f_0 are explained in Chapter 5. By detecting f_r and f_0, all degrees of freedom to control the frequency comb are obtained since the n^{th} comb tooth is defined by a simple algebraic equation, $\nu_n = n f_r + f_0$. For the next steps, the stabilization of the comb, its noise, and possible noise reduction methods are also discussed in Chapter 5. The stabilization is

required for our use in optical frequency metrology. The optical frequency of an overtone vibration transition of C_2H_2 was measured using the CNFL frequency comb. The results are shown in Chapter 6. Finally, this thesis will be concluded with research summary and future work using the CNFL frequency combs such as multi-heterodyne dual comb spectroscopy and mid-IR comb.

Chapter 2 - Mode-locked Er^{3+} Doped Fiber Lasers

2.1 Introduction

Mode-locked lasers [70] are a source of the frequency comb. They produce a train of periodic pulses in the time domain and its spectral content is the frequency comb in the frequency domain. Initially, many research on the frequency comb have been done with a group of crystal lasers such as the Ti:Sapphire laser and the Cr:Forsterite laser but the mode-locked fiber lasers quickly has caught up to them with advantages which are making them attractive. They provide an easy, portable, and turn-key operation with different emission wavelengths and these properties extend the potential of the frequency comb to the field-usable research instrument.

In this thesis, we studied mode-locked Er^{3+} doped fiber lasers for making a stabilized frequency comb for optical frequency metrology in the near infrared (1550 nm). A variety of mode-locking mechanisms can be used to obtain a train of ultrashort pulses including fiber nonlinearities and semiconductor saturable absorbers such as a semiconductor saturable absorber mirror (SESAM) and single walled carbon nanotubes. In this chapter, we will discuss keys to building and understanding the femtosecond mode-locked fiber laser which will include important properties of fibers, saturable absorbers for the laser passive mode locking, and mode-locked fiber laser design strategies in practical research.

2.2 Properties of optical fibers as building blocks for mode-locked fiber lasers

Single mode optical fibers are fundamental building blocks for mode-locked fiber lasers and amplifiers. In this section, the important properties of optical fibers such as guiding mechanism, dispersion, and nonlinearity are considered to design the mode-locked fiber lasers and amplifiers.

2.2.1 Light guiding in step index fibers

Fibers are excellent waveguides and therefore the light can be propagated with very low loss in the fibers (0.2 dB/km). There are two main categories of the optical fiber waveguides that we have used in this thesis. Primarily we use the step index fiber which guides the light by total internal reflection (TIR). The higher reflective index in the core than that of cladding creates the TIR in the optical fiber. The loss of the fused silica step index fiber commonly used in the telecommunication area is only a 0.2 dB/km at 1550 nm. The other group used is the photonic crystal fiber (PCF) or photonic bandgap fiber (PBGF) which is using Bragg scattering based upon two dimensional periodic crystal structure. This group of fibers will be discussed in Chapter 4. Figure 2.1 illustrates the propagating mechanisms of the step index fiber using TIR.

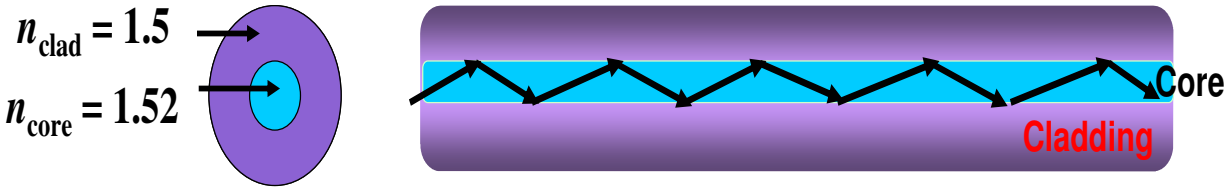

Figure 2.1 A step index fiber: the light is guided by the total internal reflection due to the higher reflective index of the core.

2.2.2 Waveguide modes in a step index fiber and single mode operation

The fiber waveguide can support a number of transverse electric and magnetic field modes depending on the *V* number or called normalized frequency defined as

$$V = \frac{2\pi a}{\lambda}(n_{core}^2 - n_{clad}^2)^{1/2} = \frac{2\pi a}{\lambda} NA\,, \tag{2.1}$$

where a is the core radius and n_{core} and n_{clad} are refractive indices for the core and the cladding respectively. The *NA* is the numerical aperture defined as $NA = [(n_{\text{core}})^2 - (n_{\text{clad}})^2]^{1/2}$. There are a number of waveguide modes depending on the *V* number and the larger *V* number corresponds to the more number of modes which increases with roughly $V^2/2$.

The modes in a step index fiber can have both electric field and magnetic field to the propagation direction (z-axis) simultaneously and therefore they are not transverse electric (TE)

or transverse magnetic (TM) modes but hybrid modes (HE or EH). However, the modes in the step index fiber we are interested in are linearly polarized (LP) modes and these waves have TE and TM field characteristics. These LP modes exist when the normalized index difference (Δ) is much less than 1 ($\Delta << 1$), where Δ is defined as $\Delta = (n_{core}-n_{clad})/n_{core}$. These types of step index fibers are called weakly guiding fibers. For all practical fibers used in our research, the difference between n_{core} and n_{clad} is very small and therefore $\Delta << 1$ so that the existing modes can be confined to the LP modes. The numerical expression of LP modes is that

$$\mathrm{E}_{\mathrm{LP}}(r,\varphi,z,t) = E_{lm}(r,\varphi)\exp[i(\omega t - \beta_{lm} z)], \tag{2.2}$$

where $E_{lm}(r, \varphi)$ represents the propagation of a transverse electric field distribution along propagation axis z and β_{lm} is the effective wavevector at the given $E_{lm}(r,\varphi)$ pattern. Because of the boundary conditions and cylindrical symmetry of fiber-waveguides, the modes can be characterized by two integers, l and m. The lowest LP mode we are interested in is the LP_{01} (fundamental mode) described in Figure 2.2.

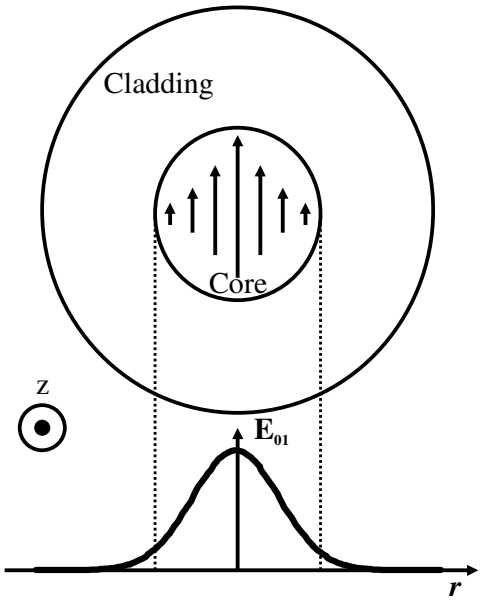

Figure 2.2 The electric field distribution of the fundament linearly polarized (LP_{01}) mode. The electric filed on both edges is due to the evanescent coupling of the electric field between the core and cladding. Reproduced from Ref. [145].

An interesting property of the step index fiber is the evanescent wave in the cladding regime as shown in Figure 2.2. This evanescent wave decays exponentially along the radius. The decay constant (α) can be derived from fiber parameters.

$$\alpha = \frac{2\pi n_{clad}}{\lambda}\left[\left(\frac{n_{core}}{n_{clad}}\right)^2 \sin^2\theta_i - 1\right]^{1/2} \approx \frac{2\pi}{\lambda}\left({n_{core}}^2 - {n_{clad}}^2\right)^{1/2} = \frac{V}{a} \tag{2.3}$$

where θ_i is the incident beam angle to the fiber and when the beam is parallel to z direction, it is 90^o. When $\theta_i = 90^o$, $\alpha = V/a$. Where V is the normalized frequency we defined earlier (Eq. 2.3). Therefore the actually electric field distribution in a step index fiber, called the mode field diameter (MFD), is larger than the fiber core size by $2a/V$.

In order to make a mode locked laser using fibers, the single mode operation is required because higher order modes not only create loss but also generate the additional inter-modal dispersion preventing the laser from mode-locking. The criterion for the single mode operation in the step index fiber is determined by the V number and more specifically $V_{cut\text{-}off} = 2.405$. For example, the Corning SMF-28e possessing $a = 4.1$ μm and $NA = 0.12$ has a cut-off wavelength at ~1280 nm. Therefore at the wavelength below 1280 nm, the light could be guided in multi-modes, which is not desirable both for making a mode-locked laser and for sending information through telecommunication channels.

2.2.4 Dispersion and nonlinearity of fibers

Understanding of fiber dispersion and nonlinearity is important for designing mode-locked fiber lasers and amplifiers. In this section, the origin of dispersion and nonlinearity produced by fibers and their effects on ultrashort pulses are discussed.

2.2.4.1 Group velocity dispersion

A pulse propagating in fiber experiences significant dispersion due to the interaction with fibers and the refractive index of fused silica fibers ($n_{\text{silica}} \sim 1.45$ at 1550 nm) is larger than air ($n_{\text{air}} \sim 1.0$). The speed of light in a medium is c/n, where c is the speed of light in vacuum and n is the refractive index of the medium. This is called the phase velocity and defined as $v_p = c/n$. In reality, the pulse or wave packet propagates in fibers with the group velocity defined as

$$v_g = \frac{d\omega}{dk}, \tag{2.4}$$

Particularly in vacuum, the group velocity is equal to the phase velocity. Because the refractive index has the wavelength dependence, the dispersion relation ($\omega = vk$) is represented by

$$\omega = vk = \left[\frac{c}{n(\lambda)}\right]\frac{2\pi}{\lambda}, \tag{2.5}$$

where k is the wave-vector. Therefore the group velocity in the medium is

$$v_{g,medium} = \frac{d\omega}{dk} = \frac{c}{n - \lambda\frac{dn}{d\lambda}} = \frac{c}{N_g}, \tag{2.6}$$

where N_g is the group index, the ratio of the vacuum velocity of light to the group velocity in the medium, defined as $N_g = n - \lambda(dn/d\lambda)$. The wavelength dependence of $n(\lambda)$ in the medium can be determined by the Sellmeier equation which is defined as

$$n(\lambda) = \sqrt{1 + \sum_{j=1}^{m}\frac{B_j\lambda^2}{\lambda^2 - C_m^2}} \approx \sqrt{1 + \frac{B_1\lambda^2}{\lambda^2 - C_1^2} + \frac{B_2\lambda^2}{\lambda^2 - C_2^2} + \frac{B_3\lambda^2}{\lambda^2 - C_3^2}}, \tag{2.7}$$

The coefficients depend on the medium. The host medium of the fibers commonly used is fused silica. The $n(\lambda)$ and its group velocity can be calculated based on the Sellmeier equation. The refractive index, $n(\lambda)$, and the group index are shown below. The Sellmeier coefficients for the fused silica are B_1=0.6961663, B_2=0.4079426, B_3=0.8974794, C_1=0.00467914826, C_2=0.135120631, and C_3=9.79340025 [130].

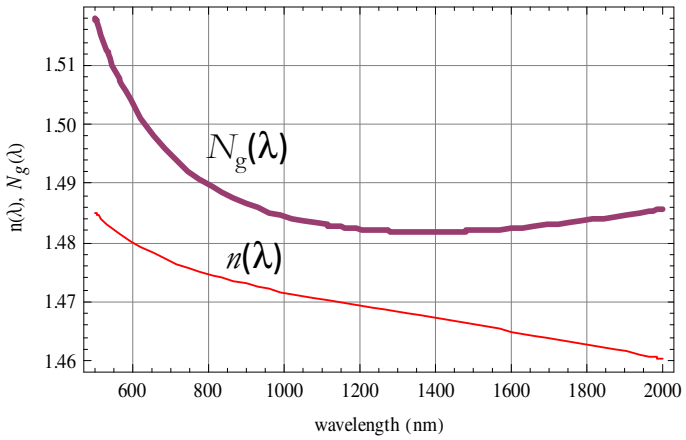

Figure 2.3 Refractive index, $n(\lambda)$ of fused silica glass in red and the group index $N_g(\lambda)$ in purple as a function of wavelength.

Material group velocity dispersion

The propagation constant, β in the medium is defined as $\beta(\omega) = n(\omega)\, k_0$, where k_0 is the propagation vector in vacuum. Now we will discuss the dispersion of fibers. The $\beta(\omega)$ can be expanded by the Taylor series which is the sum of polynomials. Therefore,

$$\beta(\omega) = \beta_0 + \beta_1(\omega-\omega_c) + \frac{1}{2}\beta_2(\omega-\omega_c)^2 + \frac{1}{6}\beta_3(\omega-\omega_c)^3 + \sum_m \frac{1}{m!}\beta_m(\omega-\omega_c)^m,$$

where $\beta_1 = \left(\frac{\partial\beta(\omega)}{\partial\omega}\right)_{\omega=\omega_c}$, $\beta_2 = \left(\frac{\partial^2\beta(\omega)}{\partial\omega^2}\right)_{\omega=\omega_c}$, $\beta_3 = \left(\frac{\partial^3\beta(\omega)}{\partial\omega^3}\right)_{\omega=\omega_c}$, and $\beta_m = \left(\frac{\partial^m\beta(\omega)}{\partial\omega^m}\right)_{\omega=\omega_c}$. β_1 is defined as $1/v_g$. β_2, called the second order dispersion or the group velocity dispersion (GVD), plays an important role in pulse broadening but as you see in the equation above, the higher order terms become significant as the spectral bandwidth increases. ω_c is the carrier angular frequency. The β coefficients are rewritten with the refractive index. For example, β_1 and β_2 can be expressed as

$$\begin{aligned}\beta_1 &= \frac{N_g}{c} = \frac{1}{c}(n + \omega\frac{dn}{d\omega}),\\ \beta_2 &= \frac{1}{c}(2\frac{dn}{d\omega} + \omega\frac{d^2n}{d\omega^2}).\end{aligned} \tag{2.8}$$

Therefore dispersions can be computed from the Sellmeier equation.

In Figure 2.4, the β_2 curve (Red) has a zero dispersion wavelength (λ_0) point at ~1370 nm (1.3 fs^{-1} in the angular frequency unit). At this point, the dispersion is minimized and therefore the pulse can propagate without a significant dispersion effect. From the zero dispersion wavelength point, the higher angular frequency (or lower wavelength) side has positive values and the lower angular frequency (or higher wavelength) side has negative values. Commonly the positive β_2 is called the positive GVD and the negative β_2 is called the negative GVD. For the positive GVD, the shorter wavelengths ($\lambda<\lambda_0$) travel slower than the longer wavelength ($\lambda>\lambda_0$) and for the negative GVD, the longer wavelengths travel slower than the shorter wavelengths. Generally, the fiber manufacturer provides the $D(\lambda)$ values rather than β_2 and it is related to β by the following equation,

$$D(\lambda) \equiv \frac{1}{c}\frac{dN_g}{d\lambda} = -\frac{2\pi c}{\lambda^2}\frac{d^2\beta}{d\omega^2}. \tag{2.9}$$

For numerically calculation discussed in Chapter 4, the GVD in unit of β_2 (fs^2/nm) is used. Therefore the conversion has to be made.

Waveguide dispersion

Different types of dispersion from the material dispersion exist in the single mode step index fiber such as waveguide dispersion (D_w). The waveguide dispersion is quantified by the following equation,

$$D_w = -\frac{n_{clad}\Delta}{c\lambda} V \frac{d^2(Vb)}{dV^2}, \tag{2.10}$$

where b is the normalized propagation constant defined as $b = \frac{(\beta/k) - n_{clad}}{n_{core} - n_{clad}}$ [131]. The effect of waveguide dispersion modifies the total dispersion (D_T) and therefore the total dispersion is the sum of them.

$$D_T = D_m + D_w . \tag{2.11}$$

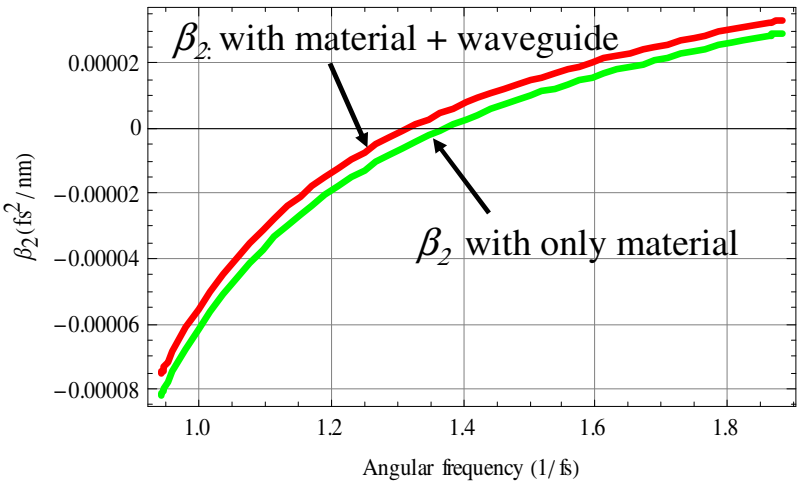

Figure 2.4 The group velocity dispersion (β_2) of the fused silica fiber. It has a zero dispersion wavelength at ~1370 nm in Green. The waveguide dispersion changes the total dispersion. The D and β are related by Eq. (2.9)

In practice, the waveguide dispersion is used to change the total dispersion. The fiber dispersion can be tuned by changing the geometry of the fiber structure. The total dispersion curves are shown in Figure 2.4 and the added waveguide dispersion shifts the total dispersion.

Dispersion length

We can define a useful quantity for dispersion during the pulse propagation in fibers, defined as

$$L_D \equiv \frac{T_0^2}{|\beta_2|}. \tag{2.12}$$

This is known as the dispersion length (L_D), where T_0 is the initial pulse width. The physical meaning of the dispersion length is that for a Gaussian pulse, the pulse becomes broadened by a factor of $\sqrt{2}$ when the pulse propagates by L_D. This equation implies that the shorter initial pulse will be broadened quickly and when β_2 is larger the pulse will be spread faster, which corresponds to the shorter dispersion length. The pulse broadening becomes significant after the value of L_D.

2.2.4.2 Fiber nonlinearities

The origin of nonlinearity in fibers

The dielectric media have nonlinear response for intense electro-magnetic fields. This nonlinear response stems from the anharmonic motion of bound electrons in the media under the strong applied field. Consequently, the total polarization, $\tilde{P}(\mathrm{r},\omega)$, induced by electric dipoles is not linear in the intense field but includes higher order contributions so that it satisfies the general equation,

$$\begin{aligned}\tilde{P}(\mathrm{r},\omega) &= \varepsilon_0\left[\chi^{(1)}(\omega)\mathrm{E}\right] + \varepsilon_0\left[\chi^{(2)}(\omega):\mathrm{EE} + \chi^{(3)}(\omega)\vdots\mathrm{EEE} + \ldots\right] \\ &= \varepsilon_0\sum_{i=1}^{3}\hat{\mathrm{x}}_i\left[\sum_j \chi_{ij}^{(1)}\mathrm{E}_j\right] + \varepsilon_0\sum_{i=1}^{3}\hat{\mathrm{x}}_i\left[\sum_j \chi_{ijk}^{(2)}\mathrm{E}_j\mathrm{E}_k + \sum_{jkl}\chi_{ijkl}^{(3)}\mathrm{E}_j\mathrm{E}_k\mathrm{E}_l\right] \\ &= \tilde{P}_{\mathrm{L}} + \tilde{P}_{\mathrm{NL}}\end{aligned} \tag{2.13}$$

where ε_0 is the permittivity in vacuum, $\chi(\omega)$ is a tensor quantity of the electric susceptibility, : and $\vdots$ denotes the tensor products respectively, $i, j, k \in \{1,2,3\}$ and is a unit vector (*i.e.* x_1=x, x_2=y, x_3=z). The total polarization term is separated into two parts in Eq (2.13), the first term known as the linear polarization related to the refractive index (n) we discussed at the previous section and the absorption of the medium. The term $\varepsilon_0\sum_{i=1}^{3}\left[\sum_j \chi_{ijk}^{(2)}\mathrm{E}_j\mathrm{E}_k\right]$ is responsible for the nonlinear effects such as second harmonic generation and sum frequency generation. Fibers normally show very low second order nonlinearity because the silica (SiO_2) has an inversion-symmetry and therefore the third order term, $\varepsilon_0\sum_{i=1}^{3}\left[\sum_{jkl}\chi_{ijkl}^{(3)}\mathrm{E}_j\mathrm{E}_k\mathrm{E}_l\right]$ is the lowest order nonlinear effect for fibers. This term is called the four-wave mixing terms (or Kerr effect). From the third order term, n_2 known as the nonlinear refractive index is derived and the n_2 is related to the third order nonlinearity by this following equation.

$$n_2 = \frac{3}{8n}\mathrm{Re}[\chi_{xxxx}^{(3)}], \tag{2.14}$$

where Re stands for the real part of one component of third order susceptibility tensor [132] and n_2 is responsible for self-phase modulation (SPM) which will be discussed in next section. The third order nonlinearity can also trigger the Raman effect such as stimulated Raman scattering in optical fiber [71-73].

Nonlinear phase shift

The $\chi^{(3)}$ is responsible for the third order nonlinearity such as third order harmonic generation and four wave mixing. However, these nonlinear processes are not efficient in optical fibers without careful phase matching which is also true for all the higher order nonlinear processes. Hence, the majority of nonlinear effects in optical fibers are induced by nonlinear refraction related to the intensity dependence of the refractive index. The total refractive index including the nonlinear refractive index (n_2) is written as

$$n(\omega, I) = n(\omega) + n_2 I, \tag{2.15}$$

where I is the optical intensity defined as $I=(\varepsilon/\mu)^{1/2}<E^2>$ where $<E^2>$ is time average value of square of an electric field and μ is the permeability. The intensity-dependent refractive index creates many interesting nonlinear effects such as self phase modulation (SPM) and cross phase modulation (XPM). The SPM is the completely degenerate four wave mixing and the process is automatically phase matched. The SPM generates the self-induced phase shift during the propagation of electric fields in optical fibers. The XPM induces another nonlinear phase shift between different wavelengths. These nonlinear processes play a role in the spectral broadening of ultrashort pulses and the SPM is especially responsible for optical soliton formation in anomalous dispersion fibers. The total phase shift induced by the sum of the linear refractive index and the nonlinear refractive index is

$$\varphi(\omega, I) = n(\omega, I) k_0 z = \left[n(\omega) + n_2 I \right] k_0 z, \tag{2.16}$$

where z is the length of propagation and therefore the phase shift is accumulated with the fiber length.

Nonlinear effects in fused-silica fibers

The nonlinear refractive index, n_2, in silica fibers is about 3×10^{-20} m^2/W [133], which is quite smaller than other nonlinear dielectric media by at least two orders of magnitude. Nevertheless, the optical fiber shows nonlinear effects with fairly low optical power levels. There are two main reasons for that. One is the high optical intensity in optical fibers since the light is confined to a very small core size. For example, the Corning SMF-28e has a mode field diameter of ~10 μm at 1550 nm. The other is due to the extremely low loss of fibers at around 1550 nm. For the pulse propagation in fibers, one typically introduces the fiber effective nonlinear coefficient γ, defined as

$$\gamma \equiv \frac{n_2 \omega_0}{c \pi a^2}, \tag{2.17}$$

where ω_0 is the carrier frequency and a is the mode field radius. For instance, the Corning SMF-28e has γ=1.43 $W^{-1}km^{-1}$.

Nonlinear length

As we defined the dispersion length before, we can similarly define the nonlinear length. The nonlinear length is defined as

$$L_{NL} \equiv \frac{1}{\gamma P_0}, \tag{2.18}$$

where P_0 is the initial peak power. The physical meaning of the nonlinear length is the effective propagation distance over which the nonlinear phase shift becomes 1 radian. For now, we can define a useful parameter from the dispersion length and the nonlinear length which is the ratio between the two, defined as

$$\frac{L_D}{L_{NL}} = \frac{\gamma P_0 T_0^2}{|\beta_2|}. \tag{2.19}$$

When L_D/L_{NL} <<1, the GVD dominates the pulse propagation and when L_D/L_{NL} >>1, SPM dominates the pulse propagation. This is related to the formation of optical solitons in fibers.

2.2.4.3 Soliton pulse propagation in fibers

An optical soliton is a special solution of the nonlinear Schrödinger equation (NLSE) which will be discussed in Chapter 4. The optical soliton can exist in an anomalous dispersion fiber. The soliton is formed in dispersion managed mode-locked fiber laser systems and also observed in fiber laser amplifier systems. The soliton has an interesting property in that the pulse shape does not change along the propagation length and it is useful to send information without distortions, so that it is an important concept in the telecommunication area. The balance between GVD and SPM is responsible for the formation of the optical soliton. In order words, when we consider the ratio, $L_D/L_{NL,}$ to be close to one, both GVD and SPM equally contribute to the pulse evolution and this balance supports the optical soliton. Furthermore, higher order optical soliton solutions exist and L_D/L_{NL} is used to determine the soliton order by the following relation.

$$N_s^2 \equiv \frac{L_D}{L_{NL}} = \frac{\gamma P_0 T_0^2}{|\beta_2|}, \tag{2.20}$$

where the integer N_s is called the soliton order. When $N_s = 1$, it is called the fundamental soliton. The higher order solitons are more unstable due to stronger nonlinear effects. Generally one can introduce the frequency chirp or the instantaneous frequency to represent the effect of GVD and SPM. It is defined as

$$\delta\omega(T) \equiv \omega_c - \frac{\partial\varphi(T)}{\partial T}. \tag{2.21}$$

The frequency chirp ($\delta\omega$) is the time-derivative quantity of optical phase-shift. Figure 2.5 shows the frequency chirp introduced by anomalous GVD and SPM which have opposite signs in the central pulse region. The balance between them produces a net frequency chirp of zero in

the central region. Therefore the pulse experiences net zero dispersion and has the same temporal shape through its propagation.

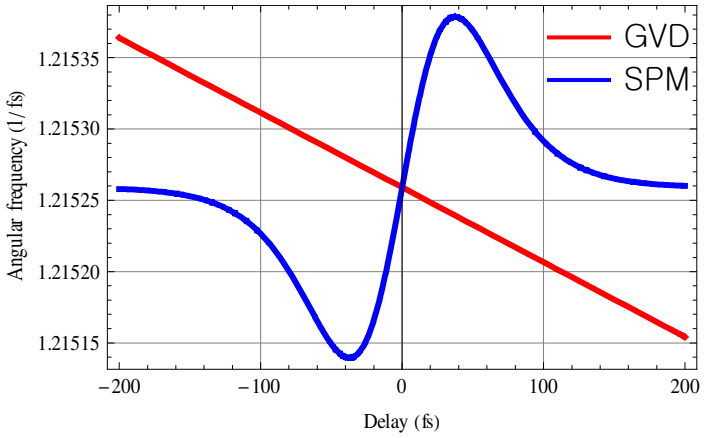

Figure 2.5 Frequency chirp introduced by anomalous GVD and SPM. The balance between anomalous GVD and SPM produces a net frequency chirp is zero of the central region and generates an optical soliton in the anomalous GVD fiber.

There are other forms of solutions existing under different conditions such as a stretched soliton pulse [74], a dissipative soliton pulse [75], and a parabolic pulse (or similariton) [76] although they will not be discussed in this thesis. Those pulses have the capability to contain more pulse energy than the energy of optical soliton pulses limited by the soliton area theorem [77].

2.3 Rare-earth ion doped gain fibers

2.3.1 Gain bandwith of rare-earth ion doped fibers

The fibers doped with the rare-earth ions such as ytterbium, erbium, and thulium can be used to produce gain in a fiber waveguide. Depending on the doped gain ions and host media, the emission wavelength can also be tuned. The table below shows the emission wavelength with the different rare-earth ion doped fibers.

Rare earth Ion	Host glasses	Emission wavelength
Neodymium(Nd^{3+})	silicate and phosphate glasses	1.03–1.1 μm,
Ytterbium(Yb^{3+})	silicate glass	1.0–1.1 μm
Erbium (Er^{3+})	silicate, phosphate, fluoride glasses	1.5–1.6 μm, 2.7 μm
Thulium (Tm^{3+})	silicate, phosphate, fluoride glasses	1.7–2.1 μm, 1.45–1.53 μm
Holmium (Ho^{3+})	silicate, fluorozirconate glasses	2.1 μm, 2.9 μm

Table 2.1 Emission wavelength of the rare earth ion doped fibers

The rare-earth ion doped fibers are very efficient gain media in the infrared wavelength regime. Especially, Erbium doped fibers is widely used in the fiber-optic telecommunication application because the loss in the fused silica single mode fiber is minimized at 1550 nm which is in the gain bandwidth of the Er^{3+} doped fibers. Ytterbium doped fibers are used in the high power fiber laser system due to excellent gain efficiency [78] and the thulium doped fibers are widely used to generate a mode-locked laser at wavelength of 2 μm.

2.3.2 Er^{3+} doped fiber

The fiber doped with Erbium atoms is one of the important gain media in near infrared application and it is also used in fiber optical telecommunication systems. Due to the long relaxation time of the Erbium atoms (~ 1 ms), its lasing atomic structure is assumed to be a three level system. It has two strong absorption lines at 980 nm and at 1480 nm as shown in Figure 2.6 (a) and both wavelengths are typically used to pump the Erbium atoms. The typical absorption and emission spectra are shown in Figure 2.6 (b). The Er^{3+} doped fiber has a broad gain bandwidth over 50 nm in the near infrared around 1550 nm.

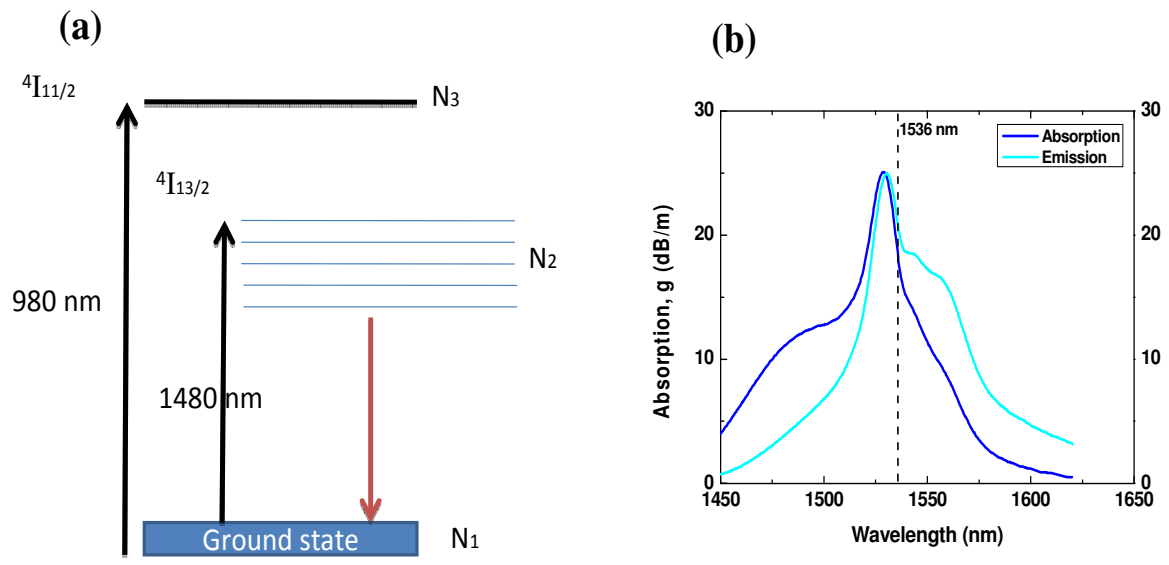

Figure 2.6 The atomic structure of an Er^{3+}atom. (a) The Er^{3+} laser is approximated as a three level laser system because of its long relaxation time. It has two main absorption lines at 980 nm and another at 1480 nm. (b) The absorption and emission spectra of a typical erbium doped fiber. Reproduced from Ref. [134].

2.4 Mode-locked Er^{3+} doped fiber lasers

In this section, we will discuss how to produce ultrashort laser pulses from fiber lasers using the method called mode-locking. The previous discussion about the dispersion and nonlinearity of fibers will be useful in understanding how to generate the shortest pulses from a mode-locked fiber laser.

2.4.1 Mode-locking

In order to achieve short pulses from lasers, the coherent mode coupling is required (specifically, all modes are arrayed in phase) [135], which leads to the mode-locking in lasers. Mode-locking can be categorized generally into two groups which are active mode-locking using an electro-optic modulator or an acoustic modulator, and passive mode-locking using saturable absorbers. For both cases, they selectively pick up the high intensity input and create short pulses. The pulse being able to be produced from the active mode-locking is on the order of picosecond

because the response of the fast electronic switch (t_{switch}) corresponds to an order of GHz. (t_{switch} ~ $1/f_m$) where f_m is the modulation frequency measured in Hertz [135]. Therefore, for the femtosecond pulse generation, passive mode-locking is exclusively implemented because passive mode-locking uses the atomic response of a medium itself. Moreover, passive mode-locking shows the low noise operation and does not require complicated and expensive electronic components. The most well known passive mode-locking technique is Kerr lens mode-locking which uses the $\chi^{(3)}$ nonlinearity, the third order atomic susceptibility (See Chapter 4) of a dielectric medium. Due to the fast nonlinear response of Kerr effect, the femtosecond pulse is readily achieved from that. For fiber lasers, the $\chi^{(3)}$ nonlinearity is also commonly used to obtain the type of passive mode-locking, called the polarization additive pulse mode-locking (P-APM), which is governed by nonlinear polarization rotation [136]. The nonlinear amplifying loop mirror is also used for passive mode-locking [79]. We will briefly discuss the mode-locking mechanisms that we used in our experiment.

2.4.2 Passive mode-locking using self amplitude modulation

Passive mode-locking is used to generate femtosecond pulses. In this section, we discuss the self amplitude modulation (SAM) which modulates the loss in the laser cavity. The SAM can be done with the $\chi^{(3)}$ nonlinearity of optical fibers or semiconductor devices. Here we introduce two methods for the SAM using the fiber nonlinearity.

2.4.2.1 Modulation instability and generation of a pulse train in optical fibers

A CW laser beam inside optical fibers experiences deviation from its optical waveform due to the interplay between the nonlinear effect and dispersion effect. This leads to modulation of the steady state and generates spectral sidebands. Therefore eventually the optical waveform is broken up into a train of pulses. This phenomenon is called the modulation instability [80-83] which is responsible for the formation of a pulse train in optical fiber laser systems. The theoretical frame work can be done with the power perturbation of a CW laser based on the nonlinear Schrödinger equation that will be discussed in Chapter 4. As a result of the perturbation, the maximum modulation gain (g_{max}) and its bandwidth (Ω_{max}) are derived as

$$\Omega_{\max} = \pm\left(\frac{2\gamma P_0}{|\beta_2|}\right)^{1/2} \tag{2.22}$$

and

$$g_{\max} = 2\gamma P_0,$$

The possible gain and gain bandwidth rely on nonlinearity (SPM). There is also a threshold power to initiate the modulation instability at the given effective nonlinearity.

2.4.2.2 Nonlinear amplifying loop mirror and the figure eight laser

The first sub-picosecond mode-locked fiber laser was generated using the nonlinear amplifying loop mirror (NALM) in 1990 [84]. The NALM was employed in a figure eight fiber laser (F8L). It has two fiber rings with 50/50 beam splitter in the middle as illustrated in Figure 2.7. The pump laser was coupled into the cavity using a wavelength division multiplexer (WDM: 980/1550 nm), a device combining two different wavelengths. The electric field in the left ring is split at the 50/50 splitter. The isolator allows unidirectional light propagation in the left ring. Afterwards one electric field propagates the right loop in a clockwise direction and the other propagates in the counterclockwise direction. Each electric field experiences a different amount of phase shift due to the fact that the gain fiber in the NALM is asymmetrically positioned. The amount of phase shift for each pulse can be written with

$$\delta\phi_c = \frac{\pi}{\lambda_s} n_2 g I_s L$$

$$\delta\phi_{cc} = \frac{\pi}{\lambda_s} n_2 I_s L, \tag{2.23}$$

where ϕ_c and ϕ_{cc} are the nonlinear phase shift for the electric field in the clockwise and in the counter clockwise direction respectively, n_2 is the nonlinear index of refraction, I_s is the signal intensity, λ_s is the signal wavelength, and g is the gain coefficient. When the difference of their phase shift is π, they are constructively interfered and create a single short pulse, and therefore the laser is mode-locked.

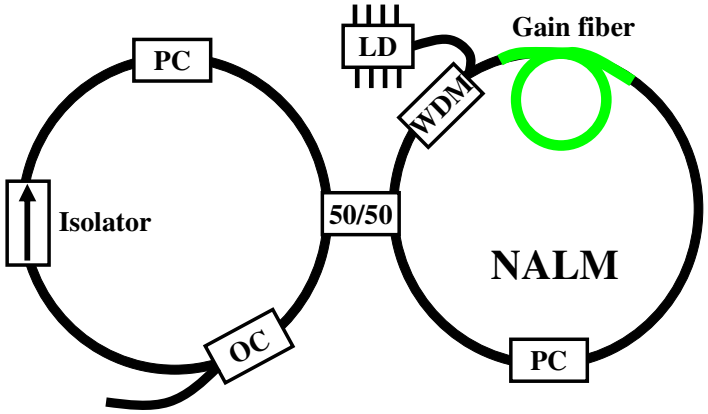

Figure 2.7 Figure eight ring laser using a nonlinear amplifying loop mirror (NALM) saturable absorber [79]. PC: polarization controller, WDM: wavelength division multiplexer, OC: output coupler, and 50/50: beamsplitter (the ratio of 50 to 50). The electric field is split at 50/50 beam splitter in the middle. One propagates the loop in the clockwise direction and the other propagates in the counterclockwise direction. Those electric fields interfere in the NALM which is a Sagnac interferometer and mode-locked pulses are generated when the difference in the phase shift of two electric fields is 180^{o}.

Since the NALM uses the fast fiber nonlinear process, it can readily produce femtosecond pulses. However, the disadvantages of the F8L are that it requires relatively long fiber length because it has two rings for the laser cavity, which is not appropriate for the high repetition frequency mode locked laser source. In addition to that, the F8L has not shown a self starting property which will be discussed in Section 2.5.4.

2.4.2.3 Polarization additive pulse mode-locking

The massive and intense research about the Polarization additive pulse mode-locking (P-APM) was done by K. Tamura, E. P. Ippen, and H. A. Haus in the early 1990s at MIT [74, 85, 86]. The P-APM is employing the $\chi^{(3)}$ nonlinearity or Kerr nonlinearity of the dielectric medium. The mode-locking mechanism is visually illustrated in Figure 2.8. The lightwave is first linearly polarized and then elliptically polarized with a polarization controller. Because the light intensities between two principal axes are different, the lightwave experiences different amounts of nonlinear phase shift for each axis. Therefore the lightwave starts to rotate, known as the nonlinear polarization rotation, in the dielectric medium. Thereafter another polarization controller selects the lightwave polarized in a particular direction possessing high peak intensity.

The iteration of the process shapes the lightwave in the laser cavity and generates ultrashort pulses.

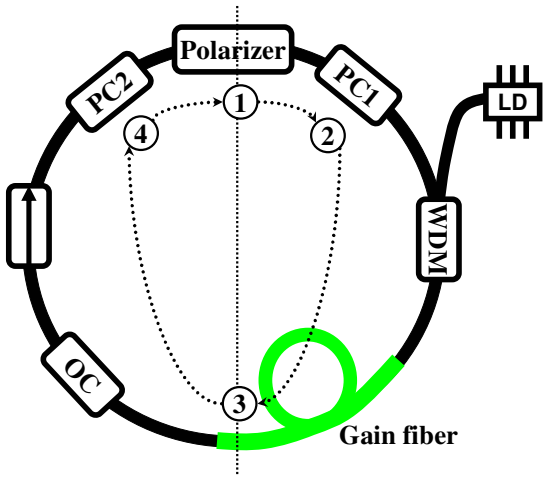

Figure 2.8 A fiber ring laser using Polarization Additive Pulse Mode-locking (P-APM). PC: Inline polarization controller, WDM: wavelength division multiplexer, and OC: Output coupler. ①: the initial lightwave is linearly polarized. ②: the PC1 elliptically polarizes the lightwave. ③: the elliptically polarized lightwave in the different axes propagates through the dielectric medium (fiber) possessing Kerr nonlinearity. Due to the different intensities in the different axes, the light polarization is rotated, which is known as the nonlinear polarization rotation. ④: the PC2 only allow for the lighwave polarized to particular direction which has the high peak intensity. Therefore the ultrashort pulse can be created.

We made an all-fiber ring laser using the P-APM that can produce a mode-locked laser possessing the repetition frequency of 100 MHz. However, we had a difficulty to get mode-locking and self-starting at the higher repetition frequency due to the relatively low intra-cavity energy.

2.5 Mode-locked Er^{3+} doped fiber laser cavity design strategies

In this section, we discuss strategies to make mode-locked Er^{3+} doped fiber lasers. General strategies we showed here may be applied to any type of Er^{3+} doped mode-locked fiber lasers. However, the details, for example, to choose the pump power and the length of fiber, may differ with the mode-locking methods we discussed in Section 2.4.

2.5.1 Gain and loss in the cavity

2.5.1.1 Small signal gain of an Er^{3+} doped fiber

Lasing starts when the total small signal gain (SSG) is larger than the cavity loss. The gain for a laser oscillator can be quantified by measuring the small signal amplification at the given length of the gain fiber. The achievable SSG depends on the length of the fiber and the pump power as shown in Figure 2.9. The small signal gain (SSG) of Liekki Er110 has been measured. Figure 2.9 (a) shows that the measured SSG at different pump powers for a length of Liekki Er110 of 50 cm. The SSG is higher when the pump power is strong for the given length of Liekki Er110 and the SSG linearly increases when the pump power keeps increasing. The SSG measured at different length of Liekki Er110 at 250 mW pump power has been shown in Figure 2.9 (b). The turning point at the length of Liekki Er110 of 80 cm is related to the pump depletion. In fact, we can recognize the pump depletion point by looking at the green fluorescence from Liekki Er110. It becomes dimmer when pump power gets depleted.

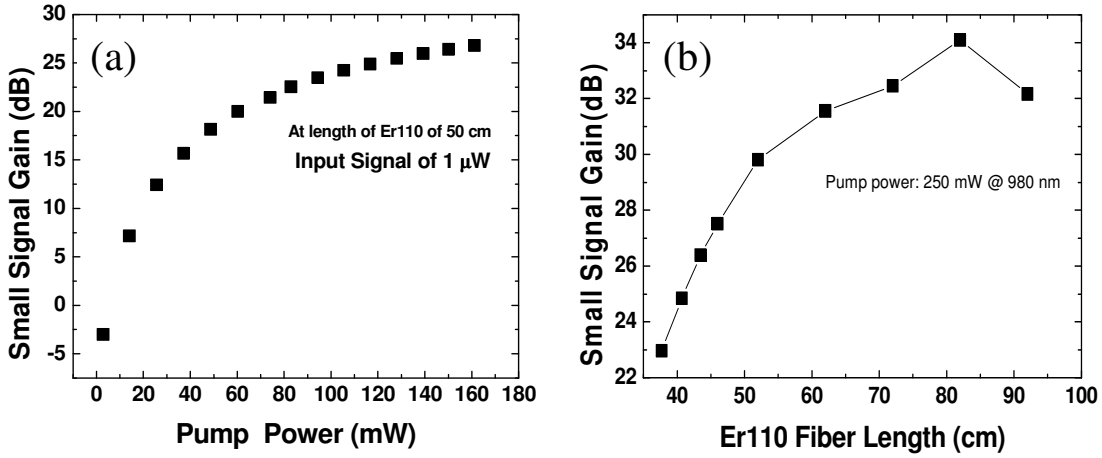

Figure 2.9 The small signal gain (SSG) of Liekki Er110. (a) The SSG measured at different pump powers at the length of Er110 of 50 cm. The SSG is higher when the pump power is higher for a fixed length of Liekki Er110. (b) The SSG measured at different length of Er110 at 250 mW pump power. The turning point at the length of Liekki Er110 of 80 cm is related to the pump depletion. In fact, one can recognize the pump depletion point by looking at the green fluorescence from Liekki Er110. It becomes dimmer when pump power gets depleted.

2.5.1.2 Cavity loss

The possible cavity loss comes from insertion losses of fiber optic components (isolator, output coupler, WDM, piezo-electric fiber transducer), and fiber splicing. Practically, the loss was not a big issue to operate the laser because Er^{3+} doped fiber laser has relatively high SSG as shown in Figure 2.9. The cavity loss, however, is related to the stability of a mode-locked fiber laser because it modulates pulse energy in the cavity [34]. In addition, the low cavity loss is desirable to obtain a broader spectral bandwidth. Therefore it is good to minimize cavity loss by making a good splice and using the low loss fiber optic components.

2.5.2 Cavity loss and shift in the center wavelength

The cavity loss results in a shift in the center wavelength of a mode-locked laser. This is because the pump power is increased to compensate the loss, which leads to the change in frequency-dependent gain producing gain filtering [87]. In Figure 2.11, the gain peak shifts to the shorter wavelength when the pump power increases. Consequently, the center wavelength is shifted to the shorter wavelength in Figure 2.10.

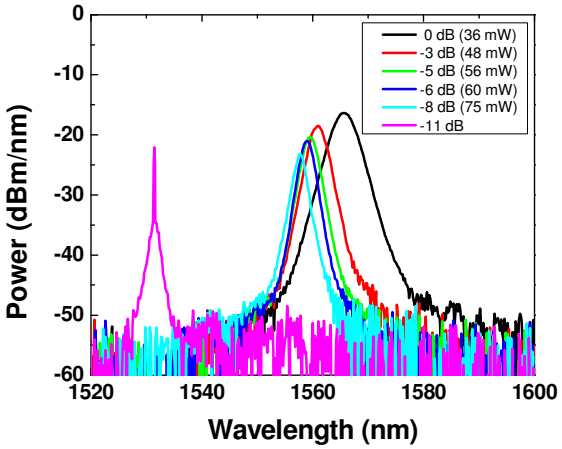

Figure 2.10 A mode-locked CNFL with different amount of cavity loss. By adding fiber connector-typed attenuators in the cavity we purposely changed the cavity loss. The Liekki Er110 of 34 cm was used. The laser stayed in mode-locking until the intentionally added attenuation was -8 dB. The center wavelength was shifted to the shorter wavelength due to the gain filtering. The spectral bandwidth became narrower because of high cavity loss combined with a gain narrowing effect.

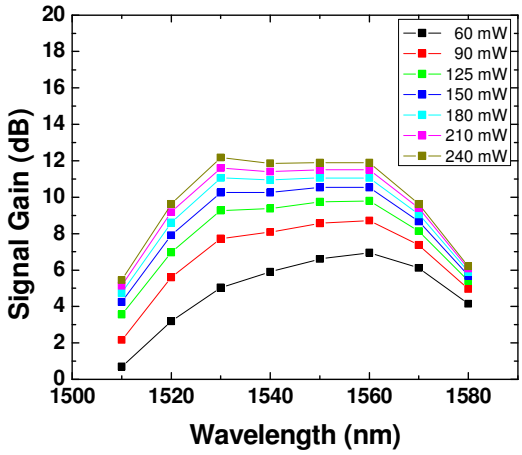

Figure 2.11 The frequency dependent gain. The gain was measured with a tunable wavelength laser (Santec). At different pump powers, the gain showed different profiles. The gain peak was shifted to shorter wavelengths. The fractional change in the gain profile was relatively small when Liekki Er110 was strongly pumped.

There are interesting points here. First, the available gain increases by pumping EDF harder and harder at the given length of EDF. Secondly, the narrowing in the pulse bandwidth in Figure 2.10 is due to the higher cavity loss combined with a gain narrowing effect. After the pulse experiences the center wavelength shift in EDF, the pulse circulates the lossy cavity which attenuates the gain. Since the gain at both spectrum ends is relatively smaller than the gain at the peak (this is called gain narrowing and will be discussed in Chapter 4), the net gain can be negative there. Hence this results in the narrowing of spectral bandwidth. One more interesting point is that the fractional change in gain is small when the pump power becomes higher and higher (See Figure 2.11). This might give a better immunity for the possible pump power perturbation to the mode-locked laser.

2.5.3 Cavity dispersion and spectral bandwidth

The cavity dispersion is another considered parameter for the cavity design. The control of dispersion is critical to obtain short and high energy pulses with the fiber nonlinearity from the mode-locked laser cavity. The soliton laser has a limitation in the obtainable spectral bandwidth and energy as explained by the soliton area theorem. To avoid this, the laser are usually mode-locked at the stretched soliton regime [74]. This requires alternative dispersion signs and close to

zero net dispersion in the cavity. Therefore the pulse repeats stretching and compression in the cavity and increases its spectral bandwidth and energy. In practice, the choice of EDF affects the bandwidth because EDFs have different dispersions and gains. In order to demonstrate the contribution of dispersion to the spectral bandwidth, we used two types of EDFs. One is the Liekki Er110 and the other is OFS EDF80. The group velocity dispersion of Liekki Er110 was $+1.13 \times 10^{-5}$ fs^2/nm and that of OFS EDF80 was $+6.12 \times 10^{-5}$ fs^2/nm. (*cf*. Group velocity dispersion of the Corning SMF-28e is -2.28×10^{-5} fs^2/nm). Here, we show a CNFL cavity design as an example of the dispersion control. For both cases, the length of Liekki Er110 used was about 60 cm. The bandwidth with Liekki Er110 was typically about 7-10 nm in our experiment at the repetition frequency (f_r) of 73 MHz (total cavity length ~ 4.12 m). The bandwidth was able to be increased by a few nanometer by increasing the pump power but it led to the multi-pulsing or damage of single walled carbon nanotube connector (we will discuss this in Chapter 3). Practically, the spectral bandwidth for CNFL was limited by the available pump power and cavity dispersion. The total group delay of this mode-locked fiber laser, quantified by multiplication of group velocity dispersion and the length of fiber ($\beta_2 \times L$), was -0.0768 ps^2. When we used OFS EDF80, the possible spectral bandwidth was ~25 nm at the f_r of 73 MHz due to the better dispersion management in the cavity. The total group delay was -0.0330 ps^2. The mode-locked fiber laser with Liekki Er110 showed a sech^2 spectrum implying the nearly soliton mode-locking. The Kelly-side bands [88] were also observed on the spectrum. The Kelly-side bands originated from the periodic disturbance of soliton pulse in the laser resonator. This periodic disturbance comes from the discrete nature of dispersion and nonlinearity and loss in the cavity. The coupling between soliton and the temporally spreading waves by the periodic disturbance is responsible for the formation of the Kelly-side bands. The Kelly-side band is useful to calculate the cavity dispersion according to the following equation,

$$DL = \frac{2|N|}{c\left(\frac{\Delta\lambda_n}{\lambda_c}\right)^2 + 0.0787\frac{\lambda_c^2}{c\tau_p{}^2}} \tag{2.24}$$

where D is the dispersion parameter, L is the length of laser cavity, N is the number representing the Kelly-side band peak from the center wavelength in order, c is the speed of light, λ_0 is the

center wavelength, $\Delta\lambda_n$ is the distance from the center wavelength to the peak wavelength in nm, and τ_p is the pulse duration. The total $\beta_2 \times L$ is calculated using the equation,

$$\beta_2 L = -\frac{DL\lambda_c^2}{2\pi c} \tag{2.25}$$

Contrary to the mode-locked laser with Liekki EDF, the mode-locked fiber laser with OFS EDF80 has revealed the pulse close to stretched-soliton. The spectrum was fit to a Gaussian rather than sech^2. As the total dispersion went down to zero, this laser was more unstable and the achievable spectral bandwidth also became narrower. The obtained spectra are shown in Figure 2.12. Practically, the length of EDF is minimized in order to increase the repetition frequency for optical frequency metrology, which makes not only the reduction in obtainable optical gain but also the reduced positive dispersion and therefore the possible net cavity dispersion gets more negative. Overall, the spectral bandwidth becomes narrower.

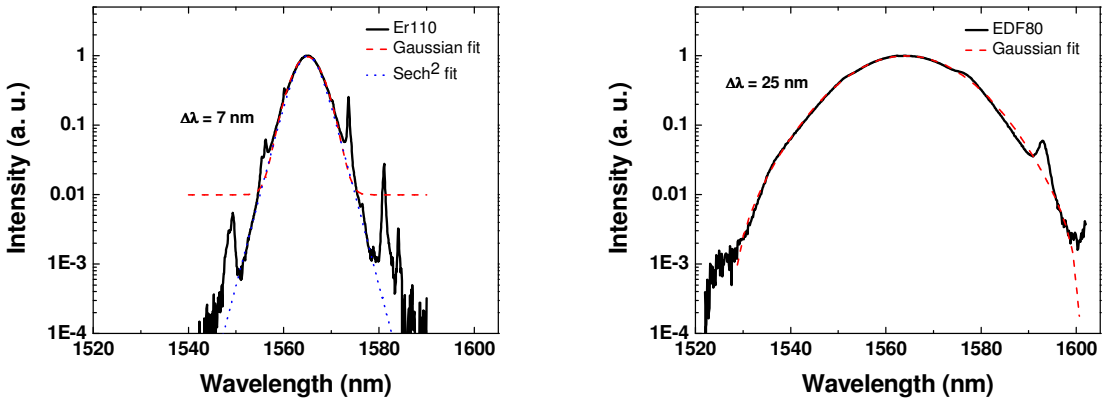

Figure 2.12 Mode-locked spectra both at the same repetition frequency (f_r = 73 MHz). (a) The mode-locked fiber laser spectrum with Liekki Er110 (β_2 = +1.13 × 10^{-5} fs^2/nm). The spectrum showed a sech^2 shape implying nearly soliton pulse mode-locking and the strong Kelly-sidebands were observed. The spectral bandwidth was ~7 nm and it was able to be increased by a few nanometer by increasing the pump power. The total cavity dispersion was -0.0768 ps^2 for the laser. (b) The mode-locked fiber laser spectrum with OFS EDF80 (β_2 = +6.12 × 10^{-5} fs^2/nm). The obtained spectrum is close to a Gaussian shape meaning a stretched soliton pulse. Due to the better dispersion control, the achieved spectral bandwidth was ~25 nm. The total $\beta_2 \times L$ was -0.0330 ps^2 for this laser.

2.5.4 Self starting and reflection in the cavity

All fiber laser cavities do not have shown the self-starting behavior which means that the laser can be mode-locked from a CW intensity fluctuation without a starting trigger. The F8L we built using the NALM as a saturable absorber did not show the self-starting. It required a physical knocking to start the mode-locking. The other lasers, such as a P-APM ring laser and CNFLs, have shown the self-starting. The self-starting can be explained with a unidirectional laser operation. Unlike a linear cavity, the ring cavity structure with an isolator significantly reduces reflections inside the cavity which causes a frequency pulling effect affecting the mode-locking.

Figure 2.13 shows that the effect of the atomic gain medium on the cavity modes. The gain induced phase shift, $\varphi_m(\omega)$ can be describe by $\varphi_m(\omega) = \Delta\beta_m(\omega)L_m$. Where $\Delta\beta_m(\omega)$ is the gain-induced dispersion expressed by $\Delta\beta_m(\omega)=\omega\chi'(\omega)/2c$ and L_m is the length of the gain medium. In the equation, the $\chi'(\omega)$ is the real part of the atomic susceptibility, the c is the speed of light and ω is an angular frequency. The atomic susceptibility will be discussed in detail in Chapter 4. Therefore the total phase shift is the sum of the linear phase shift and the gain induced phase shift as illustrated in Figure 2.13. For the simplicity, the frequency pulling term for a Lorentzian atomic transition can be assumed and rewritten with a Lorentzian form of atomic gain coefficient, $g_m(\omega)$ and then the equation for the $\varphi_m(\omega)$ is described by

$$\Delta\beta_m(\omega) = 2\frac{\omega-\omega_a}{\Delta\omega_a} g_m(\omega), \tag{2.26}$$

where ω_a is the resonant frequency. Hence the amount of the frequency pulling defined by the pulling amounts divided by the cavity mode spacing ($\delta\omega_q/\Delta\omega_{cav}$) is approximately,

$$\frac{\delta\omega_q}{\Delta\omega_{cav}} \approx -\frac{2g_m(\omega)L_m}{2\pi}\frac{\omega_q-\omega_a}{\Delta\omega_a}. \tag{2.27}$$

where ω_q is the q^{th} comb tooth. Based on this equation the frequency pulling is related to the atomic gain, $g_m(\omega)$. Reflections inside a cavity create more complicate and fluctuating structures

of the atomic gain and the amount of the frequency pulling varies, so that the cavity modes are jumping around which results in preventing a laser from efficient mode-coupling or mode locking with fast saturable absorbers. In practice, the self-staring is realized by employing a unidirectional fiber laser cavity design with an isolator.

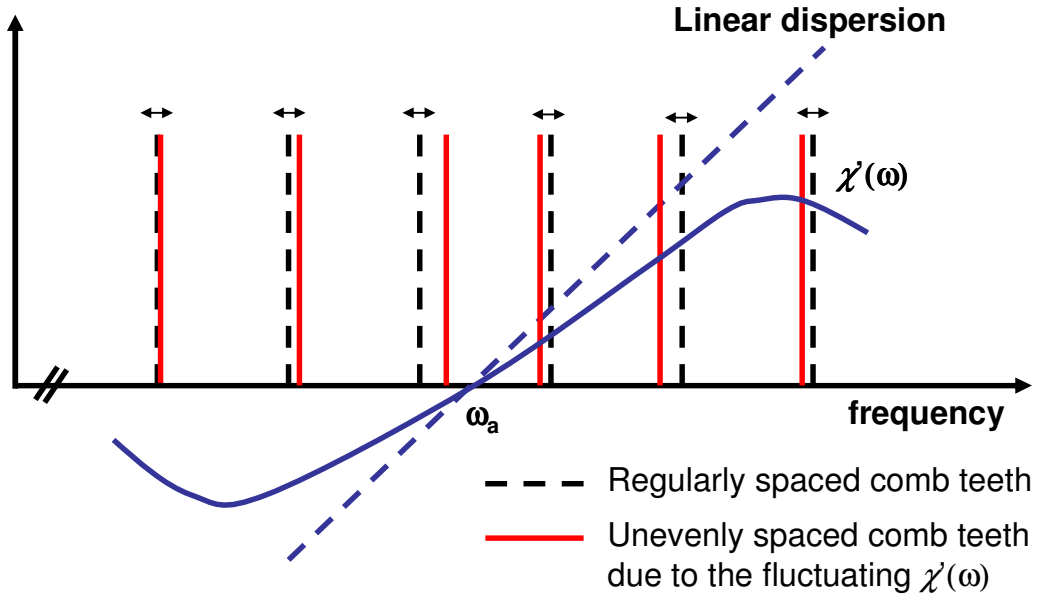

Figure 2.13 The frequency pulling effect caused by the atomic gain phase shift. $\chi'(\omega)$: the real part of atomic susceptibility. The dispersion shaped by $\chi'(\omega)$ is generated and the reflection creates more complicated and fluctuating $\chi'(\omega)$ structures, so that total dispersion changes with time for each comb tooth. Therefore the comb teeth experience time-varing dispersion and the comb teeth are fluctuating, which results in preventing a laser with fast saturable absorbers from mode-locking.

2.6 Summary

In this chapter, we reviewed the femtosecond Er^{3+} doped mode-locked fiber laser. We discussed properties of optical fibers and their origins which included the guiding mechanism of step index fiber, the group velocity dispersion (GVD) and the self phase modulation (SPM). The balance between GVD and SPM is responsible for the soliton pulse propagation in optical fibers. The Er^{3+} doped fiber is an excellent gain medium in the near infrared at the wavelength of

1550 nm which is not covered by Ti:Sapphire mode-locked lasers. Therefore we can take its advantage in optical frequency metrology at around 1550 nm. We discussed general strategies to make an Er^{3+} doped fiber laser. The gain (or loss), dispersion, and nonlinearity should be considered for the laser design and the spectral bandwidth and pulse duration are related to those parameters. We introduce passive mode-locking mechanisms. The modulation instability and saturable absorber generate an ultrashort pulse train in Er^{3+} doped fiber lasers. We have shown two artificial saturable absorbers using fiber Kerr nonlinearity and the disadvantage of those saturable absorbers is that they requires relatively long lengths of fibers for mode-locking. In our experiment using the fiber Kerr nonlinearity for mode-locking, it is difficult to get more than the repetition frequency of 100 MHz in all-fiber set-up. However, the high repetition frequency is desirable for optical frequency metrology.

Passive mode-locking can be also achieved using semiconductor saturable absobers such as a semiconductor satuarble absorber mirror (SESAM), a semiconductor Bragg reflector (SBR), and single walled carbon nanotubes (SWCNT). Unlike NALM and P-APM, those are real saturable absorbers and use the excitonic absoption of the semiconductor material for saturable absorption. The pioneering research has been done by Islam, Knox, and Keller [89-92]. The advantage of using the semiconductor saturable absorbers is that it is possible to tune the absorption wavelength and therefore they can be used for mode-locking laser of different wavelengths. In addition, they allow for making mode-locked lasers compact and allow for high repetition frequency. Especially we will focus the SWCNT saturable absorber [67, 93] in the next chapter. The SWCNT saturable absorber provides extremely compact, robust, and cost-effective mode-locked fiber lasers in an all-fiber configuration and has been used to high repetition frequency comb for optical frequency metrology.

Chapter 3 - High Repetition Frequency Fiber Laser Frequency Comb Using Single Walled Carbon Nanotube Saturable Absorber

3.1 Introduction to high repetition frequency mode-locked fiber lasers

We reviewed the mode-locking mechanisms and pulse formations in the fiber laser cavity in Chapter 2. For optical frequency metrology, higher repetition frequency (>100 MHz) is desirable in order to increase the resolving power among comb teeth. In addition, we wanted to make the laser a compact and all-fiber system for a cost-effective and turn-key operation. In this sense, the NALM mode-locking and P-APM were not the best choices.

There are technical challenges to making a high repetition frequency mode-locked fiber laser using the self amplitude modulation using the fiber nonlinearity discussed in the previous chapter because they require relatively high intracavity energy and long fiber lengths to initiate mode-locking. However, in order to increase the pulse repetition frequency, the fiber cavity length becomes shorter and shorter with the length of gain fiber and therefore the stored pulse energy in the laser cavity decreases. Hence, one generally uses a saturable absorber such as semiconductor saturable absorber mirror (SESAM) in order to make a high repetition frequency mode-locked fiber laser. The Kärtner group at MIT has demonstrated the ~1 GHz repetition frequency Er^{3+} doped fiber laser using a saturable Bragg reflector (SBR) which is also a semiconductor quantum well device [94]. Even if these methods allow for the high repetition frequency fiber laser, there are some drawbacks. First of all, SESAM and SBR require sophisticated and expensive fabrication techniques. In order to reduce the recovery time of those semiconductor devices, the defects acting as recombination centers are created using the special low-temperature growth as well as ion implantation techniques. These make their fabrication process complicated and expensive. Secondly, it is not possible to integrate it into the fiber laser cavity in an all-fiber set-up. In most cases, a free-space linear cavity is used with SESAM and SBR. In our research, we employed the single walled carbon nanotubes (SWCNT) as a saturable absorber, which allows for a cost-effective and simple fabrication without losing the advantages

of semiconductor saturable absorber devices. In addition, the SWCNT saturable absorber can be readily integrated into the fiber laser ring cavity.

We have intensely studied the frequency comb generated from Er^{3+} doped mode-locked fiber lasers employing the SWCNT saturable absorber. In this thesis, we named it as the carbon nanotube fiber laser (CNFL). The SWCNT was incorporated using an optically driven deposition method [95] into the laser cavity which allowed for an all-fiber laser configuration. In addition to that, the high repetition frequency comb was readily obtained and we took advantage for optical frequency metrology.

3.2 Semiconductor saturable absorbers

Semiconductor saturable absorbers such as SESAM, SBR, and SWCNT have been widely used because of their readiness for passive mode-locking. For mode-locked fiber lasers, they have been implemented to reduce the cavity length so that the repetition frequency of a train of pulses has been increased. The physical interpretation of the semiconductor saturable absorbers is discussed here.

3.2.1 Principle of the semiconductor saturable absorber

The interband transition is responsible for the saturable absorption behavior of the semiconductor devices. As illustrated in Figure 3.1, photons are absorbed by a semiconductor saturable absorber. The photon energy is then transferred to carriers (electrons in this discussion) and electrons are excited from the valence band to the conduction band. For low optical intensities, the population of excitation is small and therefore the states in the conduction band are not fully occupied, so that the absorption remains unsaturated. However, for high optical intensities, the electrons can be accumulated in the conduction band. As a result, the states in the valence band for the absorption transition are depleted while the states in the conduction band are occupied. Therefore the absorption is reduced.

After saturation with an intense pulse, the absorption recovers partially by coherent carrier dynamics which may last between 10-50 fs at room temperature depending on excitation density, intraband thermal relaxation caused by electron-electron scattering, and phonon

emission through electron-lattice interactions which cool the electrons down to lattice temperature. After the thermalization and cooling process, the electrons move to the bottom of the CB and these processes occur within a relatively fast time-scale (< 1 ps). Then the electrons vanish either by being trapped in defect (or impurity) states whose time-scale is ~100 fs - 100 ps or by recombination on a nanosecond time-scale [137]. Therefore the carrier lifetime is dependent on the growth conditions and purity of the material. In order to reduce the carrier lifetime (or recovery time of a saturable absorber), the defects are created using special low-temperature growth as well as ion-bombardment. The measurement of recovery time is carried out by measuring pump and probe response of a semiconductor saturable absorber. The recovery time of < 1 ps is possible for the semiconductor saturable absorber and therefore a femtosecond ultrashort pulse can be generated by using them.

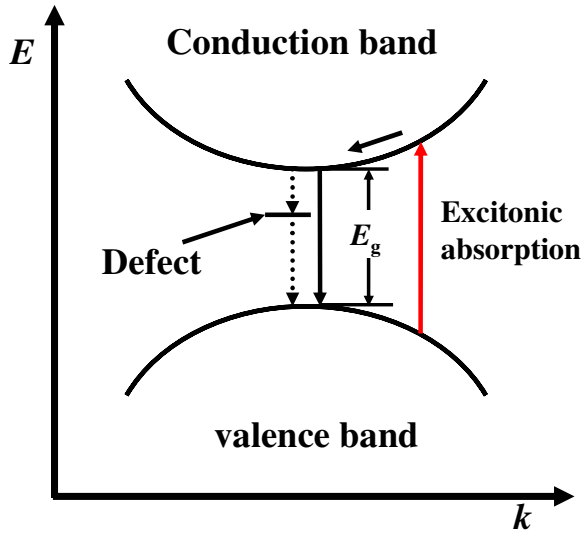

Figure 3.1 Dispersion relation of a semiconductor. E_g: energy gap. Photons are absorbed and electrons in the valence band are excited to the conduction band. For the high optical intensity pulses, the electrons are accumulated in the conduction band, so that the initial states for the absorbing transition are depleted while final states are occupied. After saturation with a short pulse, the absorption recovers partially by intra-band relaxation which includes electron-electron scattering and electron-lattice interactions. The process of the intra-band relaxation may last between 10-50 fs depending on excitation density at room temperature. Then the electrons vanish either by being trapped in defect (or impurity) states whose time-scale is ~100 fs - 100 ps or by recombination on a nanosecond time-scale [137].

3.3 Single walled carbon nanotube saturable absorber

The single wall carbon nanotube (SWCNT) is a reliable saturable absorber for passive mode-locking. The SWCNT is a type of semiconductor saturable absorber and the physical mechanism discussed in Section 3.2 can be applied to the SWCNT absorber. In this section, we discuss properties of SWCNT saturable absorber and a deposition method of SWCNT into fiber laser cavity.

3.3.1 Properties of the single walled carbon nanotube saturable absorber

The terminology for a satiable absorber is listed to help understand the following discussion.

- Modulation depth: Maximum change in absorption. A large modulation depth leads to strong pulse shaping and self-starting.
- Recovery time: The decaying time of the excitation after an exciting pulse.
- Saturation fluence: The fluence (energy per unit area) measured when the initial value reduces to 1/e of its initial value.
- Saturation energy: Saturation fluence times mode field area.

The properties of SWCNT have been intensively investigated since it was synthesized in the early 1990s [93]. Studies of the electronic structures and optical properties have proven that the SWCNT was a promising optical saturable absorber [96]. The first demonstration of a mode-locked fiber laser with a SWCNT came in 2004 by Sze. Y. Set *et al.* [67]. The SWCNT acts like a saturable absorber possessing an ultrafast recovery time which is less than 1 ps so that the femtosecond pulse is readily achieved.

The SWCNTs are categorized by their chirality into semiconducting, semimetallic, metallic nanotubes. The chirality is defined by the chiral vector, $\mathbf{C_h} = m\mathbf{a_1} + n\mathbf{a_2}$ on a two dimensional graphene sheet as shown in Figure 3.2. The saturable absorption property of SWCNTs originates from the excitonic absorption of semiconducting nanotubes, while metallic nanotubes are known to be responsible for the ultrafast recovery time acting like defects in SESAM for recombination centers.

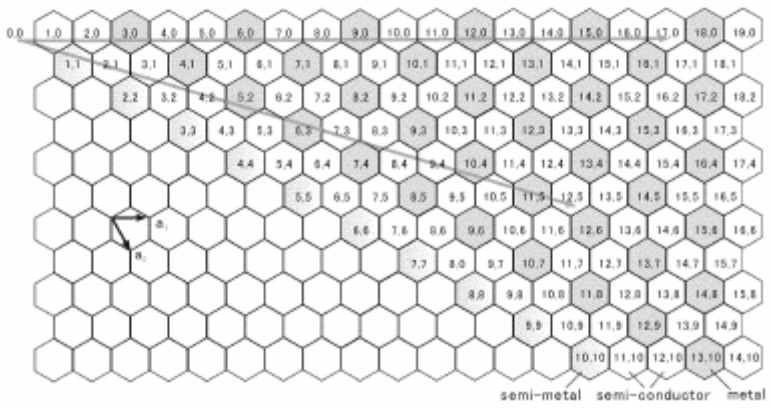

Figure 3.2 A two dimensional graphene sheet. The chiral vector is defined by $C_h = ma_1 + na_2$. The sample of SWCNTs is composed of the semimetallc, semiconducting, and metallic nanotubes. Reproduced from Ref. [67].

Depending on the chiral vector, also called the roll-up vector, SWCNTs have different energy bandgap structures. Figure 3.3 shows the energy bandgaps for two different chiral vectors which are (m,n)=(12,5) and (m,n)=(17,0) respectively. The diameter of nanotubes depends also on the chiral vector and the change of the diameter has shown interesting optical property as shown in Figure 3.3.

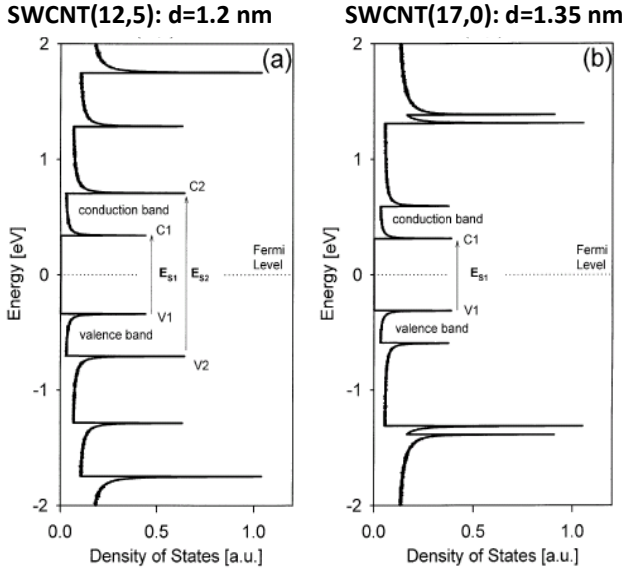

Figure 3.3 Energy bandgap depending on the chiral vector. Two different chiral vectors (12,5) and (17,0) have different diameters and their energy bandgap structures are different, which implies different saturable absorption bandwidths. Reproduced from Ref. [67].

By engineering the diameter of the SWCNT, different absorption bands can be obtained, which is useful for the laser application to tune the saturable absorption wavelength and its bandwidth. This property allows for achieving mode-locked lasers in different wavelength regimes. For example, the SWCNT saturable absorbers have been used in order to mode-lock fiber lasers at 1 μm, [97] 1.55 μm, and 1.9 μm [98].

3.3.2 Absorption at different wavelengths

We used the SWCNT made by Unidym Inc. possessing a mean diameter of 1 nm. As we mentioned earlier, the absorption property of SWCNT depends on the tube diameter. We measured the absorption of the SWCNT using a supercontinuum spectrum source, a broadband coherent source, which was stretched from 1.0 μm to 2.2 μm. The measured absorption from 1200 nm to 1750 nm using an optical spectrum analyzer is shown in Figure 3.4 and it is compared to absorption spectra of SWCNTs possessing different tube diameters [67].

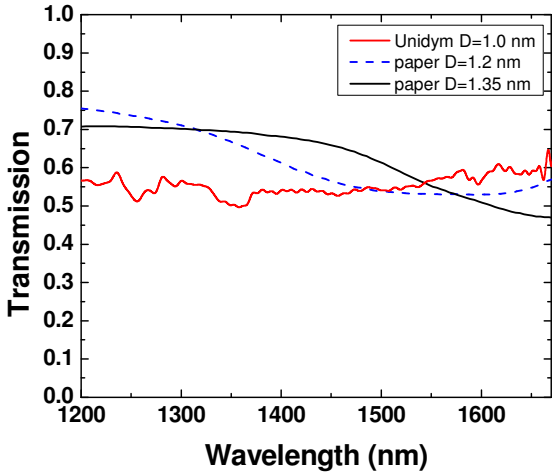

Figure 3.4 Absorption of the SWCNT (Unidym Inc.) at different wavelengths. This is measured with a supercontinuum spectrum (more than an octave spanning coherent source) in the near infra-red and the result compared to the transmission of different SWCNTs possessing different tube diameters. The red line is the transmission spectrum for our SWCNT (Unidym Inc.) whose diameter (D) is 1.0 nm, Both the dashed blue line for the transmission of the SWCNT with D of 1.2 nm and the black line for the transmission of SWCNT with D of 1.35 nm are reproduced from Ref. [67].

The SWCNT has shown a fairly uniform absorption at the wavelengths we are interested in from 1500 nm to 1600 nm. The maximum absorption peak was shown at ~1350 nm and this was the lower wavelength than those of larger diameter SWCNTs. The smaller diameter (D) corresponds to the larger energy bandgap leading to higher absorption energy corresponding to shorter wavelength.

3.3.3 Saturable absorption and modulation depth

The saturable absorption of the SWCNT (Unidym Inc.) was measured by injecting a femtosecond pulse from an Er^{3+} doped mode-locked fiber laser to the SWCNT connector. The pulse intensity was changed by attenuating the average power of the source. The measured data was fit to an exponential decay function and the modulation depth was measured. The measured modulation depth was 27 % which was similar to the value reported by Sze. Y. Set *et al.* [22]. The larger modulation depth corresponds to strong pulse amplitude modulation. The SWCNT has ~ 13 % background absorption which increased the cavity loss. The saturable fluence of the SWCNT is a few tens of $\mu J/cm^2$ which is close to that of SESAM [67, 90], which implies that the SWCNT is very easily saturated in a standard single mode optical fiber at 1550 nm with the pulse energy of ~ pJ. Therefore, the mode-locking of CNFL has been achieved at lower pump power than that of our figure eight fiber laser and P-APM fiber ring laser.

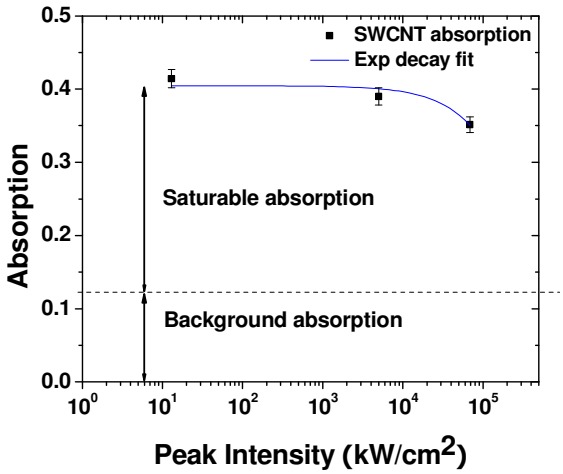

Figure 3.5 Saturable absorption of the SWCNT (Unidym Inc.). The absorption decreases exponentially for the high peak intensity. It has the modulation depth of 27 % and the background absorption of 13 %.

3.3.4 Deposition methods of the SWCNT

A variety of deposition methods have been tried to incorporate SWCNT into the fiber laser cavity. The first laser that used SWCNT saturable absorber was demonstrated with a spray coated mirror or quartz plate such as (a) [67] and (b) [91] in Figure 3.6. However, a much simpler method was introduced by J. W. Nicholson *et al*. which is called the optically driven deposition method [95]. The procedure is described in Section 3.3.6. The method is very simple and easy but it has a drawback which will be discussed in Section 3.3.7. Some other methods include the evanescent interaction with SWCNT. For instance, the tapered fiber (d) is used or a SWCNT doped polymer optical fiber is fabricated (e) for that purpose as shown in Figure 3.6.

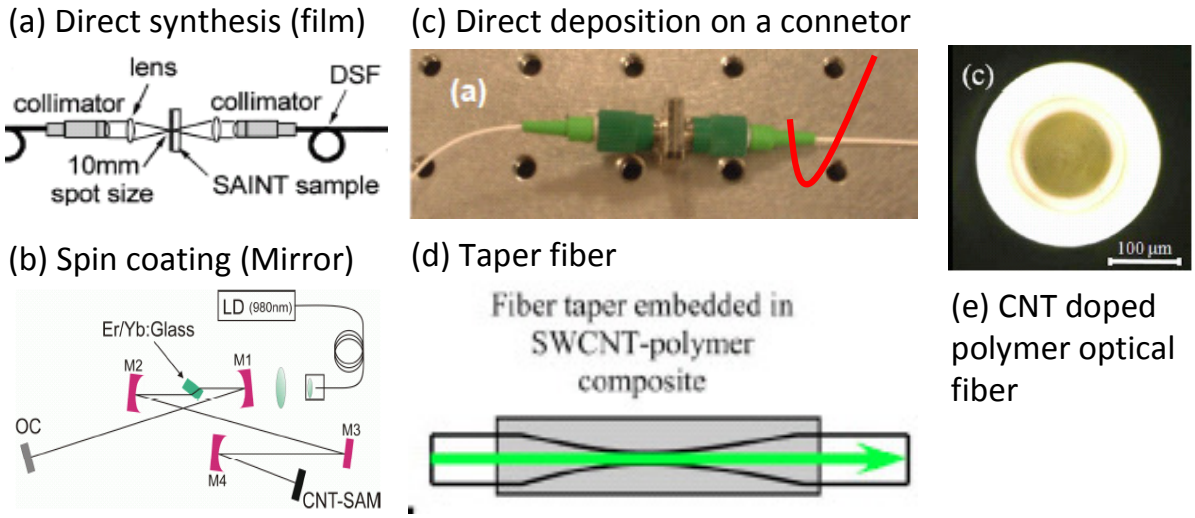

Figure 3.6 A variety of SWCNT incorporating methods; (a) Direct synthesis on thin film, (b) Spin coating on a mirror, (c) Direct deposition on a fiber connector, (d) Fiber taper embedded in SWCNT-polymer composite, (e) Fabrication of a SWCNT doped polymer optical fiber.

3.3.5 Optically driven SWCNT deposition process

The SWCNT has been incorporated into the fiber laser cavity using the optically driven deposition method providing an easy and simple incorporation of SWCNT. The SWCNTs are thermally attached to a fiber connector end-face by the absorbed heat from laser radiation. However, we were not able to control the deposition process such as thickness or uniformity of SWCNT deposition.

The set-up is depicted in Figure 3.7. First of all, the SWCNT solution was made with 0.5 mg of SWCNT and 12 mL of ethanol and then the solution was well mixed for 30 minutes using an ultrasonicator. Then a connector end-face of a fiber patchcord is dipped into the solution with the optical radiation power of 10 mW at 1560 nm. After 30 seconds, it is pulled out of the solution and is dried for a minute. Thereafter the optical power is measured. These processes are repeated until the power loss is roughly 2 dB, which indicates enough SWCNT on the fiber connector end-face. The method is summarized below,

1) Prepare single walled carbon nanotube (SWCNT) solution (0.5 mg of SWCNT and 12 mL of ethanol) and ultrasonicate it for 30 minutes.

2) Dip the fiber connector end-face into the solution with radiation power of 10 mW at 1560 nm for 30 seconds.

3) Pull it out from the solution and wait 1 min.

4) Measure the optical power.

5) Repeat the step 2)-4) until the measured power loss is ~ 2 dB.

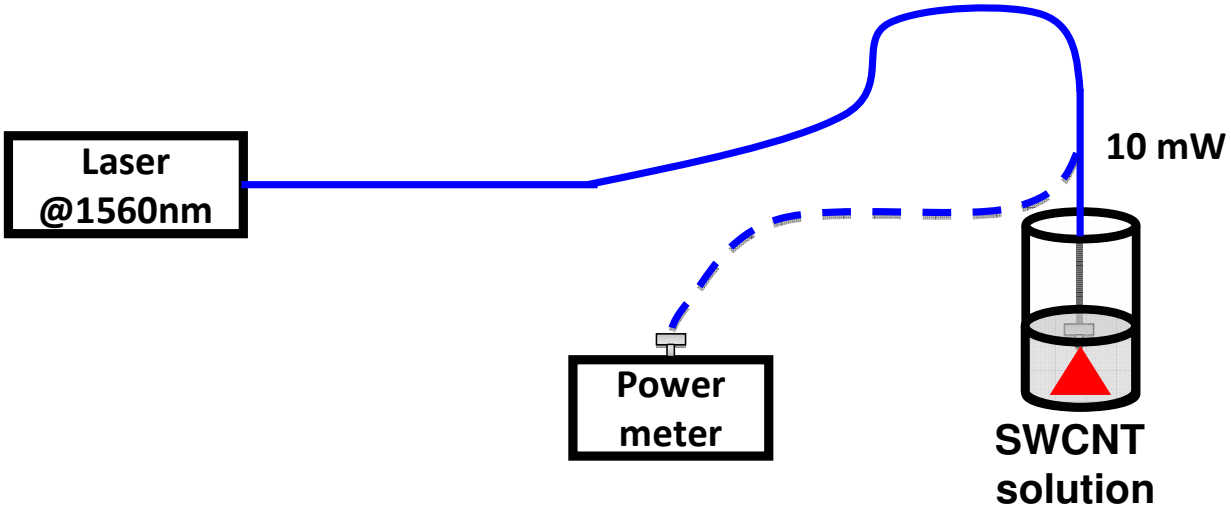

Figure 3.7 Scheme for the optically driven SWCNT deposition method. A fiber connector is dipped into the SWCNT solution and the CW laser possessing 10 mW at 1560 nm is radiated through the fiber connector. After 30 seconds radiation, the fiber connector is put out and is dried for a minute. Then the optical power is measured to check a loss. This process is repeated until the loss becomes ~ 2 dB.

Note: this technique was published by J. W. Nicholson *et al.*, "Optically driven deposition of single-walled carbon nanotube saturable absorbers on optical fiber end-faces," Optics Express 15, 9176–9183 (2007).

3.3.6 Damage of the SWCNT connector

The saturable absorber connector has realized an easy and simple incorporation of SWCNT but the problem of this saturable absorber connector is the damage from heat deposition. The saturable absorber connector was damaged as the cavity power was increased as shown in Figure 3.8, which limited the possible laser output power and spectral bandwidth. The optical power at 1560 nm affected the thermal damage in the saturable absorber connector. This problem needs to be solved to scale up the laser power. So far, the output power from our CNFLs is 1-2 mW using the optically driven SWCNT deposition method.

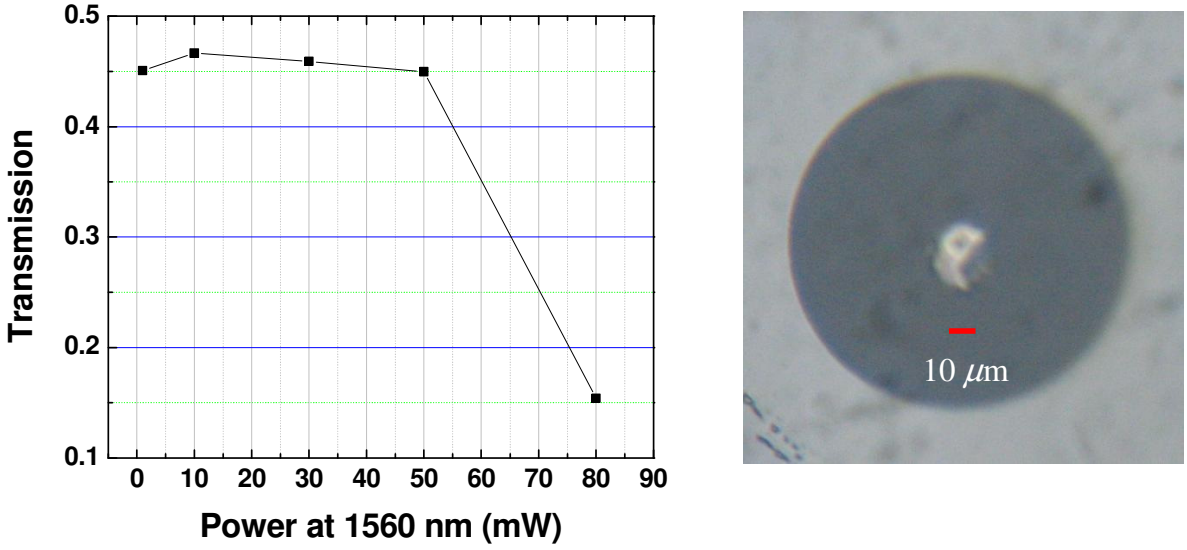

Figure 3.8 Typical Damage of fiber connector with SWCNT. (a) The transmission was measured as the power of a CW laser at 1560 nm was increased. The transmission of saturable absorber connector significantly decreased due to the heat damage at more than the power of 50 mW. (b) The damaged fiber connector end. The fiber (Dark gray circle) is 125 μm in diameter and the white spot is the damaged point.

3.4 Summary

The semiconductor saturable absorbers are desirable for the high repetition frequency mode-locked fibers. They can also be integrated into the laser cavity with simplicity. The mechanism behind the saturable absorption of the semiconductor saturable absorber is the excitonic absorption of the light and the recombination. The defect in semiconductor reduces the recovery time. The SWCNT is a type of semiconductor saturable absorbers and its bandgap energy can be tuned by changing the size of tube diameter. The metallic nanotubes act as a defect in SWCNT saturable absorbers.

The CNFL has shown the high repetition frequency which was realized in an all-fiber manner using the optically driven deposition method. The CNFL has many benefits as a frequency comb source such as easy and simple cavity fabrication, compactness, cost-effectiveness, and robustness. Nevertheless, the thermal damage should be avoided to make it more widely applicable mode-locked laser source to many research fields although the CNFL has shown a good performance in our research of optical frequency metrology. The output of CNFL is not high and therefore the output must be amplified for octave-spanning spectrum generation. The following discussion will be shown in next chapters.

Chapter 4 - Ultrashort Pulse Amplification and Compression for Supercontinuum Generation in Highly Nonlinear Fibers

4.1 Introduction to optical pulse amplification in gain fibers

The power achieved from the Er^{3+} doped fiber oscillators is limited commonly to the range from a milliwatt (mW) to tens of mW due to the dispersion and nonlinearity of fibers. However, in order to detect the carrier envelope offset frequency using the *f* to 2*f* self-referencing method, high peak intensity is required to generate more than an octave spectral bandwidth called the supercontinuum. The short and high peak intensity pulse has a benefit because it requires shorter length of fiber to generate the supercontinuum and can produce the wider supercontinuum [44]. In this chapter, we discuss backgrounds for the optical pulse amplification in gain fibers, which includes the atomic gain formulas and its related effects, such as gain saturation and gain narrowing. We also deliberated dispersion and nonlinearity affecting the pulse propagation in an Er^{3+} doped fiber amplifier (EDFA) [99]. The management of gain, dispersion, and nonlinearity is the key to generate high power optical pulses. Since the ultrashort pulse generation is critical in order to generate high peak intensity pulses, the compression of optical pulses is also an important technique. Here, the dispersion compensation with a hollow core photonic crystal fiber is discussed, which allows not only for preventing an amplified pulse from pulse distortion during the pulse compression because of very small nonlinearity of the fiber but also for an all-fiber high power ultrashort pulse EDFA.

The nonlinear Schrödinger equation (NLSE) derived from the Maxwell equations is discussed to theoretically understand the pulse evolution in fibers. By numerically solving the NLSE using the split step Fourier method, the pulse propagations in fibers are simulated.

The supercontinuum generation is a strong nonlinear process involved with higher order dispersions and four wave mixing such as self phase modulation and Raman scattering. In our research, the supercontinuum spectra from 1.0 μm to 2.2 μm were generated with the highly nonlinear fiber made by OFS using the pulse from our EDFAs.

4.1.1 Atomic resonant susceptibility

The atomic resonant susceptibility in a linear medium is related to the dispersion and loss (or gain) of the medium and those factors are important for understanding the amplification process. The resonance behavior of laser atoms in the applied electric field is responsible for the atomic resonant susceptibility.

4.1.1.1 Electric linear susceptibility

The steady-state response of a collection of atoms or electric dipole moments in a linear medium to the applied electric field is expressed as an electric susceptibility. The electric susceptibility therefore is the transfer function of the dielectric medium. The origin of electric susceptibility is the polarization of dipole moments produced by atoms. From the basic electromagnetic theory, the electric field in a dielectric medium is represented by the complex electric displacement, $\tilde{D}$, and by definition,

$$\tilde{D} = \varepsilon_0 \tilde{E} + \tilde{P}. \tag{4.1}$$

The tilde was used to stand for the complex electric field and polarization. In the equation, $\tilde{E}$ is the applied electric field, ε_0 is the dielectric constant of the vacuum, and $\tilde{P}$ is the polarization of the dielectric medium. When the dielectric medium is linear and isotropic, the polarization $\tilde{P}$ and the electric field $\tilde{E}$ are related with the following equation.

$$\tilde{P}(\omega) = \tilde{\chi}(\omega)\varepsilon_0 \tilde{E}(\omega), \tag{4.2}$$

so that the electric susceptibility of the medium represents the proportional factor of response of medium to the applied electric field and is defined by

$$\tilde{\chi}(\omega) \equiv \frac{\tilde{P}(\omega)}{\varepsilon_0 \tilde{E}(\omega)}, \tag{4.3}$$

then, the electric displacement, $\tilde{D}$, can be rewritten with the electric susceptibility and therefore

$$\tilde{D} = \varepsilon_0[1+\tilde{\chi}]\tilde{E} = \tilde{\varepsilon}\tilde{E}, \tag{4.4}$$

and where $\tilde{\varepsilon}$ is the complex dielectric constant defined by

$$\tilde{\varepsilon}(\omega) = \varepsilon_0[1+\tilde{\chi}(\omega)]. \tag{4.5}$$

4.1.1.2 Atomic susceptibility

The atomic susceptibility is a modified form of the electric susceptibility in the laser gain material. In practice, the resonant atoms are doped or imbedded into the host medium. Since the atoms of a host medium do not directly contribute to resonant transition for the laser action, we can rewrite the electric displacement in such a laser material as

$$\tilde{D} = \varepsilon_0\tilde{E} + \tilde{P}_{host} + \tilde{P}_{at}\,. \tag{4.6}$$

In the equation the contribution of the host medium is separated from that of the laser atoms. The response of the laser atoms has the weak and narrow bandwidth and therefore the laser atoms produce linear resonant polarization in the applied electric field. If we define $\tilde{P}_{host}$ as

$$\tilde{P}_{host} = \tilde{\chi}_{host}\varepsilon_0\tilde{E} \text{ and } \varepsilon_{host} = \varepsilon_0(1+\tilde{\chi}_{host}), \tag{4.7}$$

then the electric displacement can be written as

$$\tilde{D} = \varepsilon_{host}\tilde{E} + \tilde{P}_{at}\,. \tag{4.8}$$

In addition, let $\tilde{P}_{at} \equiv \varepsilon_0\tilde{\chi}_{at}\tilde{E}$ and $\varepsilon_0 \approx \varepsilon_{host}$. Then the final electric displacement is expressed as

$$\tilde{D} = \varepsilon_{host}\tilde{E} + \tilde{P}_{at} = \varepsilon_{host}[1+\tilde{\chi}_{at}]\tilde{E}, \tag{4.9}$$

which has the same form as our previous definition of electric displacement in the dielectric medium (Eq. 4.4), and the atomic susceptibility is defined as

$$\tilde{\chi}_{at}(\omega) \equiv \frac{\tilde{P}_{at}(\omega)}{\tilde{\varepsilon}_{host} E(\omega)}. \tag{4.10}$$

4.1.1.3 Resonance behavior of atoms and its susceptibility

Atoms in the laser gain medium show resonant behavior in the applied electric field. When the laser medium is approximated to a collection of resonant oscillators, the susceptibility can be written as

$$\tilde{\chi}_{at}(\omega) \equiv \frac{P_{at}(\omega)}{\tilde{\varepsilon}_{host} E(\omega)} \equiv C_0 \frac{1}{\omega_a^2 - \omega^2 + i\omega\Delta\omega_a}, \tag{4.11}$$

where C_0 is a constant defined as $\frac{-iNe^2}{m_e \omega_a \varepsilon \Delta\omega_a}$ which is related to the resonant behavior of the atomic systems. N is the number of electric dipoles, e is the charge of an electron, m_e is the mass of the electron, i=$(-1)^{1/2}$ and ω_a is the resonance frequency. The $\Delta\omega_a$ is very small compared to the resonant frequency and related to the dephasing time of oscillators. More details about this can be found in Ref. [138]. With the resonance approximation, the atomic susceptibility can be expressed as

$$\tilde{\chi}_{at}(\omega) \approx -iC_0 \frac{1}{1 + 2i(\omega - \omega_a)/\Delta\omega_a} = -iC_0 \frac{1}{1 + i\Delta x}, \tag{4.12}$$

where $\Delta x = 2\frac{\omega - \omega_a}{\Delta\omega_a}$. This type of equation is known as the complex Lorentzian lineshape and therefore the atomic susceptibility has the form of

$$\tilde{\chi}_{at}(\omega) \equiv \chi'(\omega) + i\chi''(\omega) = -C_0\left[\frac{\Delta x}{1+\Delta x^2} + i\frac{1}{1+\Delta x^2}\right], \tag{4.13}$$

where $\chi'(\omega)$ and $\chi''(\omega)$ are the real and imaginary parts of the atomic susceptibility function. We will use this complex susceptibility function to understand dispersion and gain in optical fiber amplifiers. In Chapter 2, there was a brief discussion about the self-starting and the real part of atomic susceptibility was used to explain it. The $\chi'(\omega)$ is related to the reactive, or phase-shift, or dispersive part of the atomic response and the $\chi''(\omega)$ is related to the resonant response such as the absorption or amplification of the atomic response.

4.1.2 Laser power amplification with an erbium doped fiber amplifier

Since the average power generated from CNFL is in general small (an order of mW), the EDFA is used to amplify pulses. The purpose of pulse amplification is to generate a supercontinuum spectrum that is a coherent spectrum source possessing more than an octave in spectral bandwidth. Then we used the supercontinuum spectrum to detect the CEO frequency. The larger pulse amplification is required for the higher repetition frequency mode-locked laser to achieve the same pulse energy because total average power is split by the number of pulses. In general, more than 1 nJ pulse energy is required to generate enough supercontinuum spectrum with a highly nonlinear fiber (HNLF), which is specially designed to generate a supercontinuum spectrum from a 1550 nm pulse laser source [100]. The CNFL we used in our experiment has a 167 MHz repetition frequency. In order to support the 1 nJ pulse, the 170 mW average power is demanded at the 167 MHz repetition frequency. Our CNFL has a 1 mW average power; therefore we needed at least 22 dB of integrated optical gain from the EDFA. In our experiment, we obtained the amplification of 26 dB with the EDFA using the parabolic pulse amplification. The optical wave-breaking [101] during the pulse amplification caused by the interplay between dispersive effects and nonlinear effects was not observed.

4.1.2.1 Laser power amplification in the single pass gain of Er^{3+} doped fiber

By solving the Maxwell equations with the electric displacement in the laser medium and the paraxial approximation of light propagation, we can derive an equation for the light propagation. The paraxial approximation is valid for the fiber laser because the beam is tightly

confined in fibers and therefore the change in the transverse component of the electric field can be ignored. Hence the axial component of the complex electric field has the following form in the frequency domain.

$$\tilde{A}(z,\omega) = A_0(\omega)\exp\left\{-i\left[\beta(\omega)+\Delta\beta_m(\omega)\right]z + i\varphi_0(\omega)\right\}\times\exp\left\{\left[g_m(\omega)-\alpha_0\right]z\right\}, \tag{4.14}$$

where $A_0(\omega)$ is the pulse envelope in the frequency domain and $\Delta\beta_m(\omega)$ is the additional atomic dispersion produced by the atomic gain defined as

$$\Delta\beta_m(\omega) = (\beta/2)\chi'(\omega), \tag{4.15}$$

and $g(\omega)$ is the atomic gain or loss coefficient defined as

$$g_m(\omega) = (\beta/2)\chi''(\omega). \tag{4.16}$$

α_0 is the loss from the medium and $\varphi_0(\omega)$ is the initial spectral phase. In those definitions, the real and imaginary atomic susceptibility we discussed in the previous section were included. In practice, the atomic gain (or loss) function is not a single Lorentzian function (susceptibility function), but rather the sum of many Lorentzian functions because the erbium atoms have many resonance frequencies induced by the Stark shift [139] and therefore the actually gain and loss dynamics is a more complicated process. In addition, the electric field we used here only includes the dispersive effect of the medium and does not include the nonlinear effect. The nonlinear effect in the laser amplification will be discussed with introducing the nonlinear Schrödinger equation (NLSE) in later sections. Even if this is a simple approach for the laser power amplification, it explains many interesting phenomena in the laser amplification process.

Single pass laser gain formulas

Fiber amplifiers, for example EDFAs, have a single pass laser gain process. Here the gain can be represented using complex notation. The complex gain in the laser gain fiber in the length of L is written as

$$\tilde{g}(\omega) \equiv \frac{\tilde{A}(L,\omega)}{\tilde{A}(0,\omega)} \approx \exp\{-i[\beta(\omega)+\Delta\beta_m(\omega)]L\} \times \exp\{[g_m(\omega)-\alpha_0]L\}. \quad (4.17)$$

Because we measure the intensity (I ~A^2) in the experiment, the single pass intensity gain is the magnitude of the complex gain so that

$$G(\omega) \equiv |\tilde{g}(\omega)|^2 = \exp[2g_m(\omega)L - 2\alpha_0 L]. \quad (4.18)$$

Because the material loss α_0 is generally much smaller than the optical gain, the equation is even more simplified as $G(\omega)=\exp[2g_m(\omega)L]$. By substituting Eq. (4.16),

$$G(\omega) = \exp[\beta\chi''(\omega)L] = \exp\left[\frac{\omega L}{c}\chi''(\omega)\right]. \quad (4.19)$$

The gain shape is determined by the imaginary part of the susceptibility. Note that practically we measure $G(\omega)$ rather than $\chi''(\omega)$.

4.1.2.2 Gain narrowing

If we assume that the $\chi''(\omega)$ has a simple Lorentzian shape, then Eq. (4.19) can be expressed as

$$G(\omega) = \exp\left[\frac{\omega L}{c}\chi''(\omega)\right] = \exp\left[\frac{\omega L}{c}\frac{\chi_0''}{1+[2(\omega-\omega_a)/\Delta\omega_a]^2}\right], \quad (4.20)$$

where χ_0'' is the midband value which is a constant and ω_a is the resonant frequency. We then convert $G(\omega)$ into power gain in decibels (dB) and we will see that

$$G_{dB}(\omega) \equiv 10\log_{10} G(\omega) = \frac{4.34\omega_a L}{c}\chi''(\omega). \quad (4.21)$$

Since the $\chi''(\omega)$ is in the exponent of the gain expression (Eq. 4.20), the gain falls off quickly from the resonance frequency. If we defined the full width half maximum (FWHM) or the 3 dB bandwidth ($\Delta\omega_{3\mathrm{dB}}$) where the $G(\omega)$ is a half of maximum value, then the $\Delta\omega_{3\mathrm{dB}}$ is represented as

$$\Delta\omega_{3dB} = \Delta\omega_a \sqrt{\frac{3}{G_{dB}(\omega_a) - 3}}\,. \tag{4.22}$$

Therefore when the maximum peak gain at ω_a increases, the gain bandwidth decreases. This is known as the gain narrowing. We have explained the gain narrowing with a single Lorentzian shape of $\chi''(\omega)$ but this is generally true for different gain shapes. Therefore when one designs the amplifier with the broad spectral bandwidth, the gain narrowing effect should be considered.

4.1.2.3 Atomic phase shift

The amplifier adds not only the gain but also adds the phase shift induced by the $\chi'(\omega)$ during the pulse propagation. This additional phase shift related to the $\chi'(\omega)$ is given by the following equation when you assume a single Lorentzian form of the atomic susceptibility.

$$\Delta\beta_m(\omega)L = \left(2\frac{\omega-\omega_a}{\Delta\omega_a}\right) \times g_m(\omega)L = \frac{G_{dB}(\omega_a)}{20\log_{10} e} \times \frac{2(\omega-\omega_a)/\Delta\omega_a}{1+\left[2(\omega-\omega_a)/\Delta\omega_a\right]^2}\,. \tag{4.23}$$

4.1.2.4 Gain saturation

In order to achieve efficient energy extraction, the pulse should be intense enough to saturate the population inversion during the propagation through the gain medium. However, this causes the reduction of gain in time. We will discuss the saturation intensity and saturation fluence of a pulse. Both are intrinsic properties of a gain medium and do not depend on pump intensity.

Saturation analysis of a CW laser

In the amplification process, the available gain is saturated with a large input signal. For the CW laser amplification, the saturation intensity can be calculated with the formula defined as

$$I_{sat} \equiv \frac{\hbar\omega}{\sigma\tau_{eff}}, \tag{4.24}$$

where σ is the transition cross section of the atoms representing the capacity to absorb power per unit area, τ_{eff} is the recovery time, and $\hbar$ is the Planck constant. The saturation intensity is inversely proportional to the cross section and the recovery time. Hence the larger the cross section is, the smaller the saturation intensity is, and the longer the recovery time is, the smaller saturation intensity is. However, the saturation intensity we define here is valid for the amplification of CW laser sources with the given pump power and the temperature. In order to have a sense for the saturation intensity of Er^{3+} atoms in fibers, we are, for example, able to calculate the saturation intensity at 1550 nm. The cross section of Er^{3+} atoms in fibers has on the order of 10^{-21} cm^2 at 1550 nm [102] and varies with the doping concentration and the temperature. The recovery time is on the order of milliseconds (ms). Then the saturation intensity (I_{sat}) is about 10^4-10^5 W/cm^2. The corresponding power with a core of the radius of 4 μm optical fiber (Area = 5.3×10^{-7} cm^2) is 1 to 10 mW. Due to the strong confinement of pulses in fibers, the saturation power is quite small. In general, the available power from an amplifier is proportional to the saturation intensity, so that the fundamental limitation of the amplification exists for the small core Er^{3+} doped fiber laser amplifier with the given pump power. Therefore, for high power CW laser amplification, the large mode area fibers are commonly used.

Saturation analysis of a pulsed laser

Since an ultrashort pulse has very broad spectral bandwidth, it is very difficult to analytically calculate the saturation intensity and saturation behavior during the pulse amplification. In the case of ultrashort pulse amplification, the frequency dependence of saturation intensity also needs to be considered. Especially for the EDFA, the pulse energy increases along the long interaction length with fibers, and therefore the dispersive effects and nonlinear effects are more complicatedly involved. Practically, when the pulse width concerned is long enough and the pulse propagation length in a gain medium is short enough, an approximate analysis can be used known as the Frantz-Nodvik analysis that is a homogenous saturation analysis [140]. This pulse amplification might be understood using this approximation even if the dispersive and nonlinear effects might be large and some situations might be different

in the relatively long length of EDF. For the pulse laser amplification, we can define a useful quantity known as the saturation energy per unit area, U_{sat} (sometimes called the saturation fluence) for an atomic gain medium by

$$U_{sat} \equiv \frac{\hbar\omega}{\sigma}. \tag{4.25}$$

This quantity is obviously the analog to the saturation intensity described in Eq. (4.24) for the pulse input. For instance, the Er^{3+} atom has the saturation intensity of ~100 J/cm^2. Therefore the saturation energy in a core radius of 4 μm EDF is about 50 μJ. For example, when a Gaussian pulse possessing the average power of 400 mW, the pulse repetition of 167 MHz, and the pulse duration of 7 ps has the pulse energy of 2.4 nJ. Note that the numbers we have shown here are practical values used in our EDFA, and therefore the EDFA we discuss in this chapter does not work at the saturation regime because the pulse energy we are dealing with is on the order of 1 nJ.

The gain saturation also affects the pulse shaping because the pulse leading edge saturates the gain medium, the trailing edge is not equivalently absorbed by the gain medium. The result is the pulse-shape distortion, which is the shift of the pulse peak to the pulse leading edge. In general, the gain in time, $G(t)$ is related by

$$G(t) \approx \exp\left[-U_{out}(t)/U_{sat}\right], \tag{4.26}$$

where U_{out} is the time varying output pulse energy per unit area. Therefore, when U_{out} is larger than U_{sat}, the gain exponentially decreases with time.

4.1.2.5 Slope efficiency

Previously, we discussed the gain saturation. The saturation fluence is an intrinsic quantity of a gain medium which is not changed. Therefore, in order to extract more energy from an amplifier one should increase a small signal gain which is explained by the extraction energy (U_{extr}) equation defined as below.

$$U_{extr} = U_{sat} \times \ln\left(\frac{G_0}{G_f}\right), \tag{4.27}$$

where G_0 is the small signal gain (or unsaturated gain) and G_f is the final gain. G_0 can be increased by pumping the gain medium harder. When the applied pump power is high enough, the extractable output intensity is linearly proportional to the applied pump power. The relationship is called the slope efficiency and therefore the slope efficiency is defined by the ratio between the output power and the applied pump power. For example, the parabolic pulse EDFA we made has shown the integrated gain of 26 dB (amplified from 1 mW to 430 mW) with the pump power of 1.15 W and its slope efficiency of 37 % as shown in Figure 4.1. Its output power was limited by the available pump power. The details of the parabolic pulse amplifier will be explained in following sections.

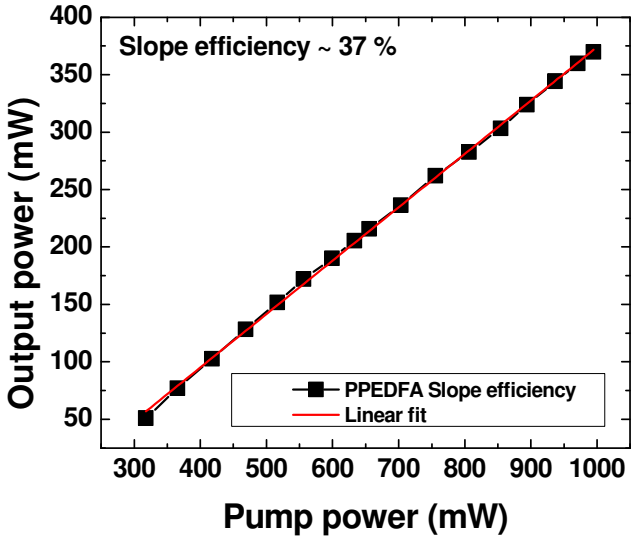

Figure 4.1 Slope efficiency of a parabolic pulse EDFA which has shown the slope efficiency of 37 %. The output power is linearly proportional to the applied pump power when the applied pump power is high enough.

4.2 Ultrashort pulse Er^{3+} doped fiber amplifiers

4.2.1 Ultrashort pulse propagation in Er^{3+} doped fiber amplifiers

When an ultrashort pulse propagates through fibers, nonlinear effects are much more critical in the laser amplification because the short pulse source has much higher peak intensity than that of a CW laser source. In Chapter 2, we have already discussed the origin of nonlinear effects. This is because of the nonlinear refractive index and its intensity-dependence. In this section, we will discuss how nonlinear effects affect the pulse propagation and interact with dispersive effects in an EDFA. In the earlier section, we only considered the linear effect of polarization ($\chi^{(1)}$), which explained the gain (or loss) of a medium and the gain-induced phase shift. However, when a pulse source possessing high peak intensity is considered, the higher order susceptibilities play important roles in the pulse propagation. As we discussed before, the $\chi^{(3)}$ is the lowest order nonlinear contribution and creates SPM and XPM during the pulse propagation in fibers. Those nonlinear effects generate new frequency components and nonlinear phase shift. The contribution of nonlinear effects, dispersive effects, and their interactions can be numerically explained by the nonlinear Schrödinger equation (NLSE) which we will explore here.

4.2.1.1 Nonlinear Schrödinger equation (NLSE) for undoped fibers

The pulse propagation in fibers can be analytically solved with the NLSE. The NLSE can be derived from the Maxwell equation. (See Appendix C) For the simplest case of pulse propagations, we can just consider GVD and SPM. This is true if we consider the decent pulse energy and spectral bandwidth (see an example in Section 4.2.1.4) in a standard single mode optical fiber at 1550 nm, so that high order dispersions and high order nonlinearities can be ignored. In this case, the NLSE for a fiber without gain is

$$\frac{\partial \tilde{A}}{\partial z} + \beta_1 \frac{\partial \tilde{A}}{\partial t} + \frac{i\beta_2}{2}\frac{\partial^2 \tilde{A}}{\partial t^2} + \frac{\alpha}{2}\tilde{A} = i\gamma \left|A\right|^2 \tilde{A}, \tag{4.28}$$

where $\tilde{A}$ is the slowly varying complex pulse envelope, $\beta_1=1/v_g$, β_2 is GVD, α is the loss, and γ is the effective nonlinearity defined in Chapter 2. Although this equation is used for standard optical fibers it can be modified (Eq. 4.34) to include gain and gain dispersion associated with a pumped EDF. Since the loss of the standard single mode fiber is only 0.2 dB/km at 1550 nm, the loss term can be ignored. Further simplification can be done by considering the reference frame moving with the pulse at the group velocity, v_g (the so-called retarded frame). By making the transformation as

$$T = t - z/v_g \equiv t - \beta_1 z, \tag{4.29}$$

Eq (4.28) becomes even simpler which is then,

$$i\frac{\partial \tilde{A}}{\partial z} - \frac{\beta_2}{2}\frac{\partial^2 \tilde{A}}{\partial T^2} + \gamma |A|^2 \tilde{A} = 0. \tag{4.30}$$

4.2.1.2 Split Step Fourier Method

In order numerically to solve NLSE, we used the split step Fourier method (SSFM). This method is well explained in Ref. [132]. Here we briefly introduce its idea behind SSFM. The NLSE can be written in the operator form of

$$\frac{\partial \tilde{A}}{\partial z} = (\hat{D} + \hat{N})\tilde{A}, \tag{4.31}$$

where $\hat{D}$ is a dispersion operator that represents for dispersion and absorption (or gain) in a linear medium and $\hat{N}$ is a nonlinear operator that is responsible for the nonlinear effects on the pulse propagation in optical fibers. Therefore the dispersion operator and the nonlinearity operator are given by

$$\begin{aligned} \hat{D} &= -\frac{i\beta_2}{2}\frac{\partial^2}{\partial T^2} - \frac{\alpha}{2}, \\ \hat{N} &= i\gamma |A|^2 \end{aligned} \tag{4.32}$$

Generally, dispersion and nonlinearity are not independent but they are coupled when the pulse propagates in fibers. However, we can get an approximate solution by assuming the small enough propagation length so that we can apply dispersion operator and nonlinear operator independently. So the solution of Eq. (4.31) can be written as

$$\tilde{A}(z+h,T) = \exp\left[h\left(\hat{D}+\hat{N}\right)\right]\tilde{A}(z,T), \tag{4.33}$$

where h is the step size. In order to understand this method, we schematically illustrated the SSFM in Figure 4.2. We apply the dispersion operator in the frequency domain and implement the nonlinearity operator in the time domain. These steps can numerically be done with the fast Fourier transformation. The total propagation length in fibers is split by small step sizes h (typical value we use is 0.5 mm) and dispersion and nonlinearity are separately calculated in each step.

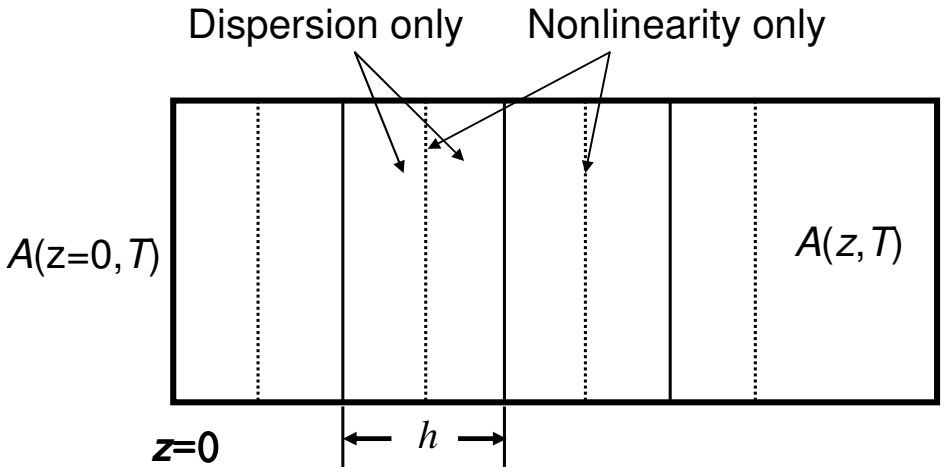

Figure 4.2 The schematic illustration of the SSFM for the numerical simulation with MATLAB. The total propagation length is split by small step sizes (*h*) and the dispersion and nonlinearity are separately computed in a small step size. Dispersion is calculated in the frequency domain and nonlinearity is computed in the time domain. The typical step size we use is 0.5 mm. Reproduced from Ref. [141]

4.2.1.3 The role of GVD and SPM during pulse propagation in optical fibers

We study the role of GVD and SPM and their interaction during the pulse propagation by numerically solving the NLSE, Eq (4.30). Remember that this is true for the low pulse energy in

a standard single mode fiber. When the pulse energy increases or we use specially designed optical fibers, we should consider different types of nonlinearities and higher order dispersions. These will be discussed later.

Group Velocity Dispersion (GVD) only

In this case, the effective nonlinearity (γ) is set to zero in Eq. (4.30) and GVD is responsible for the pulse broadening in the time domain. Since an ultrashort pulse has broad spectral components which propagate through fibers with different velocities, the final pulse becomes broad but the pulse spectrum is intact with GVD alone. Figure 4.3 shows the simulated result using the SSFM. The initial transform-limited sech^2 pulse duration of 65 fs (FWHM) corresponding to spectral bandwidth of 40 nm (FWHM) is launched into the Corning SMF-28e length of 1 m. Due to GVD, the pulse becomes broad and the final pulse has the pulse duration of 690 fs at FWHM and achieves the parabolic temporal phase distortion. In addition, the chirp is defined by the time derivative of the temporal phase and therefore for example, the parabolic phase is linearly chirped.

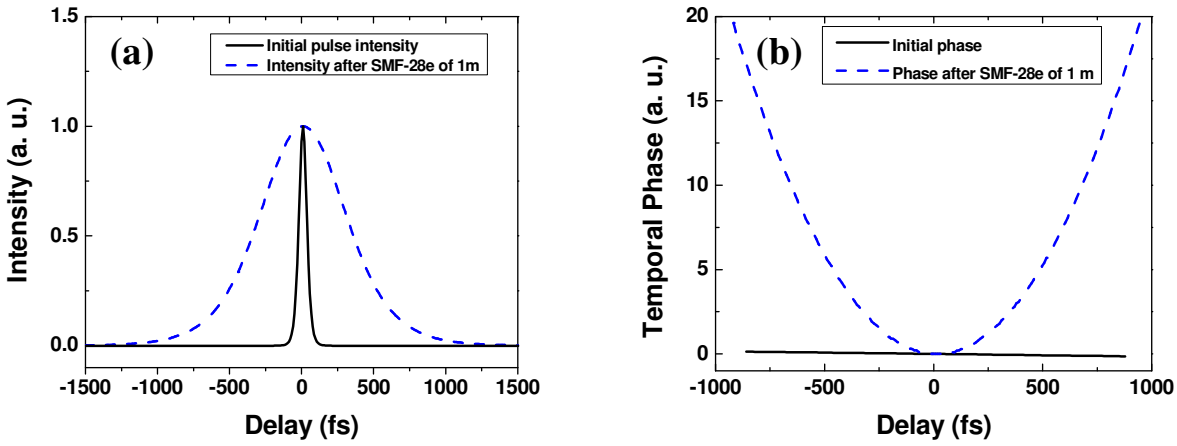

Figure 4.3 A simulation result of pulse broadening in the Corning SMF-28e with GVD alone. The initial transform limited sech^2 pulse duration of 65 fs (FWHM) corresponding to spectral bandwidth of 40 nm (FWHM) is launched into the fiber length of 1 m (a) Broadened pulse duration due to GVD. (b) Parabolic temporal phase due to negative GVD of the Corning SMF-28e. Note that the initial pulse has a constant phase.

Self-Phase Modulation (SPM) only

As we have seen in Chapter 2, the intensity dependent of the refractive index in optical fibers produces the nonlinear phase shift that is responsible for SPM. This leads to spectral broadening of optical pulses. In the form of frequency chirp we define in Chapter 2, we can see interesting features of SPM-induced nonlinear phase shift. $\delta\omega_{NL}$ is negative near the leading edge (red shift) and becomes positive near the trailing edge (blue shift) of the optical pulse. In addition, it shows a linear and positive up-chirp over a central portion of the optical pulse. The spectral broadening and nonlinear phase shift introduced by SPM is simulated and illustrated in Figure 4.4 where the effect of GVD was ignored. A transform-limited pulse possessing the peak power (P_0) of 4.9 kW centered at 1560 nm was launched into the Corning SMF-28e length of 1m possessing the effective nonlinearity (γ) of 1.42 $W^{-1}km^{-1}$, which corresponds to the nonlinear length of 14 cm. The final pulse spectrum was significantly broadened and the nonlinear phase shift or positive frequency chirp was produced in the central spectral region.

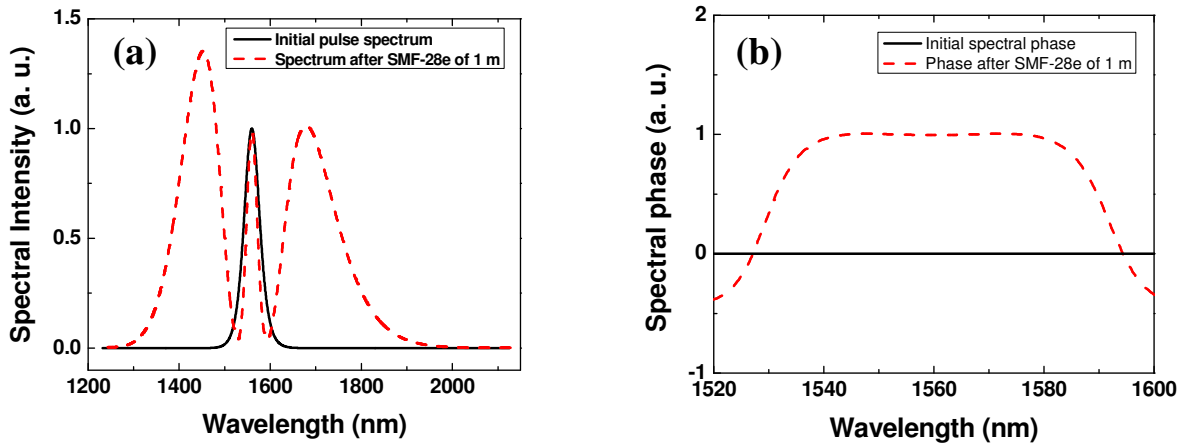

Figure 4.4 (a) A simulation result of spectral broadening due to SPM only. (b) Its spectral phase which is positively linear chirped near the central region of the optical pulse. The input pulse has the peak power (P_0) of 4.9 kW centered at 1560 nm. The Corning SMF-28e has the effective nonlinearity (γ) of 1.42 $W^{-1}km^{-1}$.

In summary, we took a look at the role of GVD and SPM independently in pulse propagation in the Corning SMF-28e by numerically simulating NLSE. GVD was responsible for the pulse broadening and SPM was in charge of creating new spectral components and frequency up-chirp in the central frequency region. The pulse propagation is more complicated

due to the interplay of dispersion and nonlinearity. One of the best examples for the case is a soliton pulse. The soliton pulse discussed in Chapter 2 can be formed in the negative dispersion fiber (β_2 <0). This is because the positive nonlinearity-induced frequency chirp is compensated by the negative GVD-induced frequency chirp by the fiber. Therefore the net frequency chirp becomes zero so that the pulse can be propagated through the optical fiber without changing its temporal and spectral shape.

4.2.1.4 Ultrashort pulse propagation in a gain fiber

In the previous section, we were dealing with the propagation of a low intense pulse in the single mode fused silica fiber and investigated the roles of GVD and SPM and briefly explained the soliton that is a form of NLSE's solution originated from the interplay between GVD and SPM. Now we will move to more complicated situation where the pulse propagates in a gain fiber. In our parabolic pulse EDFA, the dispersive effects are quite large due to the relatively long propagation length. At the same time the pulse obtains a substantial gain so that pulse energy increases and therefore the nonlinear effects could also become stronger. In some cases of the high power pulse amplification, we need to consider possible higher order $\chi^{(3)}$ nonlinear effects in optical fibers causing asymmetry to the spectrum such as the stimulated Raman scattering (SRS) and the self steepening (SS) [103] into NLSE in order to investigate the pulse evolution. Moreover, dispersion and nonlinearity interacts each other in more sophisticate manner.

Practically, there were some difficulties to explain experimental data of pulse evolution in EDF with numerical simulations because we were not able to effectively include the exact spectral gain shape and bandwidth, gain narrowing effect, signal re-absorption by EDF, the pump power depletion, and higher order dispersions. However, the simulation has shown good agreements with experimental data in the conditions of the decent pulse power amplification and the relatively short length of EDF.

NLSE for ultrashort pulse propagation in an Er^{3+} doped fiber

Higher order nonlinearities were not considered in this simulation and this could be true when the pulse possessing decent pulse energy and spectral bandwidth is dealt, which is our case. The simulation starts with the NLSE, Eq. (4.30). Since we have a gain, we should take it account in the equation. Then,

$$i\frac{\partial \tilde{A}}{\partial z} - \frac{\beta_2}{2}\frac{\partial^2 \tilde{A}}{\partial T^2} + \gamma |A|^2 \tilde{A} - i\frac{g_m(\omega)}{2}\tilde{A} = 0, \tag{4.34}$$

where $g_m = g_m(\omega,T)$ is the gain coefficient. Since the saturation energy is much larger than the pulse energy we are considering, the time-dependence of gain coefficient is ignored. Then the dispersion and nonlinearity operator becomes

$$\begin{aligned} \hat{D} &= -\frac{i\beta_2(\omega)}{2}\frac{\partial^2}{\partial T^2} + \frac{g_m(\omega)}{2}, \\ \hat{N} &= i\gamma|A|^2 \end{aligned} \tag{4.35}$$

In practice, the gain is also dependent on the propagation distance but we practically can make the constant gain along the gain fiber by bi-directionally pumping it or use relatively short length of fiber. There is a useful tip to determine the length of EDF without pump depletion. We choose the fiber length at the given pump power using the green fluorescence which becomes dimmer along the fiber when the pump begins to be depleted.

Frequency dependent of gain coefficient

As we discussed in the previous section, the gain profile is proportional to the atomic susceptibility. EDF has a broad gain bandwidth and it is not a simple Lorentzian profile rather than it can be represented by the sum of Lorentzian functions. In order to find the frequency dependence (or wavelength dependent) of EDF, we measured the optical gain at different wavelengths. A tunable CW laser (Santec) was used and its tunable wavelength range was from 1510 nm to 1580 nm which covered most of Er^{3+} gain bandwidth. The measured wavelength-dependent gain is shown in Figure 4.5. The gain bandwidth was ~55 nm at FWHM and the peak gain was obtained at 1560 nm. We normalized the gain profile with the peak gain value. This normalized gain profile is a reasonable approximation of the frequency-dependent gain profile. Therefore we imported this gain profile into our numerical simulations.

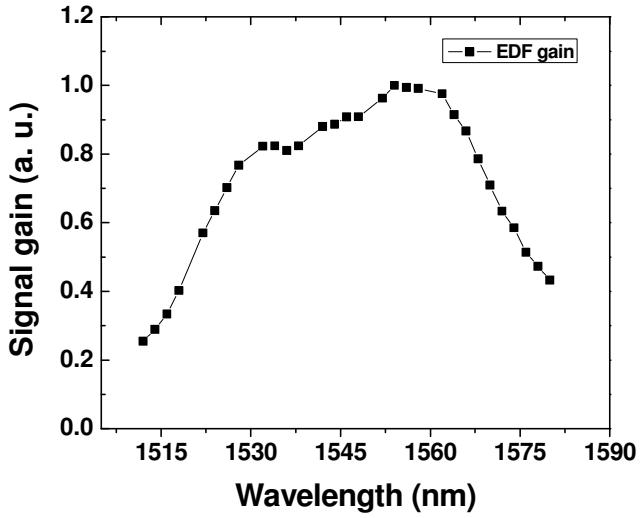

Figure 4.5 Wavelength-dependent gain of EDF (Liekki Er110). The gain is measured with a tunable CW laser. The gain bandwidth was ~55 nm at FWHM and the maximum gain was obtained at around 1560 nm.

A simulation of ultrashort pulse propagation in an EDFA

The following approximations were made before this simulation.

1) Gain is constant through the propagation distance in EDF and the frequency-dep endent profile in Figure 4.5 is used in simulation.
2) The higher order dispersions of EDF are small enough and the pulse spectral ban dwidth is reasonable narrow to ignore those higher order dispersion effects.
3) Pulse energy is much lower than gain saturation energy and the possible higher order nonlinearities only have a negligible effect.

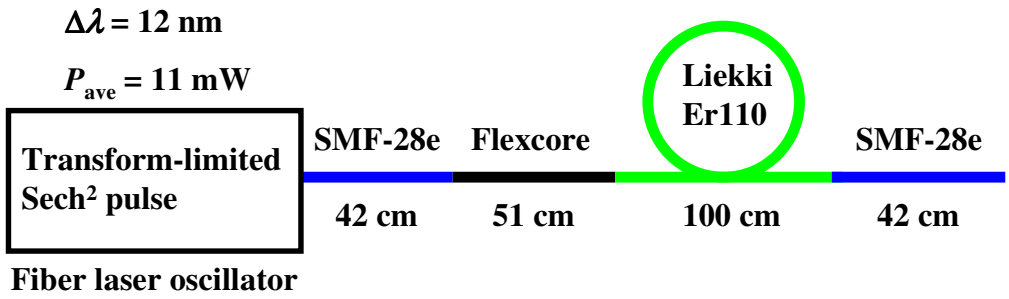

Figure 4.6 The EDFA simulation set-up. The seed pulse ($Sech^2$) has the average power (P_{ave}) of 11 mW and the spectral bandwidth ($\Delta\lambda$) of 12 nm.

A transform-limited sech^2 pulse possessing the average power of 11 mW and the gain bandwidth of 12 nm (FWHM) centered at 1570 nm is launched into Liekki Er110 fiber length of 1 m. The repetition frequency is 57 MHz. There are a Corning SMF-28e length of 42 cm and a Corning flexcore length of 51 cm before Liekki Er110 and a Corning SMF-28e length of 57 cm after EDF for the pulse compression. This simulation was done by solving Eq. (4.34) with SSFM. The properties of fibers used in this simulation are summarized in Appendix H. The results are shown in Figure 4.7.

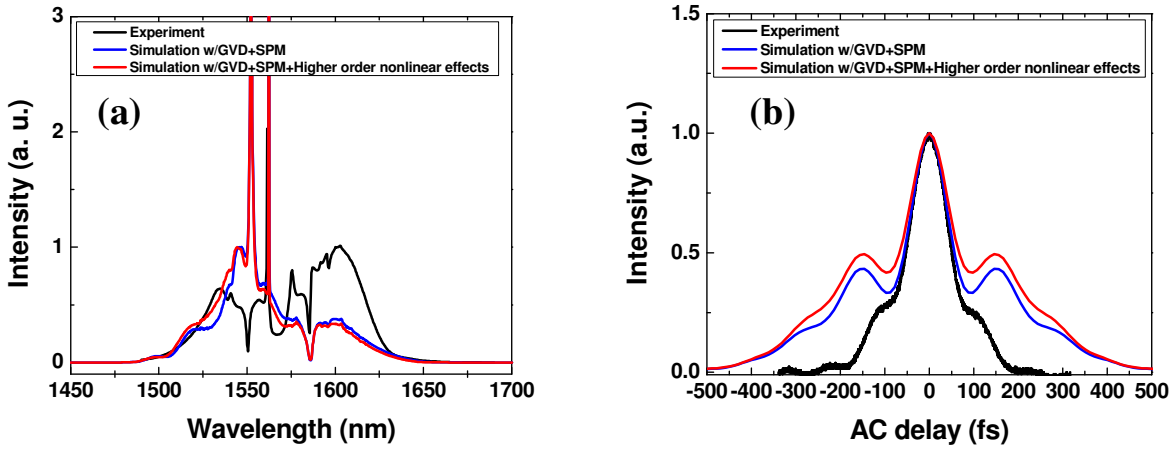

Figure 4.7 (a) Comparison between experimental spectrum and simulation spectra. One of them (Blue) included only GVD and SPM and showed a good agreement in its overall spectral bandwidth and particular features in spectrum. The other one considered higher order nonlinear effects but the spectrum has not noticeably changed. This was because the peak intensity was not high enough to make higher order nonlinear effects significant. (b) Comparison between experimental intensity autocorrelation (AC) and the simulated AC. They had the same pulse width (FWHM) and had pedestals due to nonlinear effects.

The integrated gain was 8.34 dB in the experiment at the given pump power and we derived the gain coefficient (g) of 1.354 m^{-1} from that. The GVD of Liekki Er110 was calculated by cutting-back fiber method and it was +1.107 × 10^{-5} fs^2/nm. The GVD of Corning SMF-28 is -2.408 × 10^{-5} fs^2/nm from the manufacturer and the GVD of Corning flexcore is -4.5 × 10^{-6} fs^2/nm measured by JILA. The effective nonlinearity (γ) of EDF (Liekki Er110) was 3.66 W^{-1}km^{-1} and the $\gamma$of the Corning SMF-28e was 1.43 W^{-1}km^{-1}. The spectrum and the intensity autocorrelation (AC) between the experiment and the simulation have shown good agreements. Total spectral

bandwidth and particular features were well matched even though higher order nonlinear effects such as stimulated Raman scattering, self-steepening were ignored because of its relatively low peak intensity as shown in Figure 4.7. The discrepancies between the experiment and the simulation may be caused by higher order dispersions, gain dispersion, and their interplays which are not included in the simulation, in addition to them, due to the possible inaccuracy in the frequency dependent gain and the gain distribution along the EDF.

4.2.2 Parabolic pulse amplification

We studied an interesting pulse evolution dynamics called the parabolic pulse amplification in an EDFA. When a pulse propagates a positive dispersion fiber, the pulse experiences the optical wave-breaking due to the interplay between GVD and SPM [101, 104]. This phenomenon degrades the pulse by creating the oscillatory structure near pulse edges and the sidelobes in the spectrum as shown in Figure 4.8.

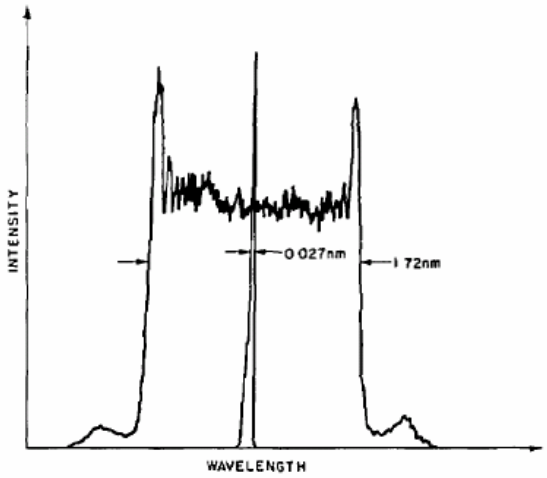

Figure 4.8 Optical wave-breaking. The input spectrum was stretched and the sidelobes were created due to the interplay between GVD and SPM. Reproduced from Ref. [104].

However, there is an interesting pulse evolution when a pulse propagates in the positive dispersion fiber with an optical gain, which is known as the parabolic pulse or similariton [105-108]. In the negative dispersion gain fiber, the pulse is broken to many soliton pulses called the soliton fission due to the various effects such as higher order dispersions and nonlinear effects [109]. The parabolic pulse is an asymptotic solution of NLSE when the appropriate positive GVD, SPM and optical gain exist. In order to obtain parabolic pulse with EDFA in the experiment, there are important factors. First, the long enough propagation length for asymptotic

behavior and large accumulated positive dispersion are required. Therefore, we used about 10.5 m of Er^{3+} doped fiber (EDF). Secondly, the control of optical gain and nonlinearity is crucial. In our experiment, the choice of EDF and the control of pump power affect those parameters.

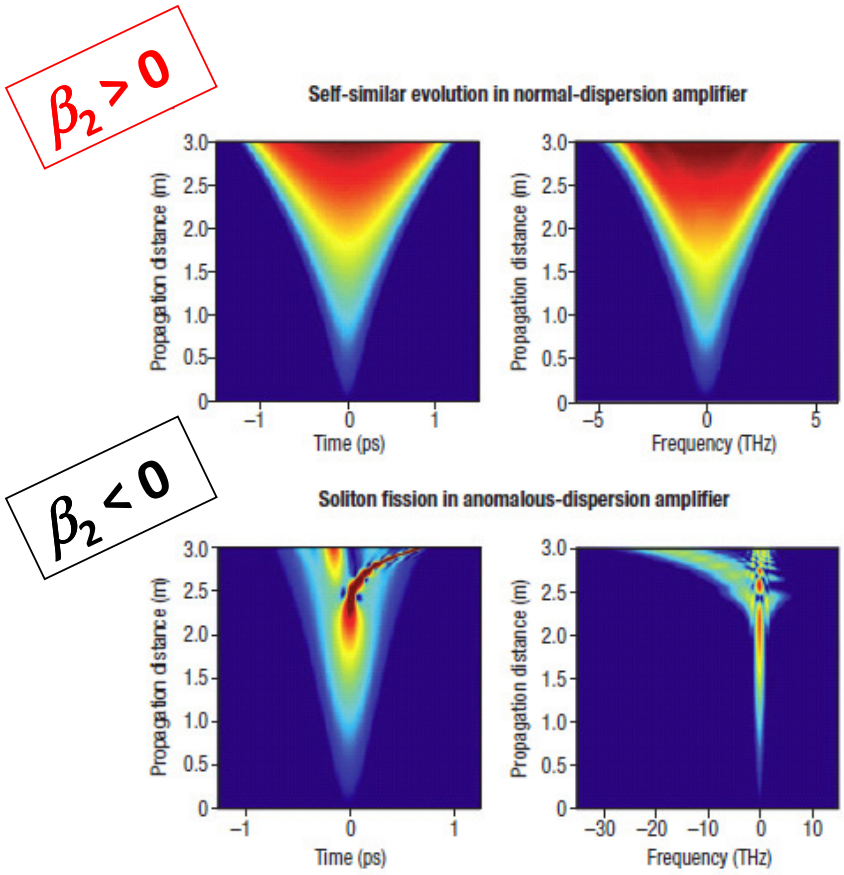

Figure 4.9 A self-similar evolution in normal dispersion amplifier. When dispersion is positive, the pulse can propagate in amplifier without breaking its pulse shape but when dispersion is negative, the pulse is broken due to the various effects such as higher order dispersions and nonlinear effects. Reproduced from Ref. [108].

4.2.2.1 Properties of the parabolic pulse

The parabolic pulse (or similariton) shows very interesting behaviors in its pulse shape and phase. There is a good review article, "Self-similarity in ultrafast nonlinear optics, Nature physics (2007)" given by John M. Dudley, Guy Millot and their team. Here we briefly discuss important properties of the parabolic pulse to make a wave-breaking-free high power ultrashort pulse for our use. When Eq. (4.34) is considered, in asymptotic case ($|T| \le T_p(z)$), the parabolic pulse has the analytic amplitude form as

$$A(z,T) = A_0 \exp\left(\frac{g}{3} z\right) \sqrt{1 - \frac{T^2}{T_p^2(z)}}, \tag{4.36}$$

and its phase has a form of

$$\varphi(z,T) = \varphi_0 + \frac{3\gamma A_0^2}{2g} \exp\left(\frac{2}{3} gz\right) - \frac{g}{6\beta_2} T^2, \tag{4.37}$$

where $T_p(z)$ and A_0 are the characteristic parabolic pulse width and amplitude respectively defined as

$$A_0 = \frac{1}{2}\left(\frac{gU_{in}}{\sqrt{\gamma\beta_2/2}}\right)^{1/3} \text{ and } T_p(z) = \frac{6\sqrt{\gamma\beta_2/2}}{g} A_0 \exp\left(\frac{g}{3} z\right), \tag{4.38}$$

The equations came from Ref. [108]. The equations show that the temporal intensity (A^2) and phase are parabolic functions. For our case A_0 = 7.3 and $T_p(z)$ = 100 ps at the given conditions where U_{in} ~ 10.0 pJ, γ ~ 4.0 $W^{-1}km^{-1}$, β_2 ~ 2.0 × 10^{-5} fs^2/nm, z = 10.5 m, and g = 2.0 m^{-1}. Hence, the actual pulse width (T) after EDF of 10.5 m was ~7 ps. Therefore we are in the asymptotic condition.

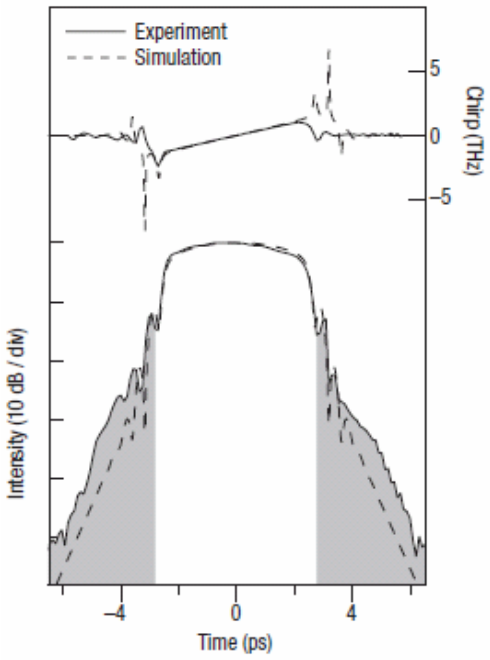

Figure 4.10 A parabolic pulse in the time domain. It has a parabolic pulse shape and a linear frequency chirp (or parabolic phase) in the core region. Reproduced from Ref. [108].

4.2.2.2 Experiment

The parabolic pulse was realized in our experiment. The set-up for the parabolic pulse generation is illustrated in Figure 4.11. A fiber ring laser (repetition frequency of 82 MHz) that has an average power of 1 mW (pulse energy: 12 pJ) and its spectral bandwidth of 20 nm (FWHM) was used as a seed for the parabolic pulse amplification. The pulse was then injected into about 10.5 m of Er^{3+} doped fibers (EDF) composed of 4.7 m of Liekki Er30 and 5.8 m of Nufern EDFL. An inline dual stage isolator was used to avoid the possible reflection from the interface between the fiber laser oscillator and the amplifier. Both EDFs are relatively low doped fibers and they have the positive dispersions ($\beta_2 > 0$). For example, the Er30 has the peak absorption of a 30 dB/m. The reason for employing the low doped EDFs is to avoid the pump power depletion and re-absorption possibly happened by the strong absorption of gain fibers, which is not desirable because the pump power should be fairly uniform through the entire length of EDF. When we were using the higher doped EDF such as Liekki Er110 possessing peak absorption of a 110 dB/m, the pumping power was rapidly depleted along the EDF and therefore the signal spectrum was significantly distorted at the end of the amplifier. The bi-directional pumping was employed to make the fairly constant gain through the entire gain fiber

and the control of pump power was critical for pulse shaping. When the pumping power for EDFs was the forward pump power of 350 mW and the backward pump power of 800 mW with 1480 nm diode lasers, a quasi-parabolic pulse was generated at the given length of the EDFs.

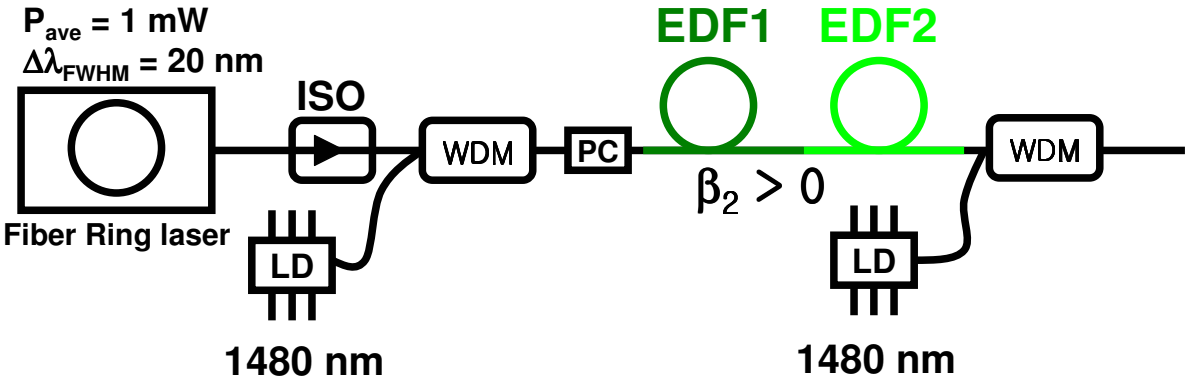

Figure 4.11 A parabolic pulse Er^{3+} doped fiber amplifier. WDM: wavelength division multiplexer, ISO: optical isolator, PC: inline polarization controller, LD: laser diode. The fiber ring laser (repetition frequency of 82 MHz) possessing an average power of 1 mW and a spectral bandwidth (FWHM) of 20 nm was used as a seed. Total 10.5 m of low doped EDFs were used to obtain enough positive dispersion and to prevent pump power depletion along EDFs. Bidirectional pumping of 350 mW to the forward direction and 800 mW to the backward direction with 1480 nm diode lasers was applied to the amplifier system [142].

Figure 4.12 (a) shows the measured intensity autocorrelation (AC) after the EDFA and the AC was fit to a parabola. In the core region, the pulse looks like a parabola but the pulse carries exponentially decaying tails at both sides, which is because the second order AC ($AC(\tau) = \int_{-\infty}^{\infty} I(t)I(t-\tau)dt$) of a parabolic pulse has higher order polynomials. For example, the second order AC integral of $I(t)$=1-x^2 is $1-\frac{5}{4}y^2+\frac{5}{8}|y|^3-\frac{1}{32}|y|^5$, where x=t/$T$ and y=τ/T [110]. Furthermore, by looking at the spectrum, we will see more information. Figure 4.12 (b) shows the spectrum of the generated pulse in our experiment. The spectrum was asymmetric and this is because 1) Re-absorption by the long length of EDFs (EDF we used has a strong absorption around 1530 nm, See Figure 2.3), 2) the frequency-dependent gain, and 3) the gain narrowing effect. From Eq. (4.22) and integrated gain of 26 dB, the spectrum possibly becomes narrow approximately by 36 % of the full spectral gain bandwidth. Even if the EDFA works at the unsaturated regime, the re-absorption and the gain distribution could shape the pulse and affect

the parabolic pulse generation by creating tails on the pulse edges. Note also that we were not able to measure the amplified pulse right after the EDF because we used a wavelength division multiplex (WDM) possessing a SMF-28 for the backward pumping. The structures on top of spectrum in Figure 4.12 (b) might originate from GVD effect which modifies the spectrum with SPM.

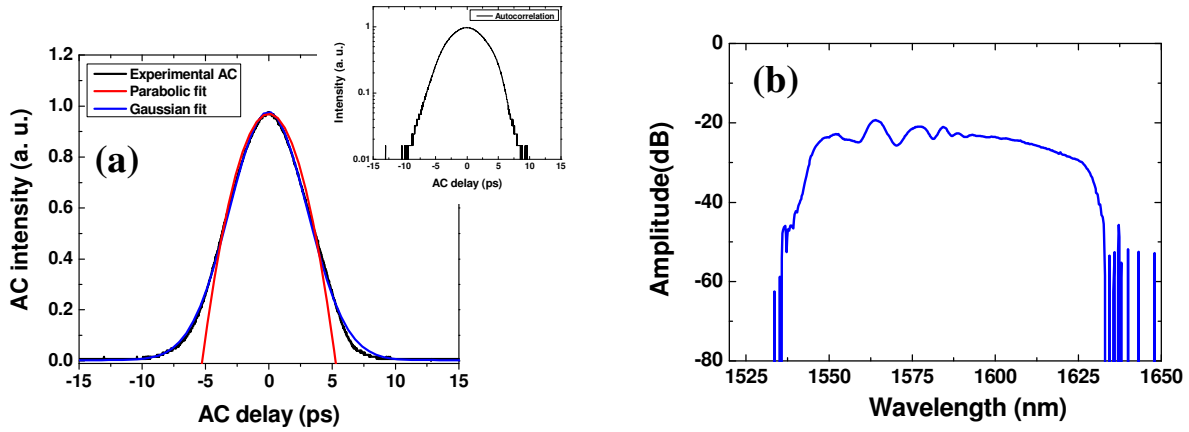

Figure 4.12 The quasi-parabolic pulse spectrum generated from the parabolic pulse EDFA with EDF length of 10.5 m. (a) The measured autocorrelation. The pulse was substantially broadened (~ 7 ps). The significant oscillatory feature was not found at the pulse edges caused by the optical wave-breaking. Inset shows the log scale of the experimental AC. (b) The spectral bandwidth of ~40 nm at FWHM. The pulse was measured right before pulse compression. The spectrum did not show the pedestal structure showing the optical wave-breaking. The experimental spectrum was fit to the parabola function. The spectrum was asymmetric possibly due to 1) Re-absorption by a long length of EDF, and 2) the frequency dependent gain, and 3) the gain narrowing effect.

The generated spectrum did not show the significant side-lobes and the AC showed negligible oscillatory features at the pulse edges caused by the optical wave-breaking.

4.2.3 Dispersion compensation of ultrashort pulses

The pulse compensation is an important technique for obtaining a high intensity peak pulse. Basically, the material that has an offset GVD sign can be used for the compression. Higher order dispersions sometimes need to be considered for the pulse possessing a broad spectral bandwidth during the ultrashort pulse compression. In this section, we will discuss two

different types of pulse compensation techniques which are the solitonic pulse compression using the Corning SMF-28e and the linear pulse compression using a hollow core photonic bandgap fiber (HC-PBGF (5-25)).

4.2.3.1 Solitonic pulse compression

The chirped pulse from the EDFA can be compensated using the Corning SMF-28e in order to obtain high peak intensity. We have already shown this in the simulation in the section 4.2.1.4. For the decent pulse energy and peak power, this method works fairly well. However, for the high power amplifier, Strong nonlinear effects degrade the ultrashort pulse quality (for example, a pedestal in the pulse decreases its pulse peak power) and sometimes the ultrashort pulse can be broken. Another interesting feature is the fluctuation in the compressed pulse duration and this is because the compressed pulse is not the fundamental soliton any more rather than the higher order solitons (Eq. 2.20). The higher order solitons are breathing in the pulse duration. This phenomenon is observed during the pulse compensation as shown in Figure 4.13.

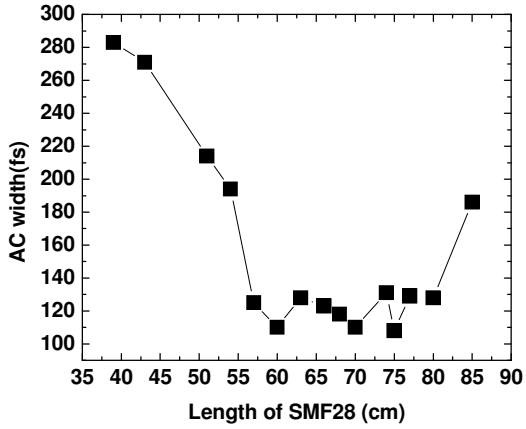

Figure 4.13 Soliton pulse compression using a Corning SMF-28e. Since the compressed pulse is the higher soliton, the pulse duration is oscillating along the fiber.

4.2.3.2 Linear pulse compression

The solitonic pulse compression with the Corning SMF-28e has degradation in the ultrashort pulse due to the nonlinear effect from the fiber and therefore it is not desirable for the high power pulse compression. The other method is the linear pulse compression which can avoid the pulse degradation from the nonlinear effect. The grating pair or prism pair is widely

used in a free space application but we, instead, used the HC-PBGF. Since the ultrashort pulse propagates through an air in the core of the HC-PBGF, the nonlinear effect is avoided.

4.2.3.3 Photonic crystal fiber

This photonic crystal fiber [111-114] has the two dimensional periodic array of holes and its structure creates the Bragg scattering, which allows that only certain wavelengths or energy band can be propagated through the fiber. Especially, the PCF has the versatility in propagating wavelengths by changing their geometrical structures, which makes the PCF more attractive for applications.

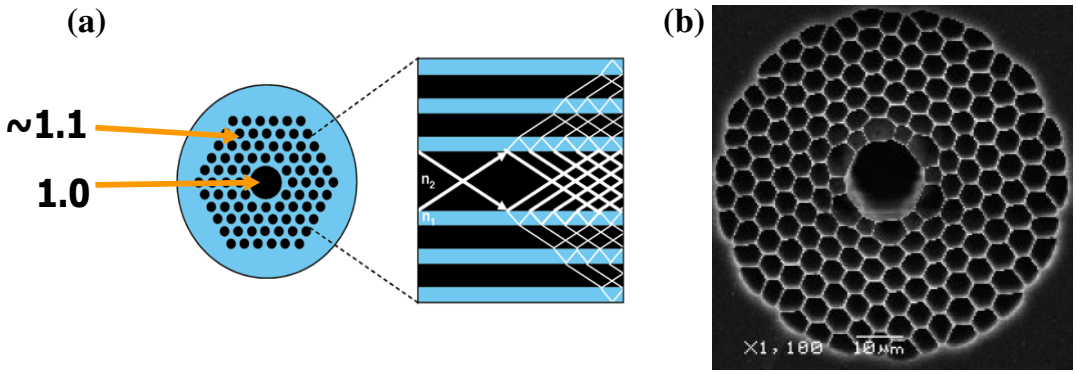

Figure 4.14 (a) A photonic crystal fiber: The two dimensional periodic array of holes creates the Bragg scattering which allows for propagating only certain wavelength regimes or energy bands. (b) Hollow core photonic bandgap fiber (HC-PBGF) fabricated by University of Bath, UK. It has an air core and its core diameter is a 10 μm. Because a pulse propagates in the air core, the nonlinear effect is very small, and therefore the HC-PBGF can be used as a linear pulse compressor. The GVD of the HC-PBGF (5-25) is -2.55×10^{-5} fs^2/nm at 1550 nm.

4.2.3.4 Ultrashort pulse dispersion compensation using HC-PBGF

Due to the substantial amount of positive dispersion from the 10.5 m of EDFs in our parabolic pulse EDFA, the pulse after the EDFs was highly chirped and the AC duration of ~7 ps was measured. However, the high peak intensity is required to facilitate nonlinear effects for the supercontinuum generation and therefore the pulse has to be compressed. For the pulse compensation, it is required to have the offset GVD sign of a dispersion compensator such as grating pairs, chirped mirrors, prism pairs, or fibers. Since we wanted to make all-fiber amplifier,

we have used a fiber compensator. However, unlike other linear dispersion compensators, the standard single mode fiber has shown relatively high nonlinearities, so this can cause the breaking of a pulse when the pulse peak intensity is high enough. In other words, the accumulated nonlinear phase shift is large. This could be avoided when we used the HC-PBGF. The HC-PBGF (5-25) made by J. C. Knight group at University of Bath, UK has the GVD of -2.55 × 10^{-5} fs^2/nm at 1550 nm which is close to that of the Corning SMF-28e (-2.40 × 10^{-5} fs^2/nm) but it has very small nonlinearity because the pulse propagates through an air hole as shown in Figure 4.14. The spectrum before and after the HC-PBGF has not changed much and the compressed pulse using the HC-PBGF (5-25) of 2.9 m has ~130 fs (FWHM) as shown in Figure 4.15. The pulse peak power was 1.8 × 10^4 W. The compressed pulse did not show the periodic oscillation during the pulse compression at different lengths of HC-PBGF (5-25), which is found in the nonlinear pulse compression (or solitonic pulse compression) of high order solitons. However, note that the compressed pulse has a weak pedestal due to nonlinear effects from the Corning SMF-28 of 1.2 m in WDM for the backward pumping. This pedestal could be suppressed by decreasing pulse energy, for example, by either decreasing pumping power or by reducing the length of SMF-28 in WDM [142].

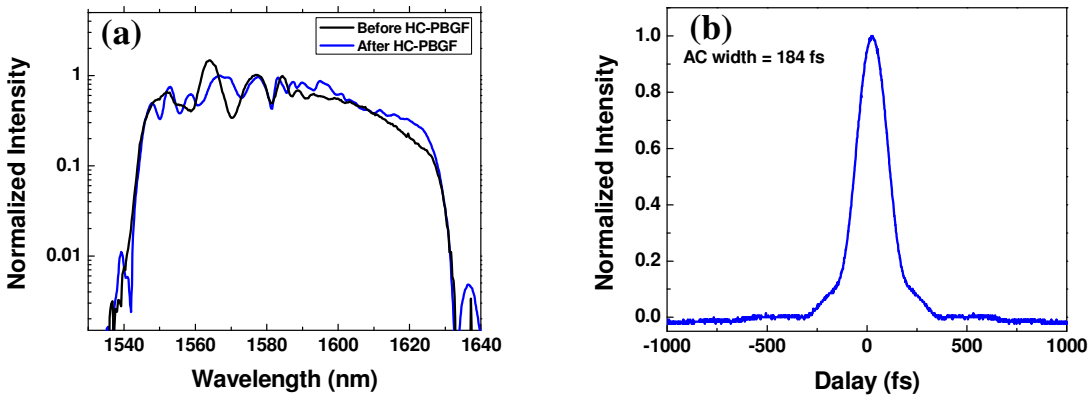

Figure 4.15 (a) The spectra before and after HC-PBGF (-5.25) length of 2.9 m. Due to the very low nonlinearity of HC-PBGF, the spectrum has not changed significantly. The final spectral bandwidth (40 nm FWHM) can support about 90 fs (FWHM) transform limited pulse. (b) Compressed pulse using a SMF-28 length of 1.2 m and HC-PBGF (5-25) length of 2.9 m. The pulse duration was ~ 130 fs and had a pedestal due to the nonlinear effects from SMF-28 in WDM for the backward pumping.

4.2.3.5 Third order dispersion in the pulse compression

Another interesting part in this pulse compression using the HC-PBGF (5-25) was the third order dispersion (TOD) or β_3. The spectral bandwidth of the parabolic pulse was ~40 nm at FWHM corresponding to the transform-limited (TL) pulse width of 90 fs but practically we could not achieve the TL pulse. Although we do not demonstrate it quantitatively, we think that this is due to relatively high TOD of HC-PBGF (5-25). The TOD can be calculated from D and the slope of D (D_{slope}) (See Appendix D). The equation is written as

$$\beta_3 = \frac{\lambda^4}{4\pi^2 c^2}\left(D_{slope} + \frac{2}{\lambda} D\right), \tag{4.39}$$

The HC-PBGF (5-25) has the quite large dispersion slope [57] compared to that of single mode fibers and therefore possibly creates the larger TOD. For example, the HC-PBGF (5-25) made by University of Bath and used for our pulse compensation has about two times larger TOD than that of the Corning SMF-28e at 1550 nm and its difference is increased when wavelengths is away from 1550 nm.

NOTE: Changing the seed source from a mode-locked fiber ring laser to a CNFL

After we demonstrated the parabolic pulse amplification with a mode-locked fiber ring laser in Figure 4.11, we changed the seed source from the fiber ring laser to the CNFL (OFS). The CNFL has the repetition frequency of 167 MHz, the average power of 1 mW, and the spectral bandwidth of 11 nm. Although the spectral bandwidth was the half of the previous fiber ring laser, the amplified spectral bandwidth was 40 nm at FWHM. Thereafter the pulse was compressed again with HC-PBGF (5-25) and we achieved the pulse width of ~125 fs at FWHM.

4.3 Supercontinuum generation for a self-referenced CEO frequency detection

4.3.1 Background for the supercontinuum generation

Supercontinuum is the coherent spectrum possessing more than an octave bandwidth. The origin of the supercontinuum is the strong degenerated four wave mixing, the fission of higher

order solitons, and th non-solitonic radiation [31, 115-117]. For Ti:Sapphire laser (center wavelength at 800 nm), micro-structured photonic crystal fibers are widely used, and for Er^{3+} doped fiber laser (center wavelength at 1550 nm), highly nonlinear fibers (HNLF) are employed. In our experiment, the supercontinuum was generated with HNLF, a type of Ge-doped silica fiber, and its dispersion was modified by exposing the fiber to ultraviolet (UV) [27]. This fiber was manufactured by OFS and showed the nonlinear coefficient of 10.2 $W^{-1}km^{-1}$, which is ten times larger than that of the Corning SMF-28e. Its zero-dispersion-wavelength is near 1550 nm as shown in Figure 4.16 and therefore the nonlinear effects are optimized for the pulse centered near 1550 nm [100]. In addition, this OFS HNFL allows for the direct splicing to the EDFA with relatively low loss which is less than 1.5 dB and the best splicing is 0.2 dB, (See Appendix F) which made the process for our supercontinuum generation simple and robust.

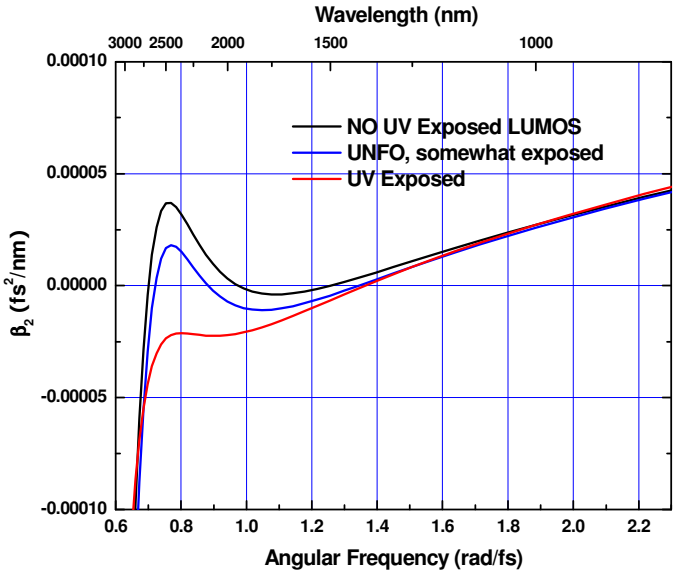

Figure 4.16 GVDs of three types of OFS HNLFs. Each GVD was calculated from dispersion parameters (*D*) provided from the company (OFS). The calculation has shown that the zero dispersion wavelength of the OFS HNLF we used is near 1550 nm.

4.3.2 Experiment for the supercontinuum generation using a parabolic pulse

In our parabolic pulse EDFA, we used HC-PBGF (5-25) for compensating dispersion to make an ultrashort pulse. Thereafter we tried to splice fiber from HC-PBGF (5-25) to OFS HNFL but the splicing loss is too high (>6 dB) to directly splice between two fibers. So we add a

short piece of Corning SMF-28e (~14 cm) as a bridge between HC-PBGF (5-25) and OFS HNLF in order to reduce the splicing loss. (The common loss between HC-PBGF (5-25) and Corning SMF-28e is 1.5 dB) Therefore the final average power before HNFL was 215 mW and its pulse duration was about 125 fs. The calculated peak intensity was 9.6×10^4 W and the corresponding pulse energy was ~1.3 nJ. Two inline fiber polarization controllers are used to optimize the supercontinuum spectrum for the *f* to 2*f* interferometer because the supercontinuum spectrum was very sensitive to those polarizations. In addition, the spectral bandwidth of the seed pulse was also important factor to obtain the desirable supercontinuum spectrum and this was realized by controlling the polarization of the CNFL cavity. The supercontinuum was generated from 1.0 μm to 2.2 μm with a 40 cm of OFS HNLF as shown in Figure 4.17. Thereafter Corning SMF-28e was spliced to OFS HNLF in order to compensate the delay between *f* and 2*f* components we wanted to beat against each other. The 10 cm of Corning SMF-28e was added and the length of fiber was determined by calculating the temporal delay between two frequencies in OFS HNLF. Finally, an average power of 170 mW was injected to a collinear *f* to 2*f* interferometer to detect CEO frequency.

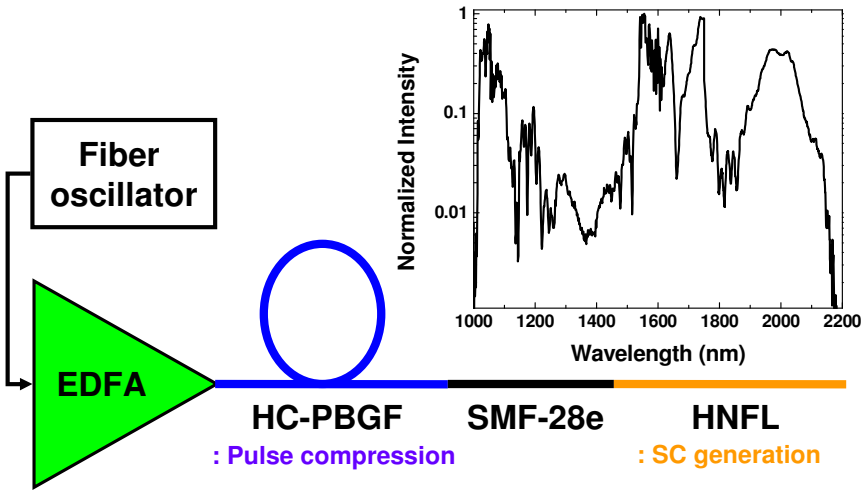

Figure 4.17 All-fiber supercontinuum generation. The supercontinuum was generated with the pulse from EDFA using the CNFL seed pulse. The supercontinuum spectrum was stretched from 1.0 μm to 2.2 μm. The OFS HNLF was spliced to the Corning SMF-28e using a fusion arc splicer (Ericson FSU995-FA). The Corning SMF-28e was used as a bridge fiber to reduce the splicing loss when the HC-PBGF (5- 25) is directly spliced to the OFS HNLF. All-fiber structure made the system simple and robust.

4.4 Summary

The ultrashort pulse from the Er^{3+} doped fiber laser oscillator has the small average power but the pulse amplification for high peak intensity pulses is demanded to generate the supercontinuum spectrum for detecting CEO frequency using the self-referenced f to $2f$ interferometric method. To understand the process of pulse amplification, the susceptibility and the related effects were explained and NLSE was introduced for simulating the ultrashort pulse propagation in an EDFA. The GVD and SPM were included to NLSE. We used both a solitonic EDFA and a parabolic pulse EDFA for the pulse amplification. The integrated power gain of parabolic pulse EDFA was 26 dB. The parabolic pulse is an asymptotic solution of NLSE in the positive dispersion gain fiber. The ideal parabolic pulse has only linear chirp and it is free from the optical wave-breaking. The highly chirped parabolic pulse after EDF was linearly compressed with the HC-PBGF (5-25) possessing very small nonlinearity. The compressed pulse has the pulse duration of 130 fs at FWHM and the peak power of 1.8×10^4 W. The pulse was injected to the OFS HNLF and the octave spanning supercontinuum spectrum was generated from 1.0 μm to 2.2 μm. In the following chapter, we will start with discussing the CEO frequency detection using the supercontinuum spectrum.

Chapter 5 - CNFL Comb Phase-stabilization and Noise Reduction

In order to phase stabilize a frequency comb, both the repetition frequency and the CEO frequency must be detected. The detection of the repetition frequency is simple and it can be detected using a fast photodetector from an output of the laser. However, the detection of the CEO frequency is cumbersome, and therefore more efforts are required. In our research, the self-referenced detection for the CEO frequency is implemented. For the purpose, the supercontinuum spectrum, a more than octave spanning spectrum stretched from 1.0 μm to 2.2 μm, was generated for detecting the CEO frequency in Chapter 4. In this chapter, we will discuss the detection of the CEO frequency and the design of an f to $2f$ collinear interferometer in the beginning. The low frequency part in supercontinuum spectrum is frequency-doubled using a nonlinear crystal. The control of the CEO frequency will be followed for the continuous discussion of its stabilization.

The stability and noise of the CNFL comb is also explored in this chapter. The low noise operation is very important for optical frequency metrology, which improves reliability of frequency measurements. It is even more critical when the comb is applied to multi-heterodyne dual comb spectroscopy [23] and optical frequency synthesis. From the comb equation, $\nu_n = n f_r + f_0$, n is the large number that is on the order of 10^6. Therefore a small change in the f_r caused by noise can be very large in each mode.

The quality of a frequency comb can be determined by how faithfully it is synchronized to the reference oscillator that can be either a microwave frequency standard or an optical frequency standard. For many applications, the linewidth and phase noise of the optical reference source have to be faithfully transferred to each comb tooth. Unfortunately, due to the noise in the frequency comb, the transfer and synchronization may not be perfect. Hence, the noise affects the linewidth and SNR of each comb tooth. The lineshape of comb teeth is an ideally delta function because the frequency comb is the interference of a train of infinite pulses but in practice the individual comb tooth has finite lienwidth because of all possible noise sources producing pulse timing-jitters. The timing-jitter degrades the inference and results in the finite linewidth. The other effect of noise is to add background noise, called the white phase noise, to

the frequency comb. The white phase noise degrades comb teeth's visibility when they beat against other frequency sources.

In this chapter, the comparison of the frequency comb produced by a CNFL to the comb produced by a figure eight laser (F8L) has been shown in order to explain noise of the CNFL comb compared to a previously exiting fiber laser comb. The noise in the laser oscillator mainly leads the broad linewidth of an individual comb tooth, and the comb linewidth was indirectly measured by looking at the CEO frequency beatnote in the RF domain.

The possible frequency noise can be suppressed by electronic feedback controls. Since the comb has two degrees of freedom ($\nu_n = n f_r + f_0$), the entire comb teeth can be stabilized by locking the repetition frequency and the CEO frequency. The quality of the comb lock can be quantified by measuring power spectral density (PSD) which also provides useful information about the existing noise sources in the comb. In order to extend the CNFL comb to the precision spectroscopy, we studied further reduction methods at the end of this chapter. The study has shown that white amplitude noise, produced from a pump laser diode combined with the laser's sensitivity to that pump fluctuation, is a major source of noise.

In this chapter, we will discuss three phase-stabilized Er^{3+} doped fiber laser frequency combs. We named them as F8L Comb, CNFL Comb 1, and CNFL Comb 2 respectively. The information for the three fiber combs are summarized in Table 5.1 and will be discussed through this chapter.

	F8L Comb	CNFL Comb 1	CNFL Comb 2
Repetition frequency (f_r)	56 MHz	167 MHz	167 MHz (± 500 kHz)
Mode-locker	NALM	SWCNT	SWCNT
Type of EDF for the laser oscillator	Liekki Er110 (80 cm)	OFS EDF (30 cm)	Liekki Er110 (40 cm)
Pump LD for the laser oscillator	FITEL (P_{max}: 300 mW)	LUCENT (P_{max}: 180 mW)	FITEL (P_{max}: 300 mW)
Cavity design	All fiber ring cavity	All fiber ring cavity	Ring cavity with a free space
SNR of CEO frequency	30-33 dB	28-30 dB	23-25 dB
Linewidth of CEO frequency (free-run)	200 kHz	650 kHz	850 kHz
Laser roll-off frequency (ν_{3dB})	5.3 kHz	32 kHz	16 kHz
Fixed points for the pump power	150 THz	512 THz	215 THz
Fixed points for the cavity length	3 THz	3 THz	1 THz
Active temperature control	Yes	No	Yes

Table 5.1 The summarized features of the three fiber combs. LD: Laser diode.

5.1 Self referenced *f* to 2*f* CEO frequency detection

In Chapter 4, we discussed the supercontinuum generation and the compensation of a delay between two colors. Now we change a topic into the detection of the CEO frequency (f_0). The *f* to 2*f* self-referenced method was employed to detect f_0. The schematic design of a collinear *f* to 2*f* interferometer is shown below.

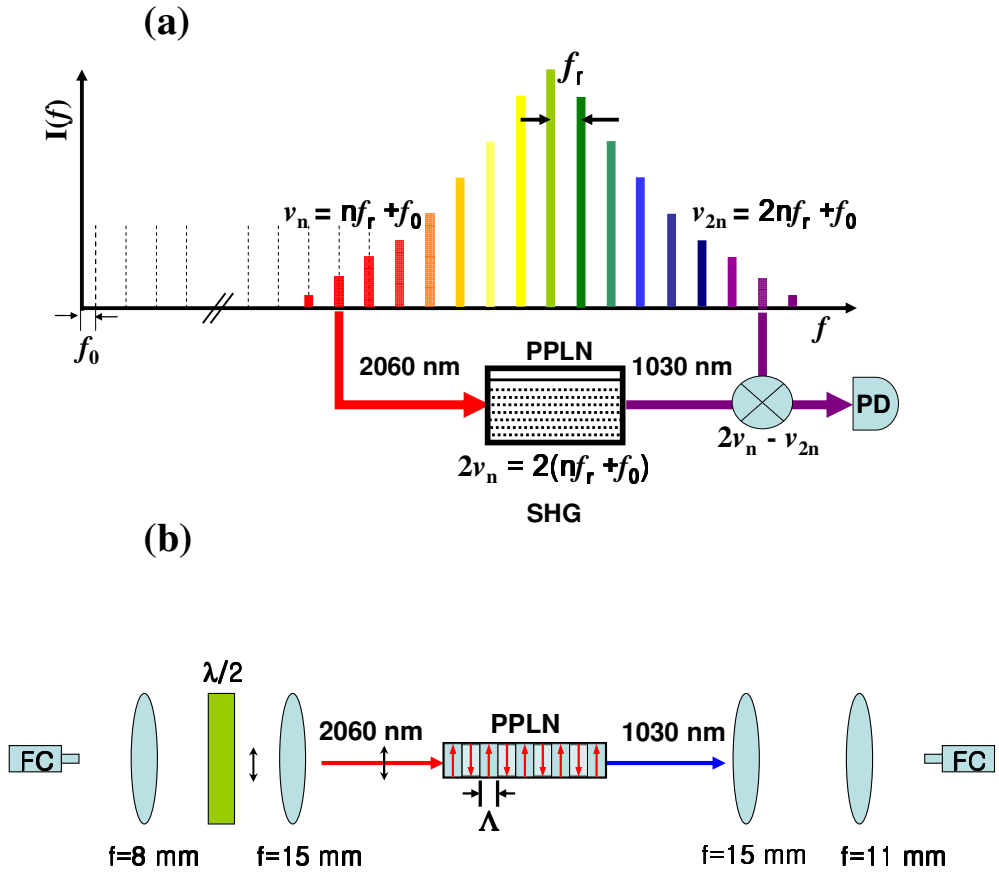

Figure 5.1 The schematic design of *f* to 2*f* interferometer. FC: fiber connector, λ/2: half waveplate, f: focal length, Λ: poling period, and PPLN: periodic poled lithium niobate. (a) The supercontinuum spectrum is injected into an *f* to 2*f* interferometer. The low frequency component (2060 nm) is frequency-doubled by a PPLN and is beaten against the high frequency component (1030 nm). The beatnote frequency, $2\nu_n - \nu_{2n} = 2(nf_r + f_0) - 2nf_r + f_0$, is the CEO frequency. The beatnote was detected using a fast photodetector (Newfocus 1811-FC). (b) The half waveplate was used to match the input polarization to the polarization of electric dipoles in the PPLN.

The f_0 is detected by beating the fundamental input (1030 nm) against the frequency-doubled output from 2060 nm. Mathematically,

$$2\nu_n - \nu_{2n} = 2(nf_r + f_0) - 2nf_r + f_0 = f_0. \quad (5.1)$$

5.1.1 Second harmonic generation with a periodically poled lithium niobate

In order to double a frequency at 2.0 μm, we used a periodic poled lithium niobate ($LiNbO_3$) crystal (PPLN) manufactured by Stratophase possessing multiple poling periods (Λ) from 29.5 to 32.5 μm increasing by 0.5 μm in a 10 mm long and a 10 mm wide. We used a quasi-phase-matching process using this PPLN and took some advantages from that. Generally, the fundamental input signal and the second harmonic signal oscillate, and exchange their energies through the propagation direction. When there is no phase matching between two signals in a crystal, the generated second harmonic photons mainly interfere destructively therefore its efficiency is low. However, when the fundamental input signal and the second harmonic signal have the constant phase relationship, the conversion efficiency can be maximized. In the tradition phase matching, the natural crystal birefringence is used to match the phase with the given crystal length so that the condition of $n(\omega)=n(2\omega)$ is satisfied in the crystal. The drawbacks of this method include that the number of available materials and the range of wavelengths that can be phase matched in those materials are limited. However, the quasi-phase-matching uses the combination of the periodicity of poles and the high effective nonlinearity of the crystal in a certain polarization. Instead of using the birefringence of crystals, the PPLN has periodically poled electric dipoles that change the direction of the diploes by 180^o in each poling period (Λ) so that it flips the sign of electric dipoles when the slope of conversion efficiency becomes negative. This process is called the quasi-phase-matching because the perfect phase-matching is not required.

5.1.2 Focusing of a Gaussian beam

The beam from a fiber diverges when it comes out of the fiber, so it should be collimated and be focused to the crystal to generate the SHG. Since the fundamental mode (LP_{01}) in a single

mode fiber is close to a Gaussian shape, we used the Gaussian beam approximation for the beam focusing. The equation we can use is that

$$w(z) = w_0\sqrt{1+\left(\frac{z}{z_R}\right)^2}, \tag{5.2}$$

where w_0 is the beam-waist at the origin and z_R is the Rayleigh range defined as

$$z_R \equiv \frac{\pi w_0^2}{\lambda}. \tag{5.3}$$

Eq. (5.2) explains the beam-waist expanded along the propagation direction and we can use this equation for focusing the beam. Since we knew the focal length of a lens and the initial beam-waist after the collimation, ~2 mm, we could calculate w_0 at the focal point. The chromatic aberration due to the broad spectral bandwidth was not considered but the equation gave a good approximation. In order to maximize the nonlinear interaction between the PPLN and the pulse, we changed the focal length and the beam-waist, and therefore we increased the effective nonlinear interaction length which is the Rayleigh range defined as Eq. (5.3). This means that when we focus the beam very tightly, we can increase the pulse intensity facilitating nonlinear effects but we loose the nonlinear interaction length through the crystal visa versa. So we compromised between the pulse intensity and the effective interaction length to maximize the efficiency of the nonlinear effect in the PPLN. The diameter of a lens can be chosen based on the π criterion ($D \doteq \pi w$) for transmitting ~99 % power and reducing diffraction.

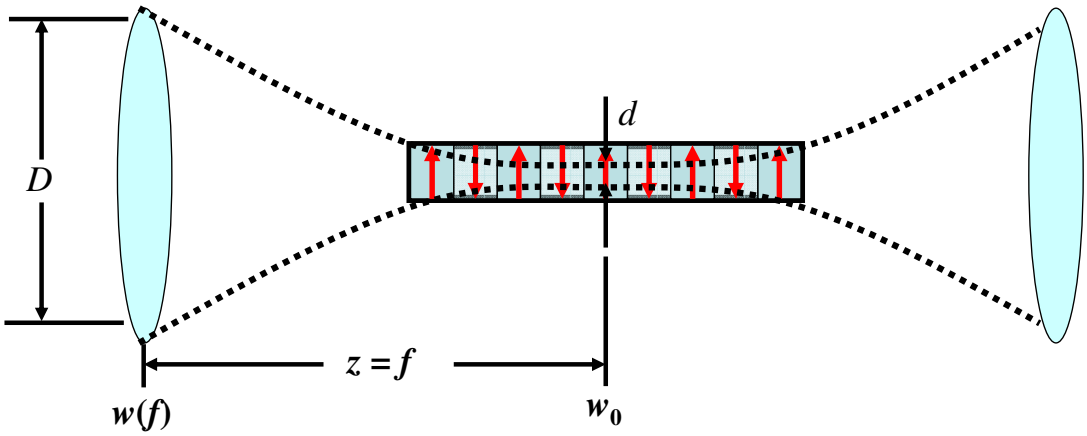

Figure 5.2 Gaussian beam focusing. *D*: Diameter of lens, *f*: focal length, w_0: beam-waist at the focal point. The collimated beam is focused and the beam-waist is minimized at the focal point which is the center of the PPNL crystal. The diameter of the lens can be chosen based on π criterion ($D = \pi w$) for transmitting ~99 % power and reducing diffraction.

The focal length of the lens we chose was 15 mm. This gave the beam-waist of 4.9 μm and the effective interaction length of 37 μm at λ = 2060 nm we wanted to generate the second harmonic output.

5.1.3 Second harmonic generation efficiency of the interferometer

The power transmission efficiency for a CW laser was more than 60 % when the diverging beam was collimated and re-coupled into a single mode fiber. We inserted the focusing lenses, a half waveplate, and a PPLN in between a pair of collimating lenses to generate the second harmonic output with 2060 nm light from supercontinuum spectrum. The half waveplate was used to match the input polarization to the polarization of electric diploes in the PPLN. The SHG efficiency of the interferometer was about 10 % which includes the SHG conversion efficiency of the PPLN and the beam coupling efficiency with a single mode fiber after the SHG.

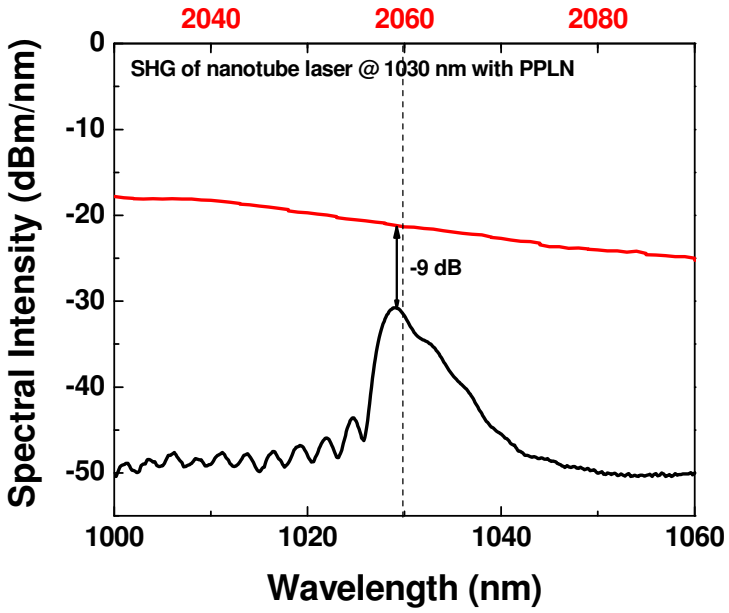

Figure 5.3 The SHG efficiency of our compact collinear *f* to 2*f* interferometer at 2060 nm. The power at 2060 nm was -21 dBm/nm in the supercontinuum spectrum before a *f* to 2*f* interferometer and the generated second harmonic signal had the power of -30 dBm/nm. The efficiency of the SHG in the interferometer was about 10 % which included the SHG conversion efficiency of the PPLN and the beam coupling efficiency with a single mode fiber after the SHG.

5.1.3.1 Poling period and temperature tuning

Practically, we choose the SHG frequency to maximize the beatnote frequency which is the CEO frequency. In that purpose, the SHG frequency can be tuned by changing the poling period or the temperature of the PPLN crystal. We use the program, SNLO, to determine those parameters. Generally, the PPNL works at the temperature range from 100°C to 200°C in order to prevent the PPLN from the damage caused by the photorefractive effect. For the parabolic pulse amplifier output, we used the poling period of 32.0 μm and the crystal temperature of 110°C. At the condition, the SHG at 1030 nm was maximized.

5.1.4 Detection of the CEO frequency

The optical beatnote is filtered using an optical interference filter and is detected in a fast photodetector. The detected f_0 is shown in Figure 5.4. Due to the sampling of an electronic

spectrum analyzer (Nyquist frequency at ~83.5 MHz), two RF beatnotes appear, one is at f_0 and the other is at $f_r - f_0$ on the electronic spectrum analyzer. The signal to noise ratio (SNR) is about 30 dB and the peak power was about -28 dBm with the resolution bandwidth (RBW) of 300 kHz.

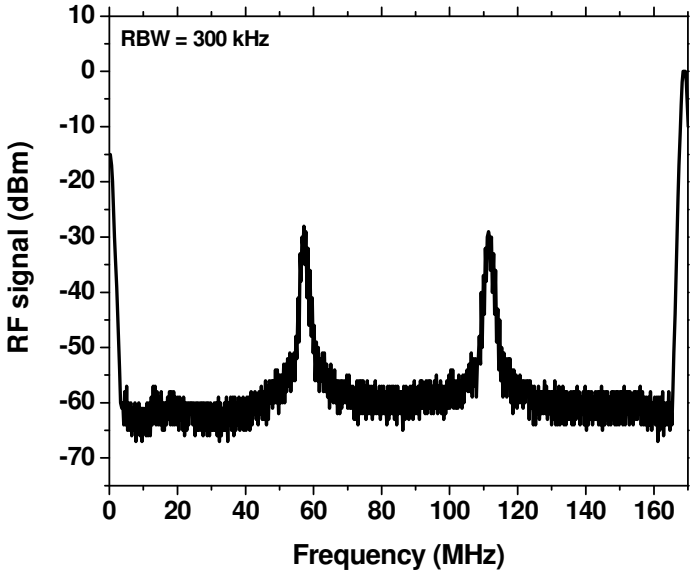

Figure 5.4 The RF beatnote (f_0) of the CNFL Comb 1. The Nyquist frequency at ~83.5 MHz. Due to the sampling of an electric spectrum analyzer (ESA), the two RF beatnotes appear, one is at f_0 and the other is at $f_r - f_0$ on the ESA.

5.1.4.1 Noise in the supercontinuum generation and the SNR of CEO frequency

During the supercontinuum generation process, white noise can be produced from shot noise and possibly Raman scattering [118]. The amount of noise is exponentially increased when the average power of an input pulse increases and therefore the shorter pulse is desirable in order to achieve a low noise supercontinuum generation because the shorter pulse can support high peak intensity at the less average power. Therefore the higher repetition frequency comb might have more white noise because more average power is required to produce the same peak intensity when other parameters are same. This supercontinuum noise increases background noise level and reduces possible SNR. Figure 5.5 shows that detected f_0s. For both cases, the generated supercontinuum is broad enough to detect f_0 but the input powers, the repetition frequencies, and the input pulse durations were different and they are summarized in Table 5.1. The CNFL Comb 1 has higher average power than that of the F8L Comb. Even if the peak RF

power of the CNFL Comb 1's f_0 was higher, the optical noise floor of the CNFL Comb 1 is higher than that of the F8L Comb by 10 dB. Interestingly enough, the linewidth of the CNFL Comb 1's f_0 is wider than that of the F8L Comb. We will discuss this in next sections.

	F8L Comb	CNFL Comb 1
Input pulse power	100 mW	215 mW
Repetition frequency	57 MHz	167 MHz
Input pulse duration	80 fs	125 fs

Table 5.2 Input pulse parameters for the two different pulsed lasers to generate supercontinuum spectra.

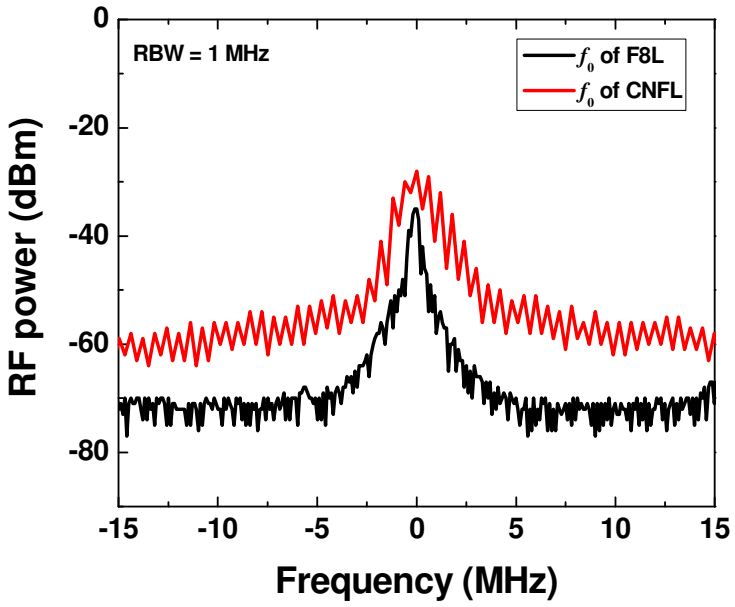

Figure 5.5 Detected CEO frequencies (f_0). The background noise level of the CNFL Comb 1's f_0 is higher than that of the F8L Comb's f_0 by 10 dB due to more supercontinuum noise.

5.2 Noise in the fiber comb

A variety of noise sources exist in the comb and affect the comb performance. To operate the comb in the low noise condition, the noise sources should be well understood and suppressed.

In Figure 5.6, the possible noise sources are shown. These noise sources are generally categorized into two groups [34, 119]. One group is the intra-cavity noise sources which impact the mode-locked laser oscillator itself. The other group is the extra-cavity noise sources which perturb the comb after the pulse is generated from the oscillator. The intra-cavity noise sources contain environmental perturbations such as fiber length fluctuation, pump induced relative intensity noise (RIN), intra-cavity amplified spontaneous emission (ASE), and cavity loss. The extra-cavity noise sources include environmental perturbation such as path length fluctuation, ASE from fiber amplifier, shot noise, and supercontinuum noise. These noise sources are fairly well understood and have different effects on the comb.

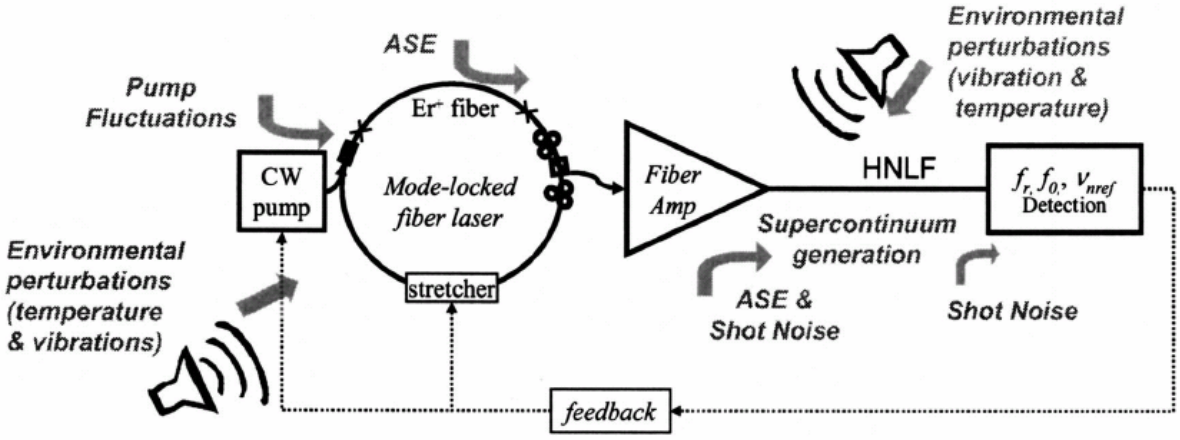

Figure 5.6 Schematic diagram of the fiber based optical frequency comb, which consists of fiber laser oscillator, EDFA, HNLF for supercontinuum generation, detection set-up of the repetition frequency and CEO frequency, and electronic feedback controls for locking the comb. The possible noise sources are shown in the diagram. Intra-cavity noise sources acting on the laser oscillator include environmental perturbations (temperature and mechanical vibrations), pump fluctuations, intra-cavity ASE and loss. Extra-cavity noise sources acting after the laser contain environmental perturbations, ASE from an EDFA, shot noise, and phase noise during the supercontinuum generation. Reproduced from Ref. [34].

The different noise sources have different impacts on the comb. The environmental noise sources such as mechanical and acoustic vibration and temperature fluctuation dominate the low Fourier frequency noise below 500 Hz. The pump fluctuations such as RIN are dominant in intermediate Fourier frequency which is the range from 0.5 kHz to 50 kHz. The quantum noise

sources such as ASE from 50 kHz to 500 kHz, shot noise and supercontinuum noise are responsible for the noise at even higher frequencies [34].

5.3 Amplitude modulation and response of the CNFL frequency comb

5.3.1 Measurement of Er^{3+} doped fiber comb frequency response

The Er^{3+} doped fiber comb has a characteristic laser frequency response for varying pump power due to the response of the gain medium [87]. The response has a roll-off frequency which acts like a low pass filter. The roll-off frequency is different for the different Er^{3+} doped fiber combs but typically has the value of 5 kHz to 15 kHz [87]. Therefore the contribution of high Fourier frequencies can be naturally suppressed in the Er^{3+} doped fiber laser comb. The roll-off frequency can be measured by an amplitude modulation (AM) of pump power of a laser diode as shown in Figure 5.7.

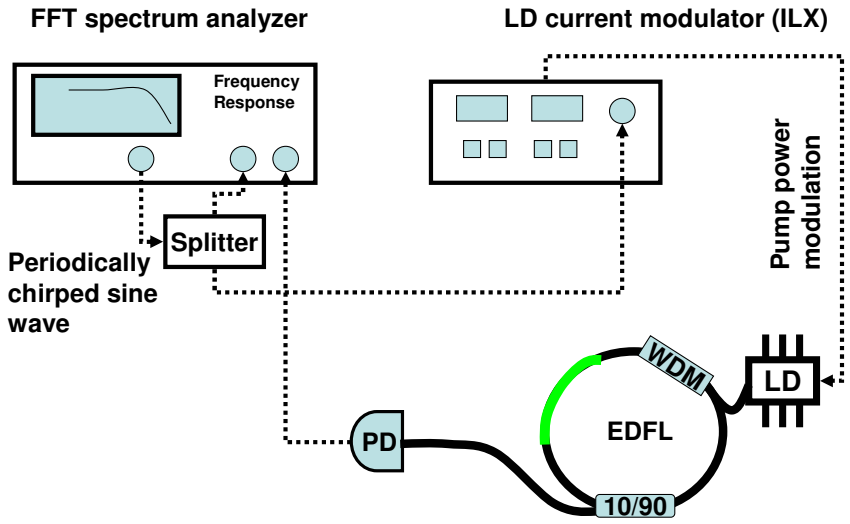

Figure 5.7 Set-up for an amplitude modulation (AM) of the pump power of a LD. WDM: wavelength division multiplexer, PD: fast photodetector, LD: Laser diode. Fast Fourier transform (FFT) spectrum analyzer generates a periodically chirped sinusoidal wave (1 Hz ~ 51.2 kHz) which is split into two ports. One works as a reference signal. The other goes to ILX box and modulates the current of the LD. The change in the magnitude and frequency of the sinusoidal wave modulates the power of the LD. The frequency response of an Er^{3+} doped fiber laser comb has a roll-off for the periodically varying input signal.

The fast Fourier transform (FFT) spectrum analyzer generates a periodically chirped sinusoidal wave from 1 Hz to 51.2 kHz. The sinusoidal wave is split into two parts. One is used as a reference for the frequency response measurement. The other goes into the laser current modulator in order to modulate the pump power with a periodically chirped manner. The comparison of two signals shows a roll-off frequency response as shown in Figure 5.8. The roll-off frequency (ν_{3dB}) of the Er^{3+} doped fiber comb has shown a close relationship with the relaxation time of the Er^{3+} gain medium [87] whose relaxation time is on the order of millisecond (ms).

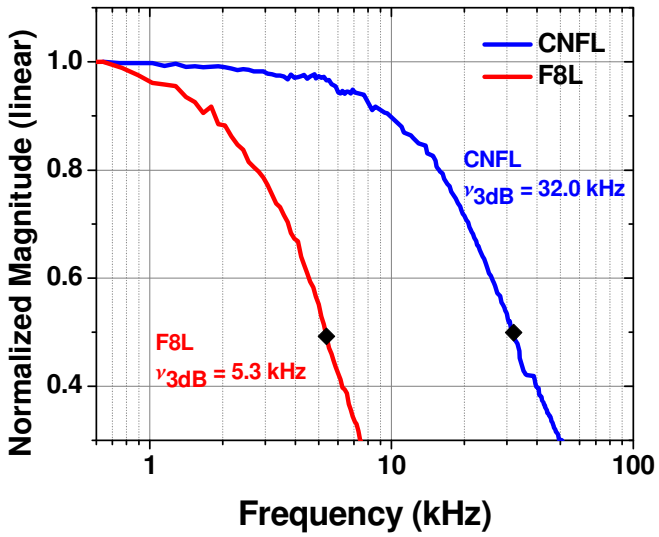

Figure 5.8 The roll-off frequencies (ν_{3dB}) of two fiber combs; F8L Comb (red) and CNFL Comb 1 (blue). The CNFL Comb 1 shows the higher ν_{3dB}. The F8L Comb was rolled off at 5.3 kHz but the CNFL Comb 1 was rolled off at 32 kHz. The higher roll-off frequency implies possibly more pump noise contribution to the comb dynamics. Reproduced from Ref. [68]

The frequency responses of two Er^{3+} doped fiber laser combs were measured. The F8L Comb has ν_{3dB} at 5.3 kHz and the CNFL Comb 1 shows ν_{3dB} at 32.0 kHz. It is not clearly known what determines the difference in ν_{3dB}. However, the higher roll-off frequency implies that the laser is more susceptible to high frequency noise sources such as particularly the pump RIN laid on 0.5 kHz to 50 kHz.

5.3.2 CEO frequency linewidth of the CNFL comb

In the section 5.2, we explained that the linewidth of a comb is governed by intra-cavity noise sources. Particularly, the noise of a pump source laid on 0.5 kHz to 50 kHz is responsible for the relatively broad linewidth of fiber laser combs [34, 120, 121]. Since we do not have a very stable and narrow linewidth laser source, both f_0 linewidths (a relative linewidth of two comb teeth) were measured when the combs were free-run in order to check the contribution of the pump RIN. The CNFL Comb 1 has the wider f_0 linewidth as shown in Figure 5.9. The measured f_0 linewidth of the CNFL Comb 1 was 650 kHz at FWHM and that of the F8L comb was 200 kHz at full width half maximum (FWHM) with the Lorentzian fit respectively.

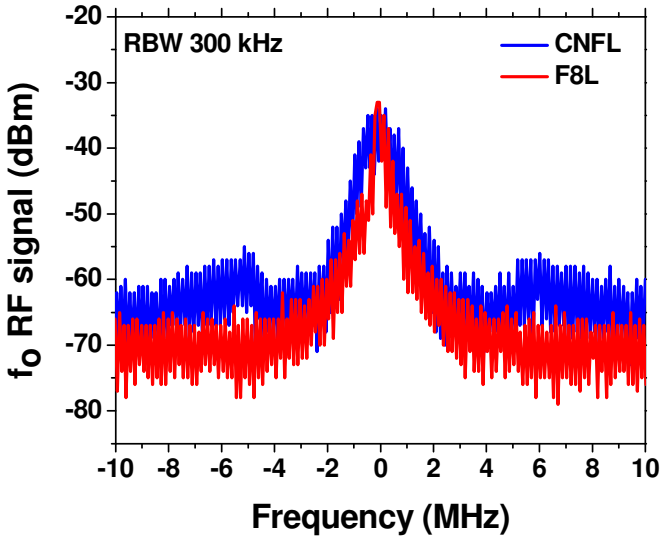

Figure 5.9 The free-running f_0 linewidths of two different combs; F8L comb in red and CNFL Comb 1 in blue. The wider f_0 linewidth was corresponding to the higher ν_{3dB}, and therefore the f_0 of the CNFL Comb 1 has wider f_0 linewidth and larger accumulatd phase noise.

The relatively large ν_{3dB} led to broad f_0 linewidth as we predicted. The high Fourier frequency noise components appeared with the wings of measured f_0 in the RF domain and therefore it was possible to achieve significant reduction in f_0 linewidth when the high Fourier frequency noise such as pump RIN was suppressed in Ref. [120, 121]. The similar result was obtained in our experiment and the reduction of noise in the CNFL Comb 1 will be discussed in the following sections.

5.4 Elastic tape model and the fixed point

In the time domain, the noise is understood as sources of the pulse timing-jitter. On the other hand, it can be explained as the motion of the comb teeth in the frequency domain. The later gives more useful and intuitive picture about the noise sources because the measured Fourier frequency response provides an insight for possible noise sources. The comb teeth are defined by a simple algebraic equation,

$$\nu_n = n f_r + f_{0,} \tag{5.4}$$

Therefore the comb dynamics is governed by only two degrees of freedom which are the repetition frequency (f_r) and CEO offset frequency (f_0). Two parameters have different effects on the comb motion. The fluctuation on f_r induces a breathing-like motion about a single fixed point (we will discuss in this section), and the perturbation on f_0 gives rise to a translational motion so that the whole comb teeth are shifted by the change of f_0. In general, the comb dynamics will be a coupled motion of both degrees of freedom but the comb motion in practice can be a linear combination of the motions of f_r and f_0.

One can think that the motion of frequency comb might be random but interestingly enough the motion of comb teeth has a pattern [49, 122] where the comb teeth are breathing like an accordion about a single fixed point. The fixed point will be different depending on noise sources and characterizes the specific noise on the comb.

5.4.1 Mathematical description of the fixed point

The fixed point can be mathematically defined. First, we can consider a perturbation, δX, to a parameter (X) related to the fiber laser comb. The X can be a pump power or a cavity length but can be all possibly changeable parameters in the fiber laser comb such as cavity loss or dispersion. This perturbation will change the CEO frequency (f_0) and the repetition frequency by an amount of

$$\delta f_0 = \frac{df_0}{dX}\delta X$$
$$\delta f_r = \frac{df_r}{dX}\delta X, \tag{5.5}$$

respectively and then small change in the n^{th} comb mode frequency, $\delta\nu_n$, will be $\delta\nu_n = n\delta f_r + \delta f_0$ from Eq. (5.4). This change in the comb mode vanishes when

$$n = n_{fix}^{X} = -\frac{\frac{df_0}{dX}}{\frac{df_r}{dX}}. \tag{5.6}$$

Therefore the fixed point frequency (or just fixed point) is

$$\nu_{fix}^{X} \equiv n_{fix}^{X} f_r + f_0, \tag{5.7}$$

where the theoretical value of f_0 is defined as

$$f_0 = \nu_c\left(1 - \frac{v_g}{v_p}\right), \tag{5.8}$$

where ν_c is the carrier frequency, v_g is the average group velocity and the v_p is the average phase velocity of the cavity. For fiber lasers, this has the value of f_0 ~1-3 THz that is not experimentally achievable. Practically we measured a harmonic frequency of theoretically achievable CEO frequency in the RF domain.

Even if we can find fixed points of all possible noise sources, we will consider two parameters that are implemented in our frequency comb control. One parameter is the pump power. The fixed point for the pump power can be derived from Eq. (5.6) and Eq. (5.7) by replacing X with the pump power. The other parameter is the cavity length. The fixed point for the cavity length change can also be measured with the same manner. For the different

perturbation parameters, the fixed points are different and bring about different amounts of breathing of the comb modes. The fixed point is not necessarily to be within the comb spectrum but it can be out of the comb spectrum. For example, the CNFL Comb 1 made has fixed points for the pump power change at ν_{fix}^{pump} = 512 THz and for the cavity length change at ν_{fix}^{length} =3 THz respectively. The CNFL Comb 2 which has a variable repetition frequency comb made for multi-heterodyne dual combs spectroscopy (See Chapter 7) has shown that ν_{fix}^{pump} = 215 THz and ν_{fix}^{length} = 1 THz respectively. In our combs, the two control parameters are independent or orthogonal because the fixed points for the pump power and the cavity length are well separated.

The CEO frequency has shown a higher sensitivity to the pump fluctuation rather than the cavity length fluctuation. In fact, this is the reason we can use the changes in the pump power to control the CEO frequency. The magnitude of the breathing motion of each comb tooth varies with respect to the fixed point for the pump power. When the comb teeth are far from the fixed point, the magnitude of breathing becomes larger as shown in Figure 5.10. The magnitude can be typically quantified by power spectral density (PSD, See appendix E). Simply saying, the PSD shows the magnitude of spurious signals caused by noise in the Fourier frequency domain.

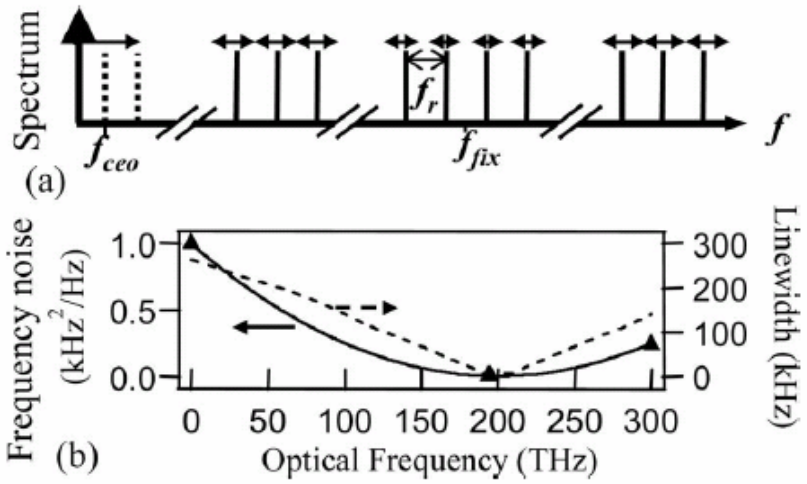

Figure 5.10 (a) Breathing modes of the frequency comb about the fixed point induced by pump power fluctuations; the length of the double arrow indicates the magnitude of the frequency jitter. (b) Frequency noise level (solid line, left axis), and the linewidth (dashed line, right axis), versus optical frequency. The assuming fixed point is at 200 THz. Reproduced from Ref. [120].

In general, the magnitude of breathing motion for the n^{th} mode of fiber combs is related to the equation written with the language of the PSD [120].

$$S_n(\nu) = (n - n_{fix})^2 \left(\frac{P \mathrm{d}f_r}{\mathrm{d}P} \right)^2 \left[\frac{RIN_p}{1 + (\nu / \nu_{3dB})^2} \right] \left[\frac{\mathrm{Hz}^2}{\mathrm{Hz}} \right], \tag{5.9}$$

where P is the pump power, RIN_p is the relative intensity noise of a pump laser, and $\nu_{3\mathrm{dB}}$ is the laser roll-off frequency we discussed in the earlier section. Note that the magnitude of the PSD, $S_n(\nu)$, increases with the second order polynomial from the fixed point and it is illustrated in Figure 5.10 (b). The $S_n(\nu)$ is also proportional to the RIN_p and the low $\nu_{3\mathrm{dB}}$ shows less noise. Furthermore, the noise would be low when the change in the repetition frequency is less sensitive to the pump power fluctuation. Therefore we can find solutions to reduce the noise in the comb mode by analyzing Eq. (5.9). First, the noise can be reduced by suppressing the RIN_p. The other method is to increase the feedback bandwidth for the pump power well beyond $\nu_{3\mathrm{dB}}$. These two approaches will be discussed in Section 5.7 before we will show the results. Here, we will first talk about how to measure the fixed points in the experiment.

5.4.2 Fixed point measurement

The experimental set-ups for the fixed point measurements are described in Figure 5.11. The fixed point is measured by modulating the control device such as a pump laser and a PZT (piezo-electric transducer) with the known modulation frequency (f_{mod}) and the magnitude using a signal generator (DS345: Stanford Research Systems). We used a square waveform with the f_{mod} of 0.5 or 1 Hz and applied the different amplitude of a modulating signal depending on the sensitivity of control devices as shown in Figure 5.6. For instance, the ILX laser diode current controller has the output current to the input voltage of 100 mA/V and the PZT voltage driver (Thorlab) has the output voltage to the input voltage of 15V/V. Both f_{r} and f_0 are then periodically modulated with the square wave and those signals can be counted using a frequency counter (Agilent 53132A). Thereafter the $\mathrm{d}f_{\mathrm{r}}/\mathrm{d}X$ and $\mathrm{d}f_0/\mathrm{d}X$ (X: pump power or cavity length) can be found and the fixed points are computed using Eq. (5.6) and (5.7). The variation in f_0 was much sensitive to the change of the pump power and it had an order of MHz unlike f_{r} whose change was on the order of Hz. The change of a few mW in the pump power was enough to see

the huge drift and modulation on f_0. This is because the change in the n^{th} mode in optical frequencies is multiplied by an order of ~10^6. The Lucent 980 nm (Maximum power of 180 mW) laser diode for the CNFL Comb 1 has the ratio of the applied current to the output power, 0.546 mW/mA and the FITEL 980 nm (Maximum power of 300 mW) laser diode for the CNFL Comb 2 has the ratio of 0.588 mW/mA respectively.

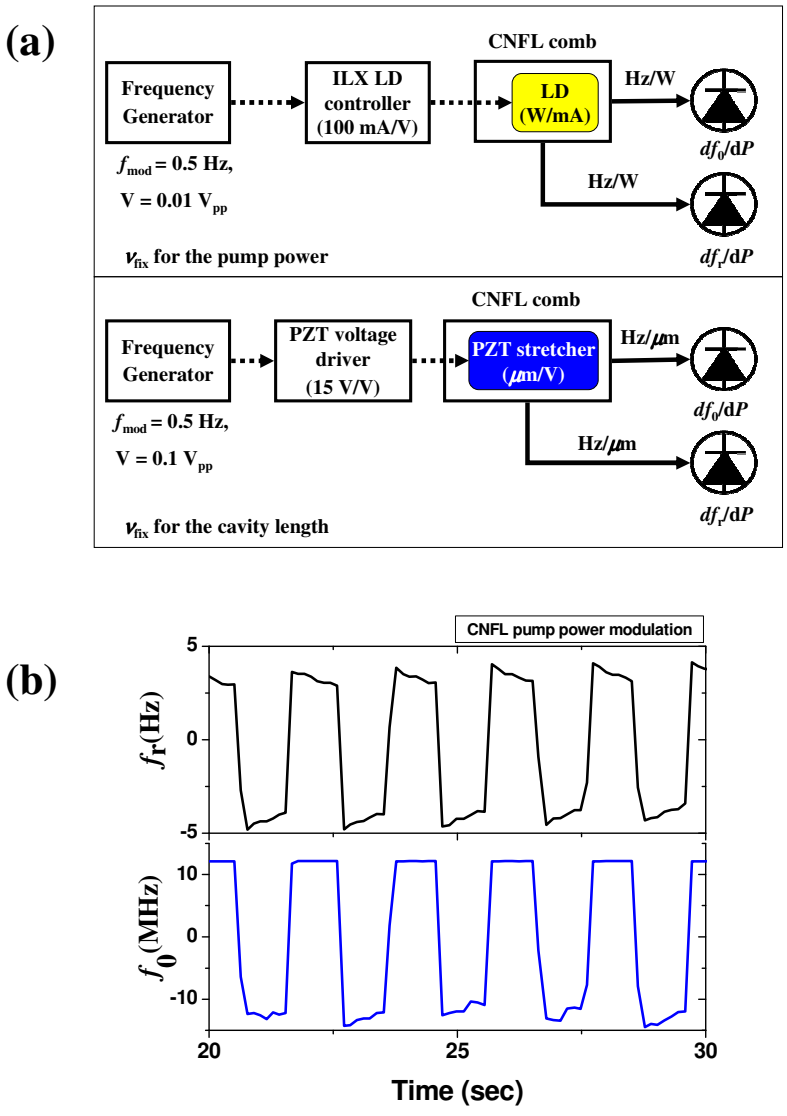

Figure 5.11 (a) Experimental set-up for the fixed point measurement for changes in the pump power and cavity length. A square wave (f_{mod}=0.5 Hz) is used to modulate both control devices and the amplitude is adjusted depending on the sensitivity of control devices. (b) The counted signals for the pump power modulation. The fixed point can be calculated from the modulated signals.

5.5 Feedback electronics and servo controls

Once both f_r and f_0 are detected, the frequency comb can be stabilized using electronic feedback controls (PI controls). The feedback loops are illustrated in Figure 5.12.

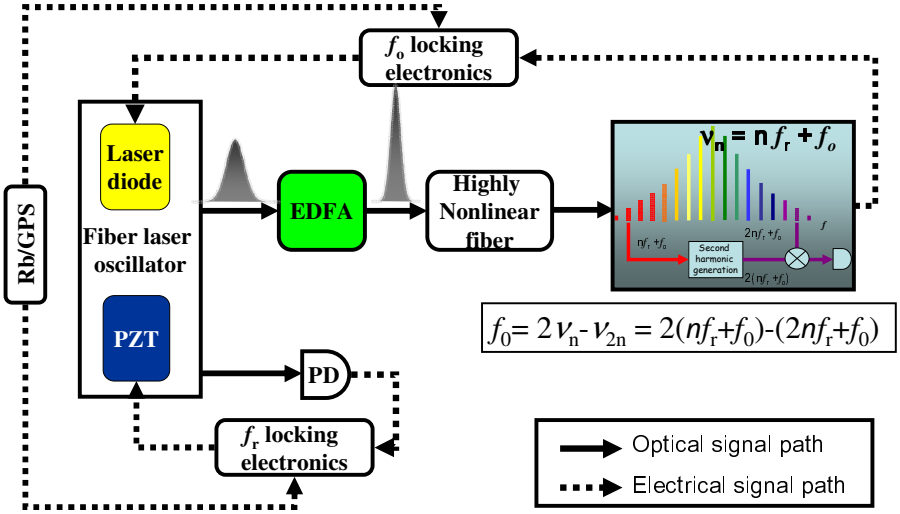

Figure 5.12 Phase-locking electronics for both f_r and f_0. The repetition frequency is detected using a fast photodetector from the oscillator output. The control of f_r was done by controlling the fiber length using a PZT fiber stretch (General photonics) in the cavity. The f_0 was detected using a self-referenced f to $2f$ interferometer. The stabilization of f_0 was obtained using the pump power control of the laser oscillator.

The detection of f_r is fairly simply and a fast photo-detector is used to detect the f_r signal from an output of the laser oscillator and the control of f_r was achieved by controlling the cavity length using a PZT fiber stretcher in the cavity. Changes in the cavity length (or fiber length) are a quite slow process mostly dominated by temperature. The fused silica fiber has an effective coefficient of thermal expansion of ~10^{-5}/^{o}K. Therefore, a good thermal isolation of the laser cavity and the cavity length control with a mechanical feedback provide a tight lock. The CNFL Comb 1 in a Styrofoam box has shown the temperature change of 0.3 ^{o}K for an overnight monitoring which corresponded to the change in the fiber length of 1.7 μm and therefore the dynamic range of our PZT fiber stretcher (General Photonics), at 3 μm, was enough to control the variation. On the other hand, the detection of f_0 is not straight forward like the detection of f_r. The f to $2f$ self-referenced interferometer is generally used to detect f_0 and we discussed it earlier in Chapter 4. The lock of f_0 was obtained by controlling the pump power for the laser oscillator.

The feedback loop for the lock is illustrated in Figure 5.13. All RF frequency devices were disciplined by a *GPS*[*]-steered Rb clock (Precision test systems, model: GPS10Rb) which guaranteed the short and long term stabilities in our frequency measurement.

* **Note:** The *GPS* shows the fractional instability of 7×10^{-13} at 1000 s averaging time. However, the stabilization becomes much more difficult as the accuracy increases. Therefore the short term instability must be improved.

5.5.1 CEO frequency lock electronics

The f_0 locking electronics is composed of a phase detector and a servo box (LB1005) with reference oscillators. The servo box includes a gain filter and an integrator and therefore the control voltage is generated from the servo box. This control voltage is fed into the laser oscillator and changes the CEO frequency. The CEO frequency is mixed with a 1 GHz local oscillator and divided down with a frequency divider. After the frequency divider, the mixed f_0 signal changes into a digital signal. The digitized signal is compared to f_{ref} which is the frequency we stabilize the CEO frequency to. We will discuss this feedback loop in detail in following sections.

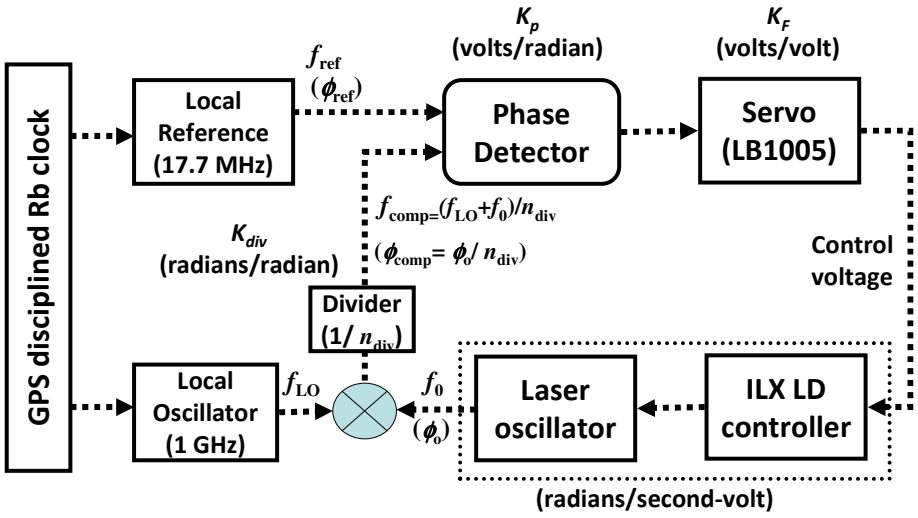

Figure 5.13 The Scheme of f_0 locking electronics. The phase detector compares the frequency (or phase), f_{comp} which is $(f_{LO}+ f_0)/n_{div}$ with the reference frequency (f_{ref}). The difference in frequency or phase is converted into voltage signal and it goes into a servo box (LB1005). The servo-box consists of a filter and an integrator and produces the control voltage for the ILX laser diode controller. The change in the control voltage shifts the CEO frequency.

5.5.1.1 Phase detector response (K_p)

A phase detector converts the difference between a reference frequency (or phase) and a CEO frequency into a voltage signal whose magnitude is proportional to their difference. The response of the phase detector can be measured by using two frequency generators. By changing the relative phase between two inputs into the phase detector, the voltage output can be measured as shown in Figure 5.14. The phase detector has shown the response of phase to voltage (K_p) of 0.596 V/rad. The measurement of the response is required to calculate the integrated phase noise of the f_0 lock.

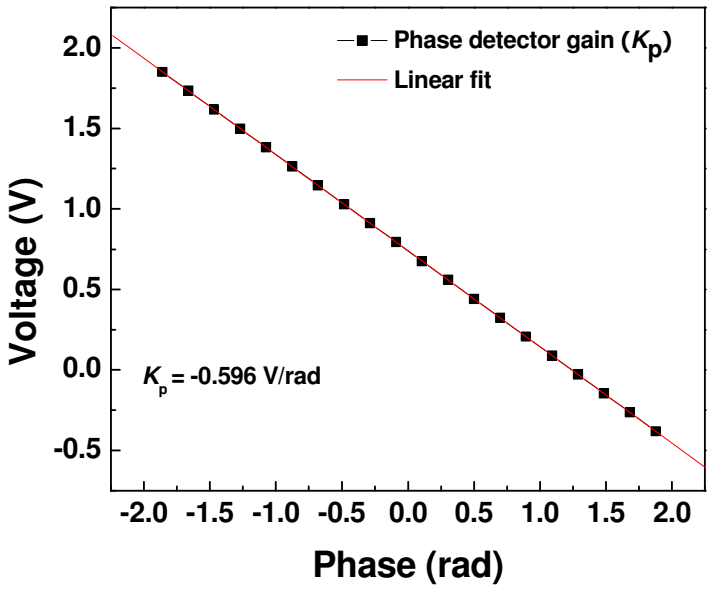

Figure 5.14 Phase detector response (K_p). In order to measure K_p, two inputs possessing a relative phase difference are fed into the phase detector. The difference in the phase of two inputs is converted into a voltage signal, which shows a linear relationship.

5.5.1.2 Servo box transfer function (K_F)

The servo box is the critical part for the feedback control. We used a commercially available servo box (LB1005: Precision photonics). Its transfer function is shown in Figure 5.15 (a).

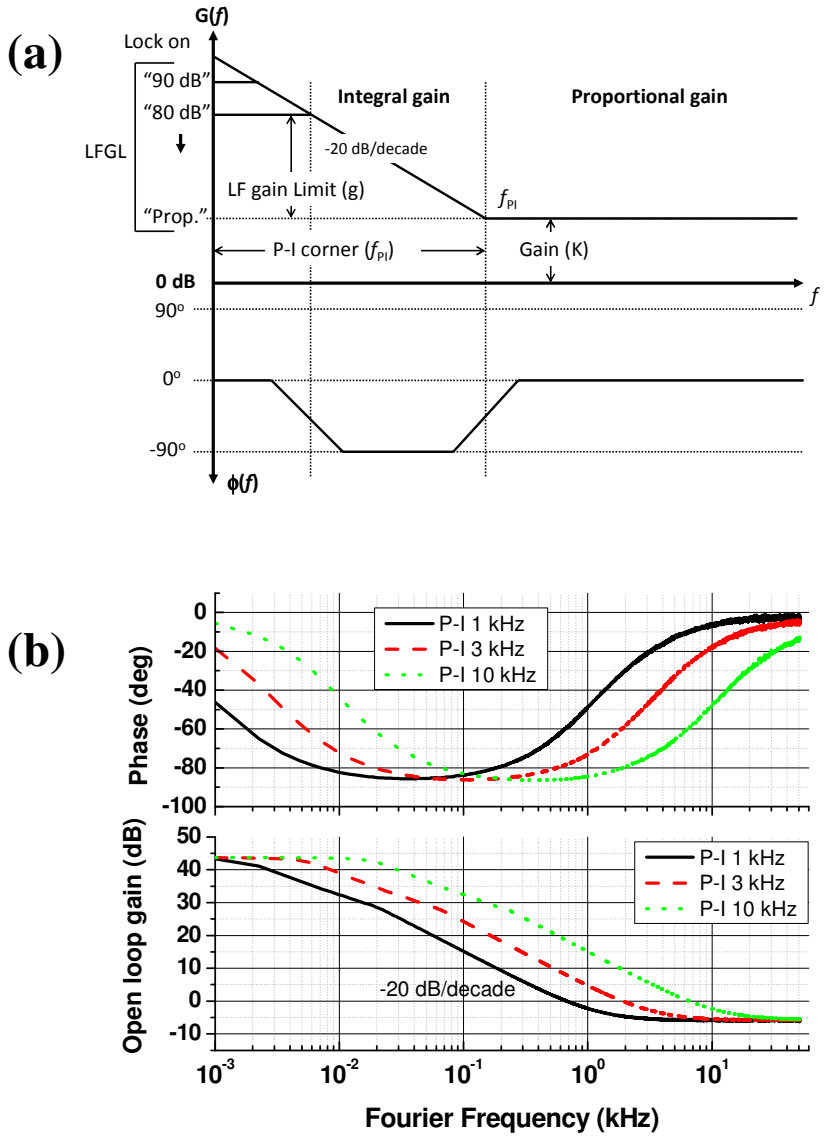

Figure 5.15 (a) Servo box (LB1005: Precision photonics) transfer function from the operation manual. (b) The experimentally measured transfer function of the servo box for the different P-I corner values when LF gain (g) = 60 dB and Gain (K) = 4 (-10 dB).

The available bandwidth of this box is a 10 MHz. The frequency range of integral gain and proportional gain can be chosen by changing P-I corner (f_{PI}) knob. The available proportional gain can be tuned by a Gain (K) knob. It linearly increases the gain from 2-8 corresponding to -30 dB to 30 dB by 10 dB. The low frequency gain below the f_{PI} is adjusted by changing a LF gain (g) knob. The measured transfer function is described in Figure 5.15 (b) which has shown a good agreement with the value given in the specification of LB1005. The

measurement of the transfer function of LB1005 was performed to check the change in the transfer function before and after the modification of the P-I corner. The modification of the P-I corner is required when the laser response is included in our feedback system. A phase-lead compensation circuit can externally change the servo transfer function. This will be dealt in Section 5.7.

5.5.1.3 Laser oscillator response and frequency divider

The response of the laser oscillator was actually measured when we discussed the fixed point measurement. The characteristic response was measured by df_0/dP. The control voltage from the servo box changes the current fed into the laser diode and then the current changes output power of the laser diode. Consequently, the f_0 is changed by the output power. For the CNFL Comb 1, df_0/dP was 4.7×10^7 Hz/mW and for the CNFL Comb 2, df_0/dP was 2.18×10^6 Hz/mW.

Before the f_0 is compared to a reference oscillator (f_{ref}), the f_0 is mixed with a 1 GHz from a local oscillator and a frequency divider is used for the frequency down-conversion. This trick reduces phase noise of the mixed signal by a factor of n_{div} (the ratio of the frequency divider). Therefore, this should be considered when one calculates the integrated phase noise of the f_0 lock. Remember the phase noise is divided down by a factor of n_{div}.

5.6 Phase noise of the CNFL comb lock

The CNFL Comb 1 was phase-locked using two feedback controls. As we mentioned earlier, we used a pump power control for the f_0 stabilization and a cavity length control for the f_r stabilization respectively. Figure 5.16 shows the PSDs of both f_0 lock and f_r lock when the CNFL Comb 1 was fully stabilized. The PSD was recorded from error signals of both servo boxes. The f_r lock was much tighter than the f_0 lock. The integrated phase noise for the f_r lock was less than 0.03 radians. The spikes in the f_r PSD were the harmonics of a 60 Hz. The integrated phase noise for the f_0 lock was ~0.32 radians in the Fourier frequency range from 100 Hz to 102 kHz. Even though the lower phase noise was well suppressed through the feedback control, the noise on the range from 1 kHz to the roll-off frequency remains. The roll-off frequency in the PSD was

corresponding to the characteristic laser response frequency of the Er^{3+} doped fiber laser comb. Therefore the feedback bandwidth using the pump power control is limited by the laser response. However, the feedback bandwidth can be artificially extended using a phase-lead compensation circuit which will discuss in Section 5.7.

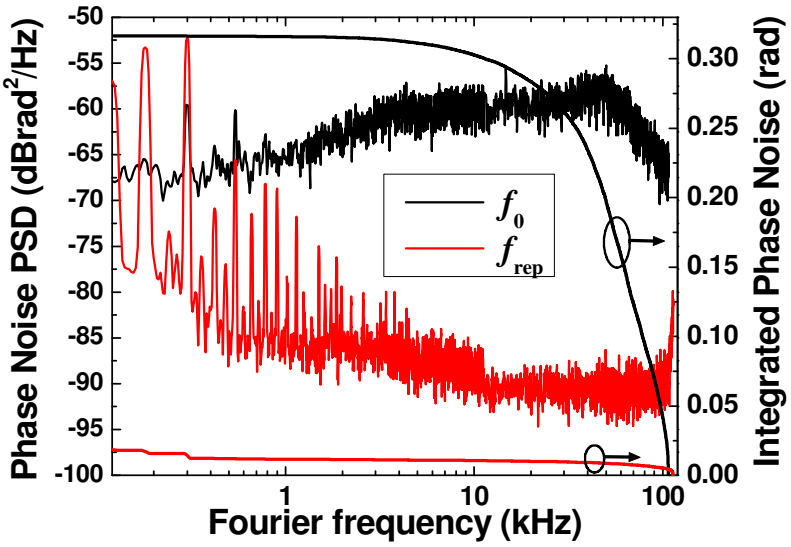

Figure 5.16 The power spectral density (PSD) of the phase-locked f_r and f_0 of the CNFL Comb 1. The integrated phase noises of each lock were calculated. The integrated phase noise of the f_0 error signal was 0.32 radians and that of the f_r error signal was 0.03 radians in the Fourier frequency range from 100 Hz to 102 kHz. Reproduced from Ref. [68].

5.7 Stability of the CNFL comb

5.7.1 Allan deviation

How can we quantify changes of a frequency with time in order to measure the stability of the frequency source? First we can think the standard deviation (SD) but the SD cannot explain these changes correctly because it always gives deviation information from a mean value. Therefore one must use a difference stability measurer known as the Allan Deviation (AD) [129]. The equations for both the SD and the AD are shown below,

$$\mathrm{SD} = \sqrt{\frac{1}{(N-1)}\sum_{i=1}^{N-1}(y_{i+1}-\bar{y})^2} \tag{5.10}$$

and

$$\mathrm{AD} = \sqrt{\frac{1}{2(N-1)}\sum_{i=1}^{N-1}(y_{i+1}-y_i)^2}. \tag{5.11}$$

The SD shows the frequency change from the mean value but the AD represents point to point fluctuation of the frequency source. For calculating the stability of a frequency comb, we used the AD in this thesis.

5.7.2 Fractional stability of the frequency combs

The stabilities of two different frequency combs, F8L Comb and CNFL Comb 1, were calculated using the AD. Both combs have shown instabilities below the reference (a Rb clock disciplined by *GPS*) limit, which is possible if we extend the f_r stability in the RF domain to the f_r stability in the optical frequency domain. However, it may not be true because the motion of the comb teeth is more complicatedly related to noise in the optical frequency regime. The finer measurement can be performed by beating the comb against an external optical frequency source, which will be discussed in Chapter 6.

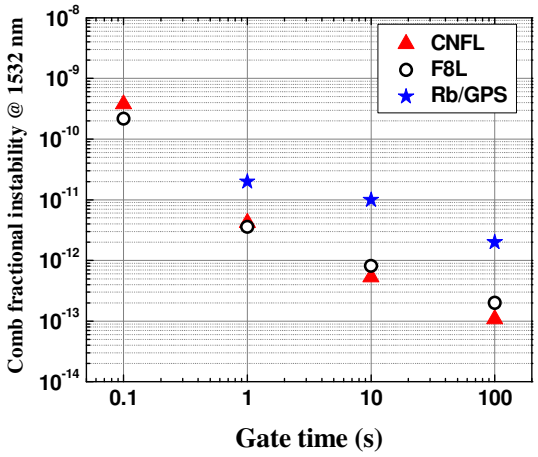

Figure 5.17 Comb fractional instabilities. Both combs have shown the instabilities less than the reference limit.

5.8 Further noise reduction methods

The CNFL Comb 2 was built with a variable repetition (±500 kHz) frequency for multi-heterodyne dual comb spectroscopy [23]. Ultimately, we want to perform the multi-heterodyne spectroscopy using the two low noise CNFL Combs (The CNFL Comb 1 has the fixed repetition frequency). In order to reduce noise of the CNFL Comb 2, we applied two methods. The scheme for the experiment is described in Figure 5.18. One is the phase-lead compensation. The other method is the reduction of pump RIN by operating a laser diode at high power and then we implemented an attenuator to maintain the same power in the laser cavity. The narrow linewidths are critical for multi-heterodyne dual comb spectroscopy. (See Chapter 7)

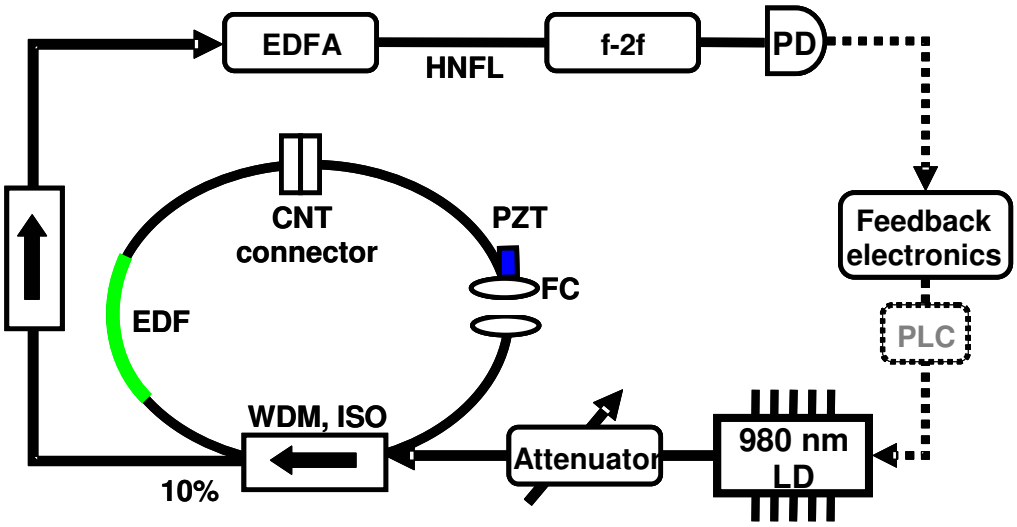

Figure 5.18 Experimental set-up for reducing noise of the CNFL Comb 2. The attenuator and phase-lead compensation (PLC) circuits are equipped. CNT: Carbon nanotube, PZT: piezo-electric transducer, FC: Fiber collimator, EDF: Er^{3+} doped fiber, WDM: Wavelength division multiplexer, ISO: Isolator, EDFA: Er^{3+} doped fiber amplifier, HNFL: Highly nonlinear fiber, PD: Photodetector, and LD: Laser diode.

5.8.1 Phase-lead compensation

For the Er^{3+} doped fiber laser, the f_0 control bandwidth is limited by the laser response (less than 30 kHz for our cases) even though our servo box (LB1005) has a 10 MHz control bandwidth. Therefore we need a method to circumvent this limitation. We implemented a

compensation circuit to extend the control bandwidth called the phase-lead compensation (PLC). The PLC circuit creates a pole in the response function. The design of the circuit is shown in Figure 5.19. It is simply a voltage divider with a capacity connected in parallel. The ratio of capacitance and voltage divider can be changed depending on the laser response and the servo box. Generally, Large capacitance (C) or big resistance (R_1) causes the large RC time constant, so that the pole created by the compensation circuit is laid on the low Fourier frequency. The capacitance (330 pF) and the resistance (50 kΩ) were carefully chosen for the CNFL Comb 2 which has the laser roll-off frequency at 16 kHz.

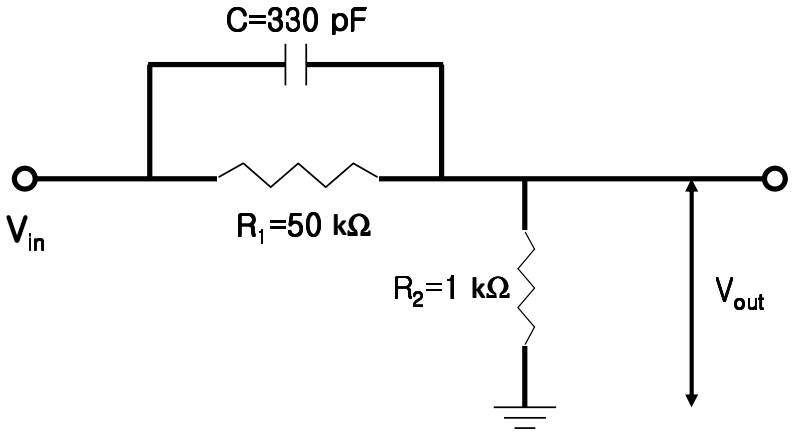

Figure 5.19 The phase-lead compensation circuit design. The values of a resistance and a capacitance shown in this diagram are typically used for the circuit. The variable resistance is used for R_1 to change the RC time constant.

The transfer function for this circuit can be derived in the Laplace domain and the equation is written as the form of

$$H_{PLC}(i\omega) = \frac{1}{1+\dfrac{R_1}{R_2 + (i\omega C R_1 R_2)}}. \tag{5.12}$$

The amplitude response and the phase response can be derived from Eq. (5.12). Figure 5.20 (a) shows the response of the phase-lead compensation circuit. The large capacitance, C (or large resistance, R_1) corresponds to the slow R_1C time constant so that the curves shift to the lower Fourier frequency. The voltage divider ratio was chosen to optimize the output voltage after the phase-lead compensation circuit since the output voltage goes into the ILX current controller

possessing the current to voltage response of a 100 mA/V. The laser can be out of lock when the applied voltage to the ILX current controller is too high. Typically, the voltage applied to the current controller is less than 0.1 V.

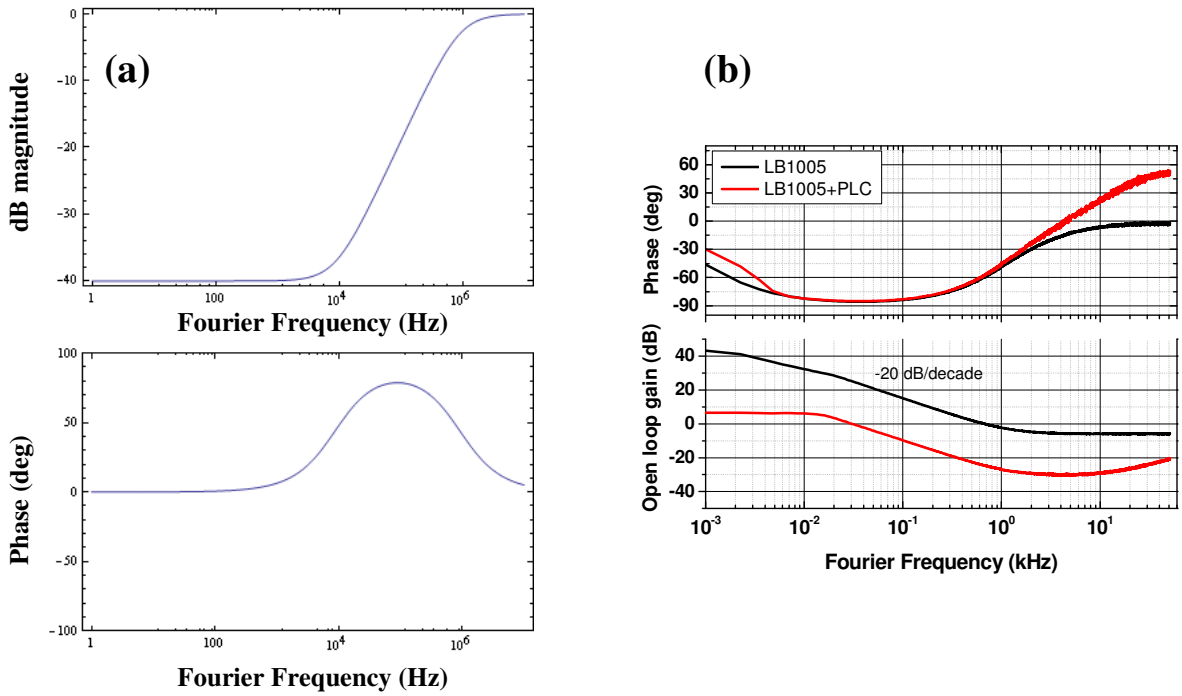

Figure 5.20 (a) A typical transfer function of the phase-lead compensation circuit generated from Eq. (5.12). Both graphs can be shifted by changing the R_1C time constant. (b) The measured transfer functions when the PLC circuit was added to the servo box (LB1005). Due to the PLC circuit, both phase and magnitude were shifted up. The gain with PLC cicuit was reduced because the voltage divider was included in the PLC circuit.

Figure 5.20 (b) shows the changes in transfer functions with the PLC circuit. The resulting frequency response was the sum of the servo box (LB1005) and the PLC circuit.

The laser response creates a roll-off (red-dash in Figure 5.21) in the whole feedback system. This roll-off makes the corresponding 90^o phase shift which degrades stability of the feedback. The added PLC circuit (blue dash) in the feedback loop creates magnitude and phase response as shown in Figure 5.21. The phase response shows that the phase margin (the phase difference between the phase at gain 1 and -180^o) is increased by adding the PLC circuit. The phase margin increases to more than 90^o which guarantees better stability in the feedback system.

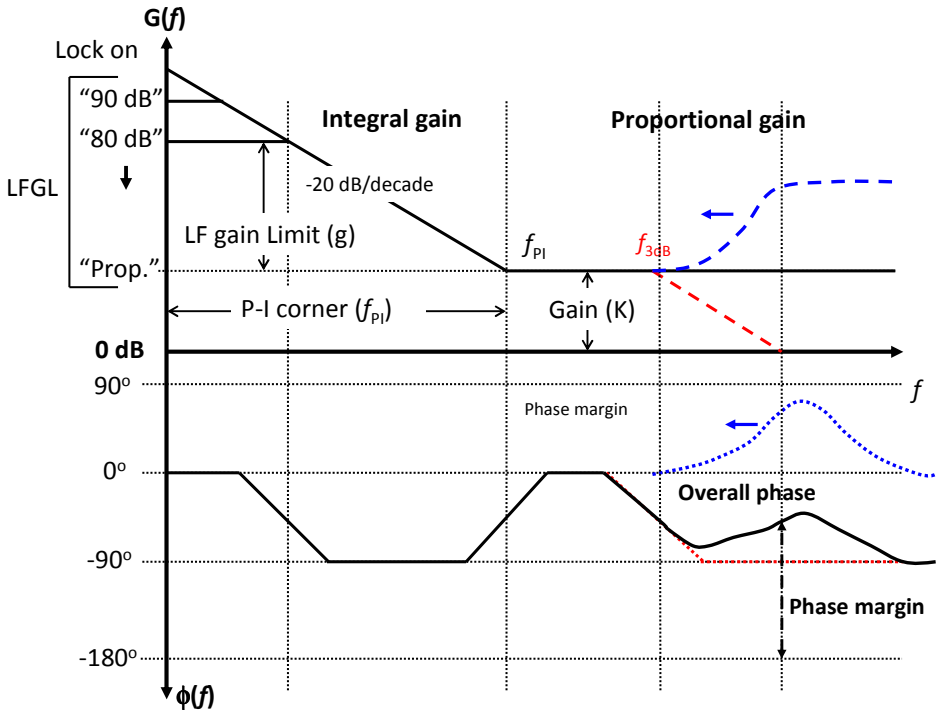

Figure 5.21 The laser response creates a pole (red) with -20 dB/decade at the characteristic roll-off frequency. The phase-lead compensator adds a pole (blue) at the roll-off frequency depending on the time constant. The overall phase response is the sum of the two, which increases the phase-margin to more than 90° and therefore the laser lock is more stable.

5.8.2 Pump power attenuation

References [120, 121] pointed out that a major noise source contributing to the linewidth of comb teeth is the white amplitude noise (or RIN) of the pump laser diode. The combination of RIN and sensitivity of comb modes to pump fluctuation produces the broad linewidth. Therefore, the reduction of RIN is required to minimize the linewidth. In order to reduce RIN of pump laser diode, we implemented a fiber-optic attenuator after the pump laser diode output, so that we were able to increase the pump power without changing the power in the laser cavity. When the applied current to laser diode was increased from 180 mA to 620 mA, the noise on f_0 was reduced by ~5 dB after 1 kHz of Fourier frequencies as shown in Figure 5.22.

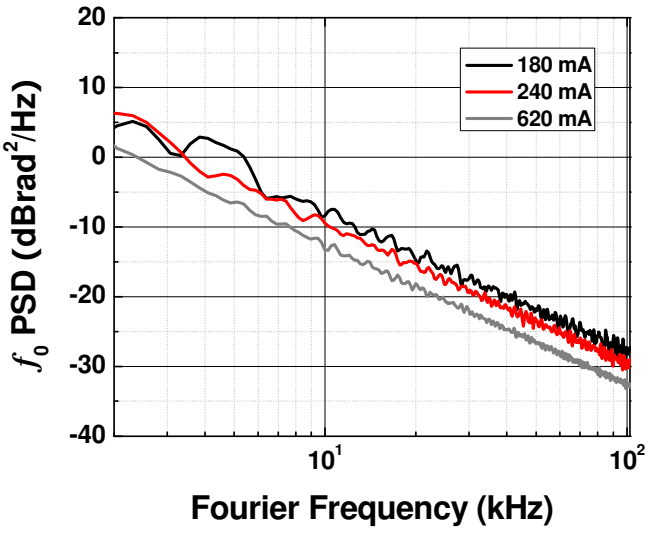

Figure 5.22 PSDs of the CEO frequency of the CNFL Comb 2. The reduction in phase noise is observed above 1 kHz Fourier frequencies by ~ 5 dB, when the current applied to laser diode is increased from 180 mA to 620 mA.

5.8.3 Linewidth of CEO frequency with noise reduction methods

The linewidth of a tooth of the CNFL comb is indirectly measured by measuring its CEO frequency because the linewidth of CEO frequency is a beatnote of two comb teeth which represents the relative linewidth between the teeth, and therefore the linewidth of CEO frequency shows the upper bound of the linewidth of the comb tooth. We employed the two noise reduction methods discussed in the previous sections for the CNFL Comb 2. The free-running f_0 of the CNFL Comb 2 had the linewidth of 850 kHz which was not changed with the feedback control indicating that the noise in high Fourier frequencies was not well eliminated. The lock just helped to fix the peak of f_0. In order to reduce the f_0 linewidth, we added the PLC circuit and the laser roll-off frequency was 16 kHz for the CNFL Comb 2. By adjusting the capacitance and resistance in the PLC circuit, the reduction of the f_0 linewidth was observed. The f_0 linewidth became narrow from 850 kHz to 595 kHz. Dramatic reduction of the f_0 linewidth was achieved when the comb was locked with both the pump attenuation and the PLC circuit simultaneously. The f_0 linewidth was reduced down to 218 kHz by a factor of four from the initial value. The results are shown in Figure 5.23

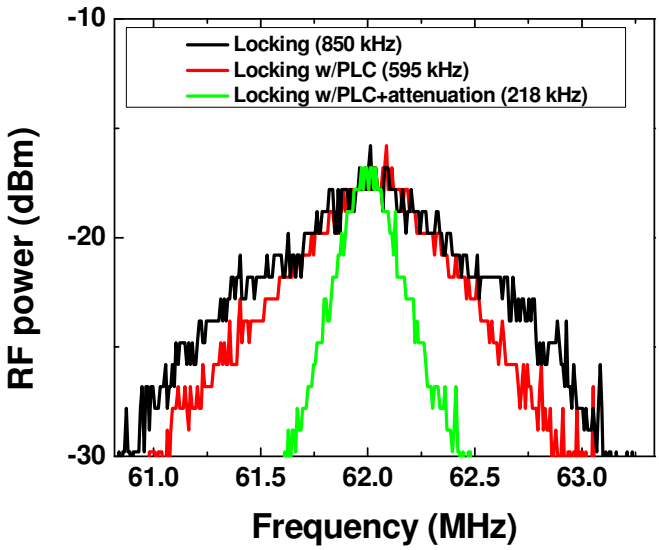

Figure 5.23 The linewidth of the CNFL Comb 2. Lock without the phase-lead compensation and pump attenuation (black); Lock with the phase-lead compensation (Red); Lock with the phase lead-compensation and pump attenuation (Green). Both noise reduction methods were applied to the CNFL Comb 2, the f_0 linewidth was narrowed down from 850 kHz to 218 kHz by a factor of four.

The PSDs of the f_0 error signals for individual locks were recorded and they showed a good agreement with the f_0 linewidths. The less PSD was obtained when the f_0 linewidth was narrower. The PSD has also shown the shift of a servo bump when the PLC circuit was applied. The servo bump is corresponding to the characteristic resonance of a feedback loop. The servo bump was shifted from 30 kHz to 60 kHz. Further shift of the servo bump was not possible. We think that the servo bump at 60 kHz might be due to the resonance of ILX current modulator. Consequently, the PLC circuit enhanced the f_0 lock at higher Fourier frequency components as shown in Figure 5.24. The PSD was minimized when the f_0 linewidth was narrowest. The servo bump was still at 60 kHz but it was suppressed to achieve the best locking performance. The PSD showed noise reduction at the entire Fourier frequencies. In order to check the performance of our f_0 lock, we compared our result to a stabilized NIST Comb although they had a different type of mode-locked mechanisms [121]. For the comparison, the value of phase noise was changed into the value of frequency noise with the relationship of $S_\nu(\nu) = \nu^2 S_\phi(\nu)$, where $S_\nu(\nu)$ stands for frequency noise and $S_\phi(\nu)$ represents phase noise respectively.

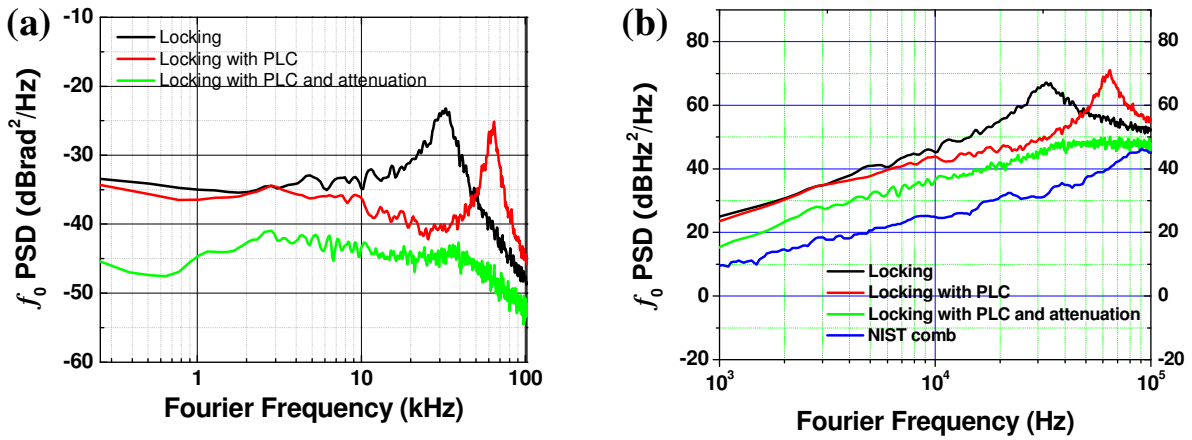

Figure 5.24 (a) f_0 PSD ($S_\phi(\nu)$) of the CNFL Comb 2. Lock without the noise reduction methods (Black). Lock with the PLC circuit (Red). The servo bump was shifted from 30 kHz to 60 kHz which provided tighter lock at high Fourier frequencies. Both PLC and pump attenuation were applied (Green). The f_0 PSD was minimized and the integrated phase noise of the CNFL Comb 2 was 1.6 radians from 100 Hz to 102 kHz. (b) For comparison, the f_0 PSD ($S_\nu(\nu)$) of a NIST Comb was plotted (Blue). The integrated phase noise of the NIST Comb was 0.99 radians up to 500 kHz.

The integrated phase noise has been 1.6 radians for the f_0 lock of our CNFL Comb 2 and that of the NIST comb has shown 0.99 radians. The coherent peak was observed for the NIST Comb when the comb was locked but not for our CNFL Comb 2. We guess that this is because of the difference in reference sources. Their comb was phase-locked to a stable CW laser reference but our CNFL Comb 2 was phase-locked to a RF reference. Some other reasons such as loss and scattering at the SWCNT connector and the relatively large ν_{3dB} might create more noise and degrade the coherence. However, if the lock is tight enough, the ultimate limit may be our RF reference source.

5.9 Summary

We have shown the detection of a CEO frequency for controlling the frequency comb. Since the n^{th} mode of the frequency comb is defined by $\nu_n = n f_r + f_0$, the detection and the

control of f_r and f_0 can fully stabilize the frequency comb. The noise sources of the frequency comb were discussed. The pump-induced amplitude noise combined with the laser's sensitivity to the pump power fluctuation was a major noise source of the CNFL comb. The sensitivity was proportionally increased according to the laser roll-off response, and the higher roll-off frequency of the frequency comb corresponds to high sensitivity to the power fluctuation. The investigation of both one of the major noise sources of the CNFL comb and transfer functions of phase-lock systems led us to the two noise reduction methods. The reduction of pump relative intensity noise reduced the noise spectrum in the laser roll-off frequency and the implementation of the phase-lead compensation circuit allowed the servo control bandwidth increased. The substantial noise reduction was observed by applying the two methods and therefore the f_0 linewidth, the relative linewidth of two comb teeth, was decreased by a factor of four.

In next chapter, we will introduce instability measurements of the CNFL combs and an optical frequency measurement as an application of the fully stabilized CNFL comb.

Note: this research in Chapter 5 has been published in Ref. [68] and submitted to the Conference on Lasers and Electro Optics (CLEO) 2011.

Chapter 6 - Results of Instability of the CNFL Frequency Comb and Absolute Frequency Measurement

6.1 Introduction

We will discuss the instability of our CNFL combs and an absolute optical frequency measurement using the stabilized CNFL comb to a microwave frequency standard, a Rb clock disciplined by GPS. The instability was measured by beating the CNFL comb against a CW laser stabilized to a molecular overtone transition, P(13) of C_2H_2. The absolute frequency of P(13) was calculated. This absolute frequency measurement was mainly done by Kevin Knabe and Chenchen Wang and the result was published in Ref. [69].

6.1.1 Optical frequency comb as a frequency ruler

As we discussed in Chapter 1, the optical frequency comb has revolutionized optical frequency metrology and has realized an optical frequency measurement over a broad spectral bandwidth with simplicity. The frequency comb filled the missing gap between microwave frequencies and optical frequencies in optical frequency metrology. The frequency comb can be stabilized to either a microwave frequency standard such as a Rb oscillator, a Cs oscillator, and a Hydrogen maser or an optical frequency standard such as a CW laser stabilized to the resonance of trapped atoms or single ions. Once the frequency comb is stabilized to those references, the stability and accuracy of the reference is faithfully transferred to the optical frequency comb. Then all comb teeth of the frequency comb are fixed in the frequency domain with known values and they serve as a frequency ruler to measure optical frequencies.

The scheme for the optical frequency measurement is illustrated in Figure 6.1. An optical frequency (f_x) is beaten against the frequency comb tooth in the stabilized frequency comb satisfying the comb equation given by $\nu_n = n f_r + f_0$ and then a heterodyne RF beatnote signal (f_{beat}) is created. The f_{beat} is therefore written as

$$f_{beat} = \left|\nu_n - f_x\right| = n f_r \pm f_0 - f_x \tag{6.1}$$

According to Eq (6.1), the f_x can be calculated and the result is expressed as $f_x = nf_r \pm f_0 - f_{beat}$. The values of f_r, f_0, f_{beat} and n in the equation are experimentally accessible, and therefore the optical frequency can be computed. In practice, the nearest mode number (n) can either be directly measured using a high resolution wave-meter for a high repetition frequency comb (> 100 MHz) or be derived from the Vernier method used in Ref. [123].

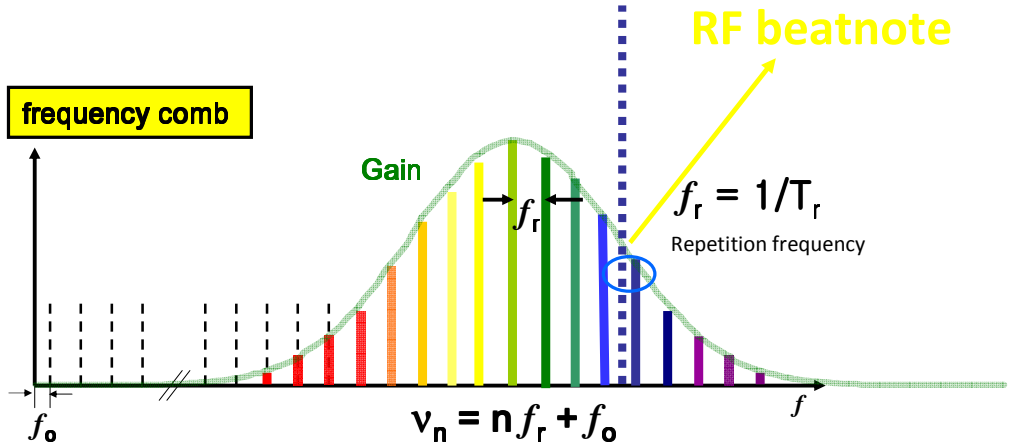

Figure 6.1 The scheme for an optical frequency measurement with a stabilized optical frequency comb. The optical frequency beats against the frequency comb and they create a RF beatnote. The optical frequency comb plays a vital role to connect between an optical frequency and a RF signal.

6.2 The stability of the CNFL comb and an absolute frequency measurement

We demonstrated a phase-stabilized CNFL frequency comb for the first time. The stability of the comb has been measured by beating it against a CW laser stabilized to a molecular overtone transition of C_2H_2. The instability of the CNFL comb was limited by our RF reference source. With the stabilized CNFL frequency comb, we have measured an optical frequency which is discussed in this section.

6.2.1 Stability and accuracy of a frequency source

Before we measured an optical frequency, we first have demonstrated the instability of the CNFL frequency comb. We start with the definition of stability and accuracy of a frequency source. What is required to be the best source for time and frequency reference? The Figure 6.2

shows four situations of the frequency change with time. The first one has a good stability meaning it has regular time interval but does not have accuracy meaning that the time interval is not correct to the frequency standard (fo). The desirable situation is the fourth. It shows both good stability and high accuracy simultaneously. The Allan deviation, point to point fluctuation we discussed in Chapter 5, is used to measure the frequency instability.

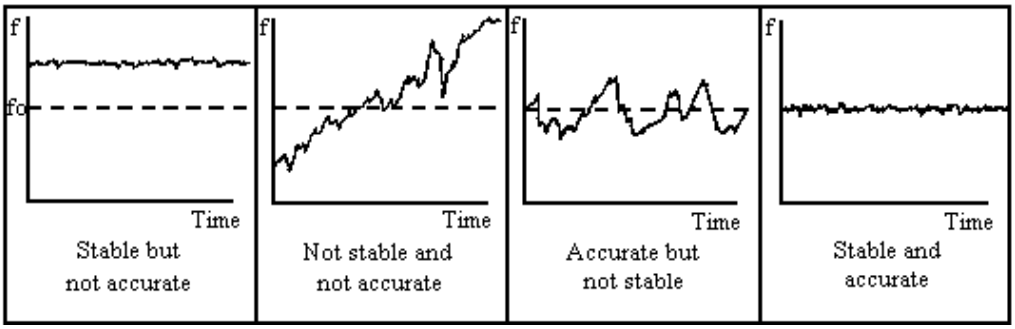

Figure 6.2 Stability and accuracy of time and frequency sources. [143]

6.2.2 Stability of the CNFL comb in the optical frequency region

In Chapter 5, we have shown the instabilities of the two different frequency combs. For the case, we extended our comb instabilities to the optical frequency regime, so that the fractional instabilities were better than our RF reference source. Practically, the motion of the comb modes may be more complicated in optical frequency regime due to the variety of noise sources of the comb and the multiplication factor, n, in the comb equation may degrade the stability. In this section, we directly carried out the measurement of comb instability in the optical frequency region. In order to do that, an external optical reference source was used. Hence the stability of the CNFL Comb 1 was measured by beating the comb against a stabilized CW laser to C_2H_2 molecular overtone transition at ~1532 nm. In this way, we were capable of measuring instabilities of both the CNFL Comb 1 and the optical frequency reference simultaneously.

The stabilized optical frequency we used for the stability measurement was generated by saturated absorption spectroscopy (SAS) [69]. The scheme for SAS is depicted in Figure 6.3. C_2H_2 molecules were trapped in a Kagome photonic crystal fiber. The pump and probe technique was implemented to detect a sub-Doppler feature and then the frequency modulation was applied in order to achieve a control signal which was the derivative of the sub-Doppler feature.

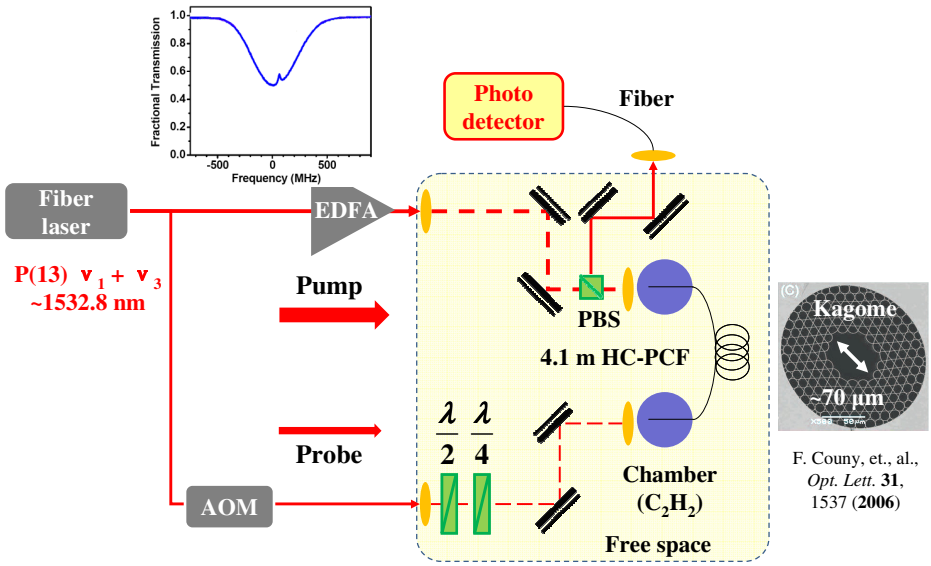

Figure 6.3 A CW laser stabilized to a C_2H_2 molecular overtone transition. The acetylene was loaded into a Kagome photonic crystal fiber. The pump and probe technique was used to detect a saturated absorption signal and frequency modulation was implemented to stabilize the CW laser to the absorption signal [24].

6.2.3 Beating the comb against the CW laser

The stabilized CNFL Comb 1 possessing the repetition frequency of ~167 MHz was beaten against a stabilized CW laser. The experimental set-up is illustrated in Figure 6.4. The supercontinuum spectrum of the CNFL Comb 1 was filtered with a reflecting fiber Bragg grating (FBG) centered at 1532 nm and its spectral bandwidth of 30 GHz. Then the frequency comb was coupled with a portion of a CW laser and a RF beatnote was detected using a fast photodetector. The RF beatnote (f_{beat}) between the comb and the CW laser was filtered using a microwave bandpass filter and amplified in order to count it. The fractional instability was calculated and the result was shown in Figure 6.5. The calculated fractional instability (Δf_{beat}/1532 nm) in the optical frequency region was 1.2×10^{-11} at 1 sec averaging time and the instability was limited by our reference source, a Rb clock disciplined by *GPS*. At the short averaging times, the instability has been limited by the reference source of the frequency comb but the instability was dominated by the CW laser at the longer gate time. Therefore, the frequency comb has shown faithful transferability of the RF reference source.

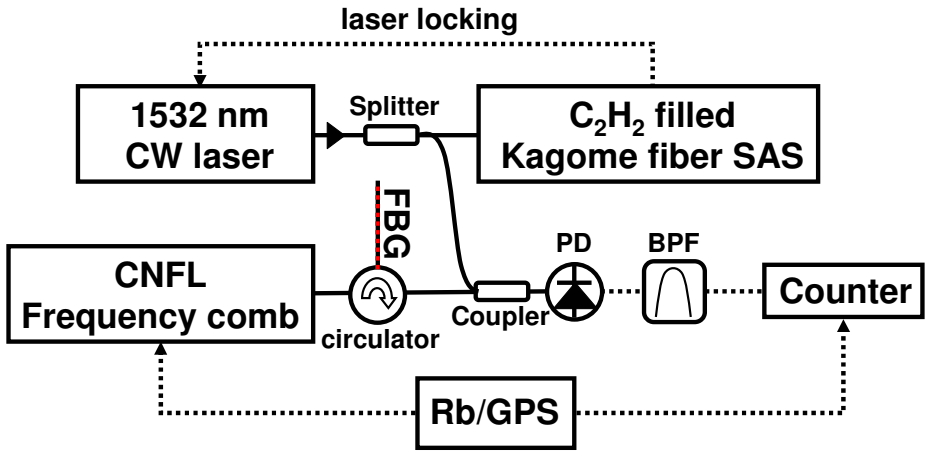

Figure 6.4 Experimental set-up for beating CNFL comb against a CW laser stabilized to C_2H_2 overtone molecular transition using SAS. FBG: fiber Bragg grating, BPF: band pass filter, PD: Photodetector.

6.2.4 Beyond the reference limit

We have seen that the stability of CNFL Comb 1 was limited by the RF reference source we have used. In order to see the instability beyond the RF reference limit, we have performed a additional measurement. For the experiment, a stabilized Cr:Forsterite frequency comb was added to the previous set-up in Figure 6.4 [124] and the new experimental set-up was shown in Figure 6.5.

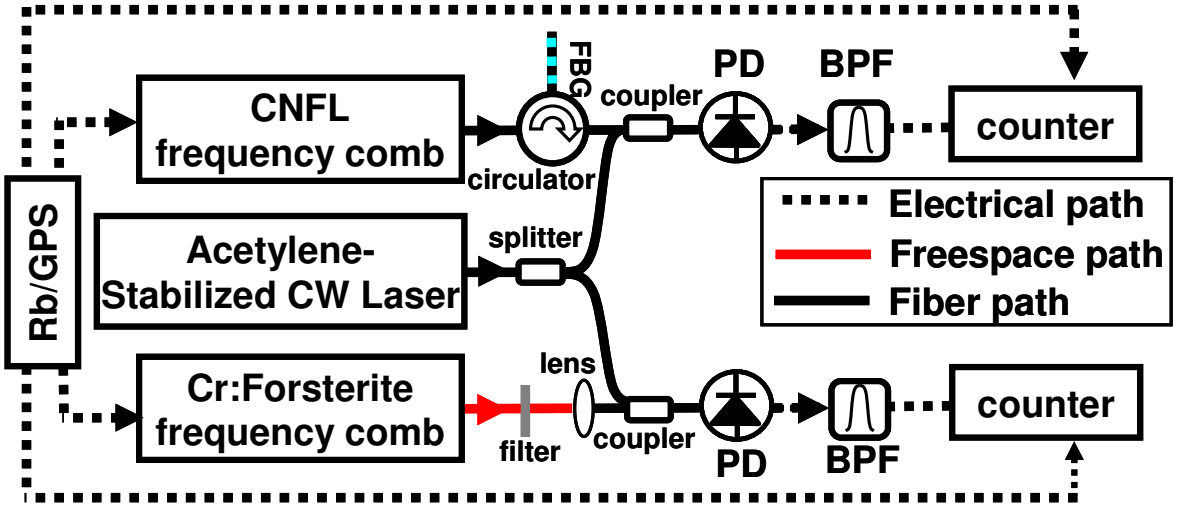

Figure 6.5 Experimental set-up for the measurement. Both stabilized combs (CNFL Comb 1 and Cr:Forsterite Comb) are filtered and beaten against a CW laser stabilized to a C_2H_2 overtone transition. Two beatnotes are simultaneously counted.

Both stabilized frequency combs were filtered and beaten against a common CW laser stabilized to C_2H_2 overtone transition at the same time. The RF beatnotes were detected for both and were counted simultaneously. The two measured beatnotes were subtracted from each other, so that the stability of the reference was effectively eliminated from the result. The fractional instability was calculated at the optical frequency, 1532 nm and it was below the reference limit as shown in Figure 6.6 which represented the instability upper bound of one of the combs. The result shows that the ultimate limit of our comb stability is set by the reference but not by the comb itself.

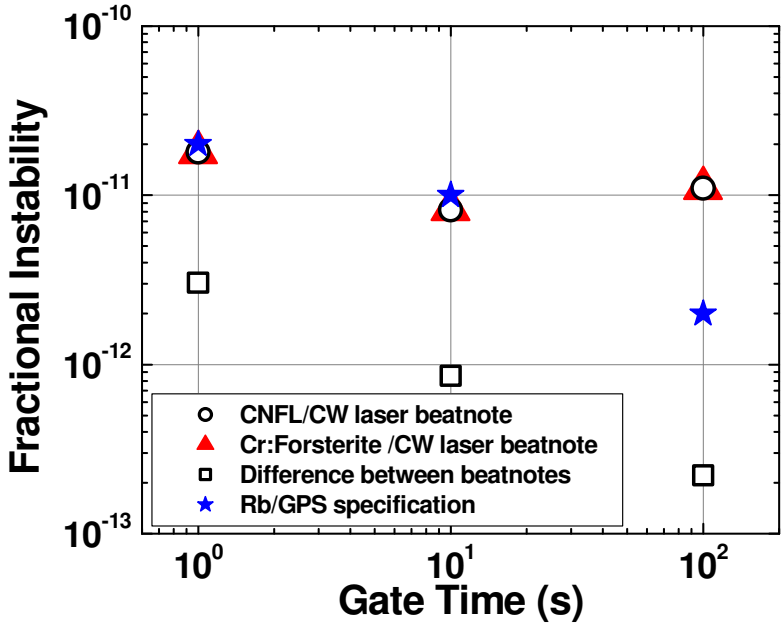

Figure 6.6 Fractional instabilities of the CNFL Comb 1, the Cr:Forsterite Comb, and the difference between their RF beatnotes against the C_2H_2 stabilized CW laser. The stability of both combs was limited by the same RF reference source. The reference source was effectively removed by looking at the difference between the two RF beatnotes and its fractional instability was below the reference limit. This sets the instability upper bound of one of the combs. Reproduced from Ref. [125]

6.2.5 Result for the absolute frequency measurement of P(13)

An molecular overtone transition of C_2H_2, P(13), was measured using the CNFL Comb 1 [24]. Due to the limited tuning range of the repetition frequency, the measurement of the mode

number discussed by Long-Sheng Ma *et al*. in Ref. [123] was not implemented to calculate the absolute frequency. The method is also discussed in the K. Knabe's thesis and paper [69]. Instead, we used *a priori* knowledge of the frequency we measured which was obtained from our previous absolute frequency measurement with the Cr:Forsterite frequency comb using the method in Ref. [123]. In other words, one just knows the approximated absolute frequency in advance but not the exact number. Then one measures and finds out the nearest mode number of the comb by beating against the absolute frequency and calculates the absolute frequency using the experimentally obtained mode number. When the measured value is close to the approximated absolute frequency value, one changes the repetition frequency and repeats the previous steps. Since the repetition frequency was changed, the nearest mode number also changed. Then one calculates the absolute frequency with the new mode number to see if there is consistency between previously calculated absolute frequency values. These steps are repeated and the values are then averaged. The measured mean value has shown a good agreement with other group's measurement within the error bar and the error in accuracy was below 10 kHz.

In order to increase the tuning range of the repetition frequency of the CNFL frequency comb, we are planning to add the high dynamic range PZT micrometer in the laser cavity. Therefore, an absolute frequency will be measured by the method used in Ref. [123] without knowing *a priori* information about the frequency we want to measure.

6.3 Summary

The stabilized CNFL frequency comb has shown the RF reference-limited instability and the fractional instability was 1.2×10^{-11} at 1 sec averaging time. The proof of upper bound of the CNFL frequency comb instability has been done by subtracting two RF beatnote signals produced by beating two different frequency combs against a common CW laser stabilized to a molecular overtone transition of C_2H_2, P(13) respectively. The direct beating between the two different frequency combs was not measured due to the difficulty in a temporal overlap between the pulses from two different mode-locked laser oscillators. The f_r of the Cr:Forsterite frequency comb was 113 MHz and that of the CNFL Comb 1 was 167 MHz respectively. The direct beating of the two frequency combs has been realized using two CNFL frequency combs

possessing the same repetition frequency and the result will be discussed in the next chapter. The measurement has shown that the instability of the CNFL combs is not limited by our RF reference. We will also show the measured relative linewidth between the two CNFL Combs at 1555 nm.

The optical frequency, P(13), has been measured with the stabilized CNFL Comb 1 and the value has shown a good agreement with previously known data and the error in accuracy has been within 10 kHz.

Chapter 7 - Conclusions and Future Work

7.1 Principle Research Contributions

This research has been focused on making the Er^{3+} doped fiber laser frequency comb more compact, robust, and cost-effective without losing stability and accuracy of the previously existing fiber frequency combs. We ultimately aimed at8 making the frequency comb be a field-usable turn-key device. We report the first phase-stabilized Er^{3+} doped fiber laser frequency comb employing a single walled carbon nanotube as a saturable absorber to achieve a passive mode-locking, which allows for a simple, easy, and cost-effective fabrication of the femtosecond fiber laser cavity. The substantial reduction of the cavity length is realized because of the SWCNT saturable absorber and therefore an all-fiber high repetition frequency (>150 MHz) mode-locking was demonstrated. The high repetition frequency is desirable for our use in optical frequency metrology because it allows for enhancing the resolving power between the comb teeth. We also demonstrated the high power Er^{3+} doped fiber amplifier (EDFA) producing a 430 mW average power and ~120 fs pulse duration at the repetition frequency of 167 MHz using a parabolic pulse amplification. The output power was limited by the available pump power. These results are comparable to the recent Er^{3+} doped mode-locked fiber amplifier products at 1560 nm. Especially by using a hollow core photonic bandgap fiber (HC-PBGF) to linearly compress the dispersion after the Er^{3+} doped fiber (EDF), we produced the pedestal-free short pulse with the high pulse energy owing to the very small nonlinearity of the HC-PBGF. From the assist of the EDFA we generated a high power supercontinuum source from a carbon nanotube fiber laser (CNFL) oscillator which includes the greater power per comb tooth or being equally true for the increased measurement sensitivity of the comb.

The phase-stabilized CNFL Comb 1 has shown the accumulated phase noise of 0.32 radians from 100 Hz to 102 kHz for the f_0 phase-lock. The further investigation of the comb instability was done by beating the comb against a CW laser stabilized to an overtone transition of C_2H_2 molecules. The measured fractional instability was 1.2×10^{-11} at 1 s averaging time and the result was limited by our reference source, a Rb clock steered by *GPS*. The laser was able to be phase-stabilized for more than 6 hours without any active temperature control.

The absolute frequency of an overtone transition of C_2H_2 molecules was measured with the phase-stabilized CNFL comb within 10 kHz uncertainty and it has shown a good agreement with the previous measurements done by other groups. These are remarkable results showing that the CNFL comb can be a truly field-usable and turn-key research instrument.

In order to extend the application of the CNFL comb to the multiheterodyne dual comb spectroscopy, we have also investigated the noise of the CNLF comb. The major noise source was the relative intensity noise (RIN) of the oscillator pump laser diode and the control bandwidth of CEO frequency (f_0) was limited by the laser response frequency (ν_{3dB}). In order to reduce the noise in the CNFL comb, we have implemented a phase-lead compensation circuit and a pump power attenuation method. The combination of those approaches has allowed the substantial reduction of noise in the CNFL comb, so that the f_0 linewidth has been narrower from 850 kHz to 220 kHz by a factor of four. The residual noise may be our RF reference or some other noise sources in the CNFL such as loss and scattering at the SWCNT connector and should be further investigated. In summary, the principle contributions have been made through this research,

- The high repetition frequency (> 150MHz) erbium doped fiber laser frequency comb using a single walled carbon nanotube saturable absorber has been obtained.

- A parabolic pulse amplifier possessing the output average power of 430 mW has been made and has been used for the supercontinuum generation using a highly nonlinear fiber.

- All-fiber linear pulse compression has been done with HC-PBGF. It has shown the low pedestal pulse due to the very low nonlinear effect of HC-PBGF

- The first fully phase-stabilized erbium doped carbon nanotube fiber laser frequency comb has been realized.
  - The comb has been stabilized for more than 6 hours without active temperature controls.
  - The comb has the fractional instability of 1.2×10^{-12} at 1 s averaging time which is the reference-limited stability.

- An optical frequency of C_2H_2 overtone transition, P(13), has been measured using the phase-stabilized CNFL comb and the measurement uncertainty was within 10 kHz accuracy.

- We have shown that the main noise source of the CNFL comb was the relative intensity noise (RIN) of the pump laser diode. The further noise reduction of CNFL comb has bee achieved both by implementing the phase-lead compensation and by reducing the RIN of pump laser diode simultaneously. Therefore, the linewidth of CEO frequency has been reduced from 850 kHz to 220 kHz.

7.2 Future work and direction

7.2.1 Scaling up the average power of a high repetition frequency CNFL

Although the CNFL comb has shown excellent performances for optical frequency metrology in near infrared there is a drawback which should be overcome for the CNFL comb to be more wildly applicable. For instance, we are making a set-up for the multi-heterodyne dual comb spectroscopy in our laboratory. For the experiment, a higher average power is desirable because the comb should effectively interact with target gases. The detail for the multi-heterodyne dual comb spectroscopy will be discussed in Section 7.3. Since the high repetition frequency mode-locked fiber laser has a short cavity length, the stored energy in the cavity is small. Therefore in order to increase the average output power, the gain fiber should be strongly pumped. However this posed a problem that was the damage of the SWCNT at the fiber connector end-face due to the heat deposition. Our research has shown that the SWCNT deposited at fiber connector end-face was destroyed over 50 mW average power at 1550 nm in the laser cavity. This significantly limited the obtainable output power. The second problem was the relatively slow recovery time (~1 ps) and low saturable fluence of the SWCNT saturable absorber which caused the CNFL to be multiple pulsing as the pump power increased. So far, the highest average power for the CNFL possessing over the repetition frequency of 150 MHz by using the optically driven direct SWCNT deposition method was about 1 mW before the multiple

pulsing arises. In order to overcome and achieve an order of magnitude higher average power we are trying a different deposition method and are using the evanescent interaction between the pulse and the SWCNTs in HC-PBGF. We are anticipating that this method allows for avoiding heat damage and alleviating the multiple pulsing. However when the HC-PBGF was incorporated into the fiber laser cavity, it has shown the Fresnel reflection (4 %) between the fiber interfaces due to the difference in refractive indices. This prevented the laser from the mode-locking. Therefore we are moving to a direction to use polymer composite to eliminate the Fresnel reflection. We have had a challenge with this direction but it would be possible in the near future.

7.2.2 Multi-heterodyne dual comb spectroscopy

More applications of the CNFL combs could be found in precision spectroscopy. One approach is the cavity ring down spectroscopy using a frequency comb and it has shown an excellent performance in detecting atoms and molecules with rapid and high sensitivity [22]. For the case, the frequency comb was coupled into an optical cavity which improved the interaction and measurement sensitivity to detect target gases at once. The other approach is the multi-heterodyne dual comb spectroscopy [23]. Two phase-stabilized combs possessing a very small difference in the repetition frequency (Δf_r) are used for the spectroscopy. A RF comb is produced when two combs are optically filtered and beaten against each other as shown in Figure 7.1. The RF comb has the repetition frequency of Δf_r and the Δf_r is typically a few kHz. Therefore, the linewidth of comb modes are important to distinguish the RF comb modes so that the resolution of spectroscopy can be improved.

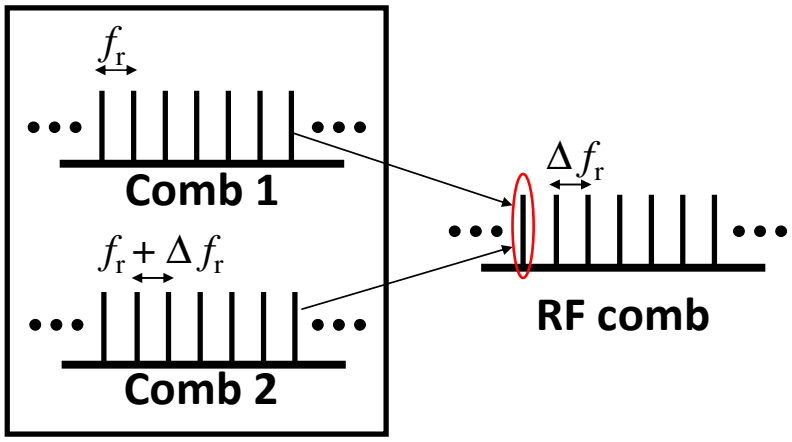

Figure 7.1 Schematic diagram of multi-heterodyne dual comb spectroscopy. The combs have a small difference in the repetition frequency by Δf_r. When the two combs are filtered and beaten, a RF comb possessing the repetition frequency of Δf_r is generated.

In order to perform dual comb spectroscopy, we measured the relative linewidth of the comb teeth before we heterodyne-beat against the two stabilized CNFL combs possessing the repetition frequency of ~167 MHz each other. The CNFL Comb 2 has a free-space in the laser cavity and therefore the repetition frequency can be tuned by several hundreds of kHz. For the experiment, we made the repetition frequencies of both combs same and a common RF local synthesizer referenced by Rb clock disciplined by *GPS* was used for locking both f_rs but the f_0s were locked with different local synthesizers at different RFs. The experimental set-up is illustrated in Figure 7.2.

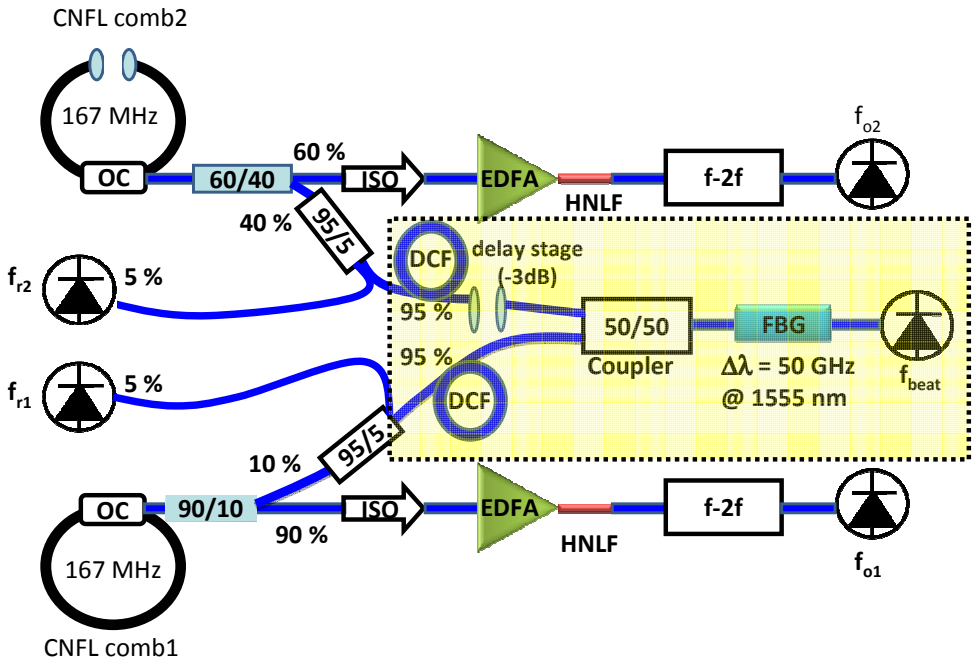

Figure 7.2 Experimental set-up for beating two stabilized CNFL combs. Both combs have the same repetition frequency of ~167 MHz. A common synthesizer referenced by Rb clock disciplined by GPS was used for locking both f_rs. The CNFL Comb 2 has a free-space in the laser cavity to tune the repetition frequency by several hundreds of kHz. Two pulses from different laser oscillators were temporally overlapped using DCF (Delay compensation fibers: Coring SMF-28e) and a free-space delay stage. The overlapped pulses were filtered by a FBG centered at 1555 nm with 50 GHz spectral bandwidth. The beatnote (f_{beat}) between two CNFL combs were detected.

The two combs were beaten directly. The temporal delay between two pulses from the different laser oscillators was compensated using the Corning SMF-28e and a fine tune was achieved with a free space delay stage for one of paths. The delay between two pulses was monitored by a fast oscilloscope (1 GHz) and we checked the relative pulse arrival time from two different oscillators. The peak in the oscilloscope was maximized when two pulses were overlapped. Then the overlapped pulses were filtered by a reflected fiber Bragg grating centered at 1555 nm with the spectral bandwidth of 50 GHz. The RF beatnote between two CNFL combs (f_{beat}) was shown in Figure 7.3.

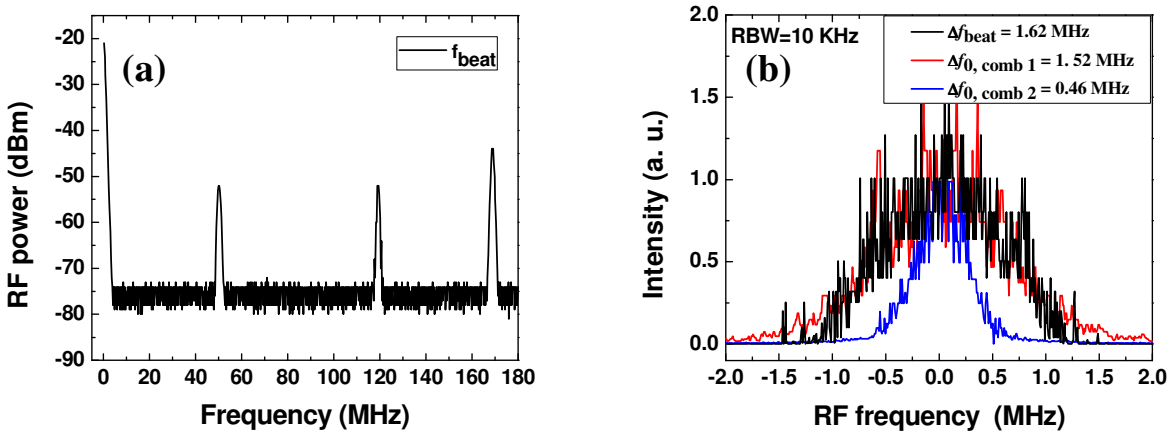

Figure 7.3 (a) Beatnote (f_{beat}) between two CNFL combs with the SNR of 25 dB. (b) The linewidth of f_{beat}. The f_0 linewiths of both combs are also plotted. The linewidth of f_{beat} is dominated by the linewidth of the worse f_0 linewidth between the two frequency combs.

The beatnote frequency was just difference in f_0s of both combs. The result can be mathematically described by the frequency comb mode equation.

$$\begin{aligned} \nu_{n1} &= n_1 f_{r1} \pm f_{o1} \\ \nu_{n2} &= n_2 f_{r2} \pm f_{o2} \end{aligned} \tag{7.1}$$

where f_{r1} and f_{r2} are the repetition frequency of the CNFL Comb 1 and the CNFL Comb 2 respectively and f_{01} and f_{02} are the CEO frequencies of the CNFL Comb 1 and the CNFL Comb 2 respectively. Therefore, f_{beat} between the two combs is written as

$$f_{beat} = n_1 f_{r1} - n_2 f_{r2} \pm f_{o1} \mp f_{o2}\,. \tag{7.2}$$

Since $f_{r1} = f_{r2}$, therefore $f_{beat} = \pm f_{o1} \mp f_{o2}$ .The relative linewidth of the two CNFL frequency combs at 1550 nm was 1.6 MHz that corresponded to the worse f_0 linewidth between the two frequency combs.

The f_{beat} was counted with both CEO frequencies at 1 s averaging time. The fluctuation in f_{beat} (Δf_{beat}) was larger than the fluctuations in both f_0s (Δf_{01} and Δf_{01} respectively) as shown in

Figure 7.4. This means that the repetition frequencies for both CNFL Combs are not fully synchronized. From Eq. (7.2), the Δf_{beat} is defined as

$$\Delta f_{beat} = n_1 \Delta f_{r1} - n_2 \Delta f_{r2} \pm \Delta f_{o1} \mp \Delta f_{o2}. \tag{7.3}$$

For the same mode numbers ($n_1 = n_2 = n$), Eq. (7.3) becomes

$$\Delta f_{beat} = n(\Delta f_{r1} - \Delta f_{r2}) \pm \Delta f_{o1} \mp \Delta f_{o2}. \tag{7.4}$$

As we see in Figure 7.4, the Δf_{beat} was not dominated either Δf_{01} or Δf_{02}. Therefore, we can conclude that the Δf_{beat} was governed by n (Δf_{r1}-Δf_{r2}) term and $n \sim 1.15012 \times 10^6$, which means that $\Delta f_{r1} \neq \Delta f_{r2}$ and therefore the two combs are not fully synchronized to the common RF reference for f_rs.

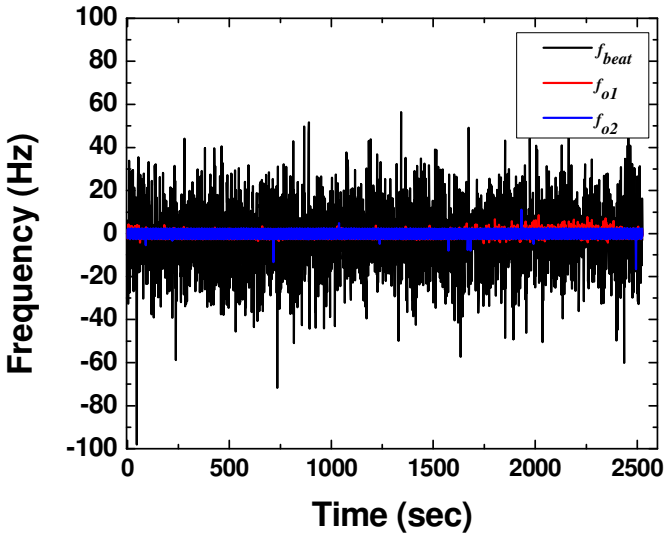

Figure 7.4 Counted f_{beat}, f_{01}, and f_{02} at 1 s averaging time. The fluctuation of f_{beat} (Δf_{beat}) was dominated by n (Δf_{r1}-Δf_{r2}) term but not by either f_{01} or f_{02}, which means that the two CNFL Combs were not fully synchronized to the common reference for f_r s.

We calculated the fractional instability of f_{beat} which has shown $1.0 \times 10^{-13}\ \tau^{-1/2}$, where τ is the averaging time. The result is shown in Figure 7.5. Since the reference source from both

combs was effectively removed, the fraction instability was able to be below the reference limit as we predicted in Section 6.2.4. However, this result shows that coherence between two combs is imperfect and may indicate the noise of frequency combs or technical noise for this measurement such as path length fluctuation.

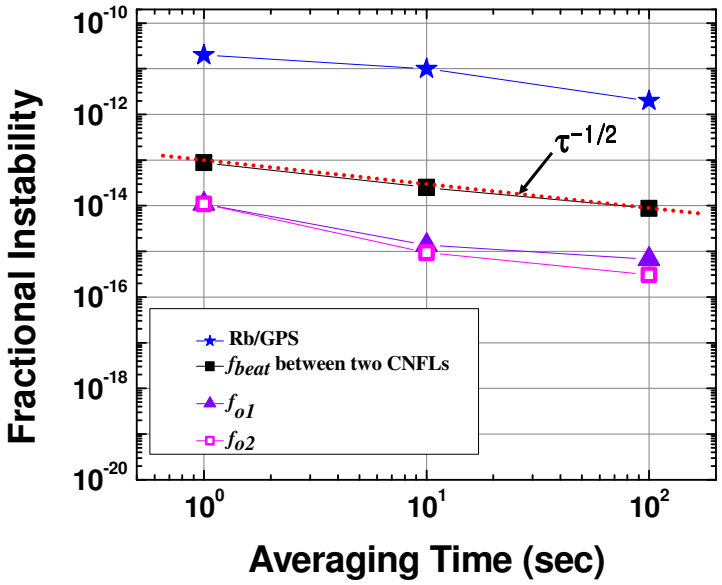

Figure 7.5 Fractional instability of f_{beat} which has shown $1.0 \times 10^{-13}\ \tau^{-1/2}$.

So far, we are focusing on the reduction of noise in both CNFL combs to achieve narrow relative linewidth between comb teeth. When we understand the noise of CNFL frequency comb and realize the further noise reduction, beating two CNFL combs and producing a RF comb will be the following step for the multi-heterodyne dual comb spectroscopy.

7.2.3 Mid-IR frequency comb

The other important application of frequency comb can be found in precision spectroscopy in the mid-IR regime which is the wavelength of 3-12 μm or even higher. Many rovibrational absorptions of interesting atoms and molecules exist in that range, for example, as shown in Figure 7.6. Therefore, it is very desirable to have a comb at the wavelength. Many efforts are still going to achieve the mid-IR comb. So far, the mid-IR comb has been achieved using parametric processes such as a difference frequency generation [126] or an optical parametric oscillator [28]. However, both methods increase the complexity and cost of the

system. Another approach is to use a CNFL comb centered at 2 μm and then one can apply the same approach that we have discussed in this thesis to make a stabilized mid-IR comb. The biggest issue is to find correct nonlinear crystals for the second harmonic generation and to fabricate the periodic pole structure and anti-reflection coating for the crystal.

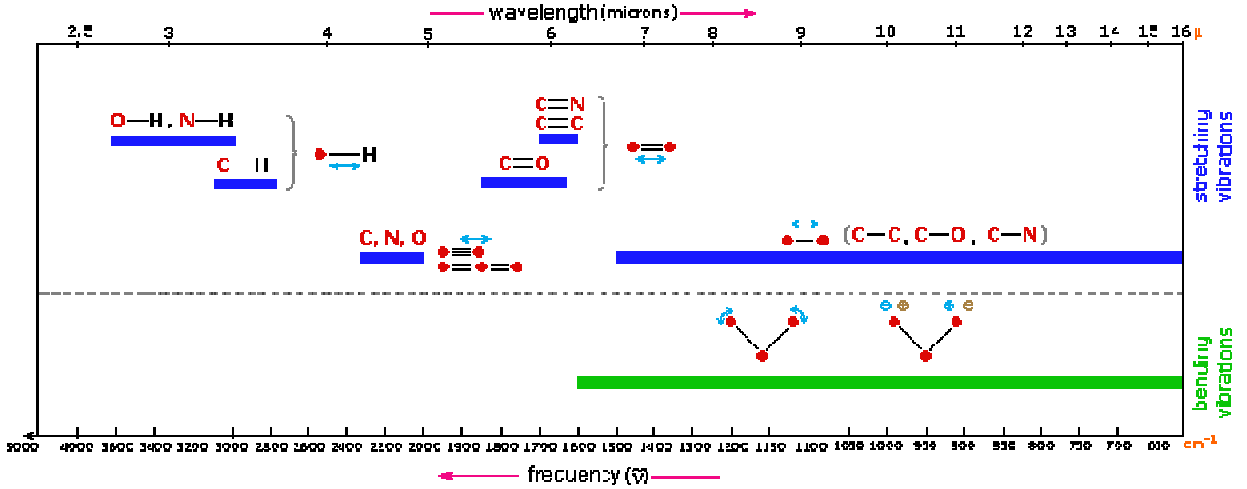

Figure 7.6 Rovibrational absorptions of molecules in the mid-IR regime. Reproduced from Ref [148]

References

1. Udem, Th., et al., *Phase-Coherent Measurement of the Hydrogen 1S-2S Transition Frequency with an Optical Frequency Interval Divider Chain.* Physical Review Letters, 1997. **79**(14): p. 2646.

2. Schwob, C., et al., *Optical Frequency Measurement of the 2S-12D Transitions in Hydrogen and Deuterium: Rydberg Constant and Lamb Shift Determinations.* Physical Review Letters, 1999. **82**(25): p. 4960.

3. Niering, M., *Measurement of the hydrogen 1S-2S transition frequency by phase coherent comparison with a microwave cesium fountain clock.* Phys. Rev. Lett., 2000. **84**: p. 5496-5499.

4. Udem, Th., R. Holzwarth, and T. W. Hansch, *Optical frequency metrology.* Nature, 2002. **416**(6877): p. 233-237.

5. Hall, J. L., *Optical frequency measurement: 40 years of technology revolutions.* Selected Topics in Quantum Electronics, IEEE Journal of, 2000. **6**(6): p. 1136-1144.

6. Webb, J. K., *Further evidence for cosmological evolution of the fine structure constant.* Phys. Rev. Lett., 2001. **87**: p. 091301-1-091301-4.

7. Dirac, P. A. M., *The cosmological constants.* Nature, 1937. **139**: p. 323-323
.
8. Rosenband, T., et al., *Frequency Ratio of Al^+ and Hg^+ Single-Ion Optical Clocks; Metrology at the 17th Decimal Place.* Science, 2008. **319**(5871): p. 1808-1812.

9. Hensley, J. M., *A Precision Measurement of the Fine Strucure Constant*. 2001.

10. Rafac, R. J., et al., *Sub-dekahertz Ultraviolet Spectroscopy of $^{199}Hg^+$*. Physical Review Letters, 2000. **85**(12): p. 2462.

11. Wilpers, G., et al., *Optical Clock with Ultracold Neutral Atoms.* Physical Review Letters, 2002. **89**(23): p. 230801.

12. Kleppner, D., *A Milestone in Time Keeping.* Science, 2008. **319**(5871): p. 1768-1769.

13. Evenson, K. M., et al., *Accurate frequencies of molecular transitions used in laser stabilization: the 3.39 μm transition in CH_4 and the 9.33 and 10.18 μm transitions in CO_2.* Applied Physics Letters, 1973. **22**(4): p. 192-195.

14. Schnatz, H., et al., *First Phase-Coherent Frequency Measurement of Visible Radiation.* Physical Review Letters, 1996. **76**(1): p. 18.

15. Schnatz, H., et al., *Extension of the PTB frequency chain towards the Ca intercombination line at 657 nm.* Instrumentation and Measurement, IEEE Transactions on, 1993. **42**(2): p. 273-275.

16. Jones, D. J., *Carrier-envelope phase control of femtosecond mode-locked lasers and direct optical frequency synthesis.* Science, 2000. **288**: p. 635-639.

17. Udem, Th., et al., *Absolute Frequency Measurements of the Hg^+ and Ca Optical Clock Transitions with a Femtosecond Laser.* Physical Review Letters, 2001. **86**(22): p. 4996.

18. Jun, Y., H. Schnatz, and L.W. Hollberg, *Optical frequency combs: from frequency metrology to optical phase control.* Selected Topics in Quantum Electronics, IEEE Journal of, 2003. **9**(4): p. 1041-1058.

19. Schibli, T. R., et al., *Frequency metrology with a turnkey all-fiber system.* Opt. Lett., 2004. **29**(21): p. 2467-2469.

20. Diddams, S. A., et al., *Standards of Time and Frequency at the Outset of the 21st Century.* Science, 2004. **306**(5700): p. 1318-1324.

21. Schibli, T. R., et al., *Phase-locked widely tunable optical single-frequency generator based on a femtosecond comb.* Opt. Lett., 2005. **30**(17): p. 2323-2325.

22. Thorpe, M. J., et al., *Broadband Cavity Ringdown Spectroscopy for Sensitive and Rapid Molecular Detection.* Science, 2006. **311**(5767): p. 1595-1599.

23. Coddington, I., W. C. Swann, and N. R. Newbury, *Coherent Multiheterodyne Spectroscopy Using Stabilized Optical Frequency Combs.* Physical Review Letters, 2008. **100**(1): p. 013902.

24. Diddams, S. A., L. Hollberg, and V. Mbele, *Molecular fingerprinting with the resolved modes of a femtosecond laser frequency comb.* Nature, 2007. **445**(7128): p. 627-630.

25. Li, C. -H., et al., *A laser frequency comb that enables radial velocity measurements with a precision of 1cm s^{-1}.* Nature, 2008. **452**(7187): p. 610-612.

26. Ozawa, A., et al., *High Harmonic Frequency Combs for High Resolution Spectroscopy.* Physical Review Letters, 2008. **100**(25): p. 253901.

27. Gohle, C., et al., *A frequency comb in the extreme ultraviolet.* Nature, 2005. **436**(7048): p. 234-237.

28. Adler, F., et al., *Phase-stabilized, 1.5 W frequency comb at 2.8-4.8 μm.* Opt. Lett., 2009. **34**(9): p. 1330-1332.

29. Teets, R., et al., *Coherent Two-Photon Excitation by Multiple Light Pulses.* Physical Review Letters, 1977. **38**(14): p. 760.

30. Spence, D. E., P. N. Kean, and W. Sibbett, *60-fsec pulse generation from a self-mode-locked Ti:sapphire laser.* Opt. Lett., 1991. **16**(1): p. 42-44.

31. Ranka, J. K., R. S. Windeler, and A. J. Stentz, *Visible continuum generation in air-silica microstructure optical fibers with anomalous dispersion at 800 nm.* Opt. Lett., 2000. **25**(1): p. 25-27.

32. Washburn, B. R., et al., *Phase-locked, erbium-fiber-laser-based frequency comb in the near infrared.* Opt. Lett., 2004. **29**(3): p. 250-252.

33. Swann, W. C., et al., *Fiber-laser frequency combs with subhertz relative linewidths.* Opt. Lett., 2006. **31**(20): p. 3046-3048.

34. Newbury, N. R. and W. C. Swann, *Low-noise fiber-laser frequency combs (Invited).* J. Opt. Soc. Am. B, 2007. **24**(8): p. 1756-1770.

35. Long-Sheng, M., et al., *A new method to determine the absolute mode number of a mode-locked femtosecond-laser comb used for absolute optical frequency measurements.* Selected Topics in Quantum Electronics, IEEE Journal of, 2003. **9**(4): p. 1066-1071.

36. Diddams, S. A., et al., *An Optical Clock Based on a Single Trapped $^{199}Hg^{+}$ Ion.* Science, 2001. **293**(5531): p. 825-828.

37. Ludlow, A. D., et al., *Sr Lattice Clock at 1×10^{-16} Fractional Uncertainty by Remote Optical Evaluation with a Ca Clock.* Science, 2008. **319**(5871): p. 1805-1808.

38. Collis, R. T. H., *Lidar Observation of Cloud.* Science, 1965. **149**(3687): p. 978-981.

39. Diddams, S. A., *Direct link between microwave and optical frequencies with a 300 THz femtosecond laser comb.* Phys. Rev. Lett., 2000. **84**: p. 5102-5105.

40. Holzwarth, R., *Optical frequency synthesizer for precision spectroscopy.* Phys. Rev. Lett., 2000. **85**: p. 2264-2267.

41. Shelton, R. K., et al., *Phase-Coherent Optical Pulse Synthesis from Separate Femtosecond Lasers.* Science, 2001. **293**(5533): p. 1286-1289.

42. Steinmetz, T., et al., *Laser Frequency Combs for Astronomical Observations.* Science, 2008. **321**(5894): p. 1335-1337.

43. Walker, G., *Extrasolar planets: With a coarse-tooth comb.* Nature, 2008. **452**(7187): p. 538-539.

44. Baltuska, A., et al., *Attosecond control of electronic processes by intense light fields.* Nature, 2003. **421**(6923): p. 611-615.

45. Jun, Y., et al. *Precise phase control of short pulses*. in *Quantum Electronics and Laser Science, 2003. QELS. Postconference Digest*. 2003.

46. Xu, L., *Route to phase control of ultrashort light pulses.* Opt. Lett., 1996. **21**: p. 2008-2010.

47. Apolonski, A., *Controlling the phase evolution of few-cycle light pulses.* Phys. Rev. Lett., 2000. **85**: p. 740-743.

48. Kienberger, R., et al., *Steering Attosecond Electron Wave Packets with Light.* Science, 2002. **297**(5584): p. 1144-1148.

49. Telle, H. R., et al., *Carrier-envelope offset phase control: a novel concept for absolute optical frequency measurement and ultrashort pulse generation.* Appl. Phys. B, 1999. **69**: p. 327-332.

50. Paul, P. M., et al., *Observation of a Train of Attosecond Pulses from High Harmonic Generation.* Science, 2001. **292**(5522): p. 1689-1692.

51. Milosevic, N., A. Scrinzi, and T. Brabec, *Numerical Characterization of High Harmonic Attosecond Pulses.* Physical Review Letters, 2002. **88**(9): p. 093905.

52. Hentschel, M., et al., *Attosecond metrology.* Nature, 2001. **414**(6863): p. 509-513.

53. Marian, A., et al., *United Time-Frequency Spectroscopy for Dynamics and Global Structure.* Science, 2004. **306**(5704): p. 2063-2068.

54. Thorpe, M. J., et al., *Cavity-enhanced optical frequency combspectroscopy: application to human breathanalysis.* Optics Express, 2008. **16**(4): p. 2387-2397.

55. Udem, Th., *Absolute frequency measurements of the Hg^+ and Ca optical clock transitions with a femtosecond laser.* Phys. Rev. Lett., 2001. **86**: p. 4996-4999.

56. Stenger, J., *Phase-coherent frequency measurement of the Ca intercombination line at 657 nm with a Kerr-lens mode-locked femtosecond laser.* Phys Rev. A, 2001. **63**: p. 021802-1-021802-4.

57. Pokasov, P. V., *Proc. Sixth Symp. Freq. Standards Metrol*. 2002.

58. Nevsky, A. Y., *Frequency comparison and absolute frequency measurement of I_2 stabilized lasers at 532 nm.* Opt. Comm., 2001. **263**: p. 192-272.

59. Stenger, J., et al., *Absolute frequency measurement of the 435.5 nm 171Yb^{+} clock transition with a Kerr-lens mode-locked femtosecond laser.* Opt. Lett., 2001. **26**: p. 1589-1591.

60. Ramsey, N. F., *History of early atomic clocks.* Metrologia, 2005. **42**(3): p. S1-S3.

61. Bartels, A., et al., *Mode-locked laser pulse trains with subfemtosecond timing jitter synchronized to an optical reference oscillator.* Opt. Lett., 2003. **28**(8): p. 663-665.

62. Diddams, S. A., et al., *A femtosecond-laser-based optical clockwork with instability 6.3 × 10^{-16} in 1 s.* Opt. Lett., 2002. **27**: p. 58-58.

63. Ma, L. -S., et al., *Optical Frequency Synthesis and Comparison with Uncertainty at the 10^{-19} Level.* Science, 2004. **303**(5665): p. 1843-1845.

64. Brown, H., *Planetary Systems Associated with Main-Sequence Stars.* Science, 1964. **145**(3637): p. 1177-1181.

65. Webbink, R.F., *Binary Systems.* Science, 1979. **203**(4379): p. 430-431.

66. Nicholson, J. W. and D. J. DiGiovanni, *High-Repetition-Frequency Low-Noise Fiber Ring Lasers Mode-Locked With Carbon Nanotubes.* Photonics Technology Letters, IEEE, 2008. **20**(24): p. 2123-2125.

67. Set, S. Y., et al., *Ultrafast fiber pulsed lasers incorporating carbon nanotubes.* Selected Topics in Quantum Electronics, IEEE Journal of, 2004. **10**(1): p. 137-146.

68. Lim, J. K., et al., *A phase-stabilized carbon nanotube fiber laser frequency comb.* Optics Express, 2009. **17**(16): p. 14115-14120.

69. Knabe, K., et al., *10 kHz accuracy of an optical frequency reference based on $^{12}C_2H_2$-filled large-core kagome photonic crystal fibers.* Optics Express, 2009. **17**(18): p. 16017-16026.

70. Haus, H. A., *Mode-locking of lasers.* Selected Topics in Quantum Electronics, IEEE Journal of, 2000. **6**(6): p. 1173-1185.

71. Lin, C., et al., *Phase matching in the minimum-chromatic-dispersion region of single-mode fibers for stimulated four-photon mixing.* Opt. Lett., 1981. **6**(10): p. 493-495.

72. Stolen, R. H. and E. P. Ippen, *Raman Gain in Glass Optical waveguides.* Applied Physics Letters, 1973. **22**(6): p. 276-278.

73. Stolen, R. H., et al., *Raman response function of silica-core fibers.* J. Opt. Soc. Am. B, 1989. **6**(6): p. 1159-1166.

74. Haus, H. A., et al., *Stretched-pulse additive pulse mode-locking in fiber ring lasers: theory and experiment.* Quantum Electronics, IEEE Journal of, 1995. **31**(3): p. 591-598.

75. Renninger, W. H., A. Chong, and F. W. Wise, *Dissipative solitons in normal-dispersion fiber lasers.* Physical Review A, 2008. **77**(2): p. 023814.

76. Oktem, B., C. Ulgudur, and F. O. Ilday, *Soliton-similariton fibre laser.* Nat Photon. **4**(5): p. 307-311.

77. Hasegawa, A. and F. Tappert, *Transmission of stationary nonlinear optical pulses in dispersive dielectric fibers. I. Anomalous dispersion.* Applied Physics Letters, 1973. **23**(3): p. 142-144.

78. Allain, J. Y., et al., *High-efficiency ytterbium-doped fluoride fibre laser.* Journal of Non-Crystalline Solids, 1993. **161**: p. 270-273.

79. Fermann, M. E., et al., *Nonlinear amplifying loop mirror.* Opt. Lett., 1990. **15**(13): p. 752-754.

80. Tai, K., A. Hasegawa, and A. Tomita, *Observation of modulational instability in optical fibers.* Physical Review Letters, 1986. **56**(2): p. 135.

81. Anderson, D. and M. Lisak, *Modulational instability of coherent optical-fiber transmission signals.* Opt. Lett., 1984. **9**(10): p. 468-470.

82. Hasegawa, A., *Generation of a train of soliton pulses by induced modulational instability in optical fibers.* Opt. Lett., 1984. **9**(7): p. 288-290.

83. Karlsson, M., *Modulational instability in lossy optical fibers.* Journal of the Optical Society of America B-Optical Physics, 1995. **12**(11): p. 2071-2077.

84. Duling, I.N., *Subpicosecond all-fiber erbium laser.* Electronics Letters, 1991. **27**(6): p. 544-545.

85. Namiki, S. and H.A. Haus, *Noise of the stretched pulse fiber laser. I. Theory.* Quantum Electronics, IEEE Journal of, 1997. **33**(5): p. 649-659.

86. Tamura, K., et al., *77-fs pulse generation from a stretched-pulse mode-locked all-fiber ring laser.* Opt. Lett., 1993. **18**(13): p. 1080-1082.

87. Washburn, B. R., W. C. Swann, and N. R. Newbury, *Response dynamics of the frequency comb output from a femtosecond fiber laser.* Optics Express, 2005. **13**(26): p. 10622-10633.

88. Kelly, S. M. J., *Characteristic side-band instability of periodically amplified average solition.* Electronics Letters, 1992. **28**(8): p. 806-807.

89. Keller, U., *Recent developments in compact ultrafast lasers.* Nature, 2003. **424**(6950): p. 831-838.

90. Keller, U., et al., *Semiconductor saturable absorber mirrors (SESAM's) for femtosecond to nanosecond pulse generation in solid-state lasers.* Selected Topics in Quantum Electronics, IEEE Journal of, 1996. **2**(3): p. 435-453.

91. Schibli, T., et al., *Ultrashort pulse-generation by saturable absorber mirrors based on polymer-embedded carbon nanotubes.* Optics Express, 2005. **13**(20): p. 8025-8031.

92. Haiml, M., R. Grange, and U. Keller, *Optical characterization of semiconductor saturable absorbers.* Applied Physics B-Lasers and Optics, 2004. **79**(3): p. 331-339.

93. Iijima, S., *Helical microtubules of graphitic carbon.* Nature, 1991. **354**(6348): p. 56-58.

94. Byun, H., et al., *Compact, stable 1 GHz femtosecond Er-doped fiber lasers.* Applied Optics. **49**(29): p. 5577-5582.

95. Nicholson, J. W., R. S. Windeler, and D. J. DiGiovanni, *Optically driven deposition of single-walled carbon-nanotube saturable absorbers on optical fiber end-faces.* Optics Express, 2007. **15**(15): p. 9176-9183.

96. Chen, Y. C., et al., *Ultrafast optical switching properties of single-wall carbon nanotube polymer composites at 1.55 μm.* Applied Physics Letters, 2002. **81**(6): p. 975-977.

97. Yim, J. H., et al., *Fabrication and characterization of ultrafast carbon nanotube saturable absorbers for solid-state laser mode locking near 1 μm.* Applied Physics Letters, 2008. **93**(16): p. 161106-3.

98. Solodyankin, M. A., et al., *Mode-locked 1.93 μm thulium fiber laser with a carbon nanotube absorber.* Opt. Lett., 2008. **33**(12): p. 1336-1338.

99. Desurvire, E., J. R. Simpson, and P. C. Becker, *High-gain erbium-doped traveling-wave fiber amplifier.* Opt. Lett., 1987. **12**(11): p. 888-890.

100. Nicholson, J. W., et al., *All-fiber, octave-spanning supercontinuum.* Opt. Lett., 2003. **28**(8): p. 643-645.

101. Anderson, D., et al., *Wave-breaking-free pulses in nonlinear-optical fibers.* J. Opt. Soc. Am. B, 1993. **10**(7): p. 1185-1190.

102. Barnes, W. L., et al., *Absorption and emission cross section of Er^{3+} doped silica fibers.* Quantum Electronics, IEEE Journal of, 1991. **27**(4): p. 1004-1010.

103. DeMartini, F., et al., *Self-Steepening of Light Pulses.* Physical Review, 1967. **164**(2): p. 312.

104. Tomlinson, W. J., R. H. Stolen, and A.M. Johnson, *Optical wave breaking of pulses in nonlinear optical fibers.* Opt. Lett., 1985. **10**(9): p. 457-459.

105. Fermann, M. E., et al., *Self-Similar Propagation and Amplification of Parabolic Pulses in Optical Fibers.* Physical Review Letters, 2000. **84**(26): p. 6010.

106. Ilday, F., et al., *Self-Similar Evolution of Parabolic Pulses in a Laser.* Physical Review Letters, 2004. **92**(21): p. 213902.

107. Kruglov, V. I., et al., *Self-similar propagation of high-power parabolic pulses in optical fiber amplifiers.* Opt. Lett., 2000. **25**(24): p. 1753-1755.

108. Dudley, J. M., et al., *Self-similarity in ultrafast nonlinear optics.* Nature Physics, 2007. **3**(9): p. 597-603.

109. Yin, L., Q. Lin, and G. P. Agrawal, *Soliton fission and supercontinuum generation in silicon waveguides.* Opt. Lett., 2007. **32**(4): p. 391-393.

110. Sala, K., G. Kenney-Wallace, and G. Hall, *CW autocorrelation measurements of picosecond laser pulses.* Quantum Electronics, IEEE Journal of, 1980. **16**(9): p. 990-996.

111. Amezcua-Correa, R., et al., *Control of surface modes in low losshollow-core photonic bandgap fibers.* Optics Express, 2008. **16**(2): p. 1142-1149.

112. Knight, J. C., *Photonic crystal fibers and fiber lasers (Invited).* J. Opt. Soc. Am. B, 2007. **24**(8): p. 1661-1668.

113. Knight, J. C., et al., *Endlessly single-mode photonic crystal fibre.* Opt. Lett., 1996. **22**: p. 961-964.

114. Wadsworth, W. J., *Soliton effects in photonic crystal fibres at 850 nm.* Electron. Lett., 2000. **36**: p. 53-53.

115. Birks, T. A., W. J. Wadsworth, and P. S. J. Russell, *Supercontinuum generation in tapered fibres.* Opt. Lett., 2000. **25**: p. 1415-1417.

116. Husakou, A. V. and J. Herrmann, *Supercontinuum generation, four-wave mixing, and fission of higher-order solitons in photonic-crystal fibers.* J. Opt. Soc. Am. B, 2002. **19**(9): p. 2171-2182.

117. Wadsworth, W. J., et al., *Supercontinuum generation in photonic crystal fibers and optical fiber tapers: a novel light source.* J. Opt. Soc. Am. B, 2002. **19**(9): p. 2148-2155.

118. Corwin, K. L., et al., *Fundamental Noise Limitations to Supercontinuum Generation in Microstructure Fiber.* Physical Review Letters, 2003. **90**(11): p. 113904.

119. Newbury, N. R. and B. R. Washburn, *Theory of the frequency comb output from a femtosecond fiber laser.* Quantum Electronics, IEEE Journal of, 2005. **41**(11): p. 1388-1402.

120. McFerran, J. J., et al., *Elimination of pump-induced frequency jitter on fiber-laser frequency combs.* Opt. Lett., 2006. **31**(13): p. 1997-1999.

121. McFerran, J. J., et al., *Suppression of pump-induced frequency noise in fiber-laser frequency combs leading to sub-radian f_{ceo} phase excursions.* Applied Physics B: Lasers and Optics, 2007. **86**(2): p. 219-227.

122. Telle, H. R., B. Lipphardt, and J. Stenger, *Kerr-lens, mode-locked lasers as transfer oscillators for optical frequency measurements.* Applied Physics B-Lasers and Optics, 2002. **74**(1): p. 1-6.

123. Ma, L. S., et al., *Frequency Uncertainty for Optically Referenced Femtosecond Laser Frequency Combs.* Quantum Electronics, IEEE Journal of, 2007. **43**(2): p. 139-146.

124. Tillman, K. A., et al., *Stabilization of a self-referenced, prism-based, Cr:forsterite laser frequency comb using an intracavity prism.* Appl. Opt., 2009. **48**(36): p. 6980-6989.

125. Lea, S. N., *Proc. Sixth Symp. Freq. Standards Metrol*. 2002.

126. Erny, C., et al., *Mid-infrared difference-frequency generation of ultrashort pulses tunable between 3.2 and 4.8 ?m from a compact fiber source.* Opt. Lett., 2007. **32**(9): p. 1138-1140.

127. www.nobelprize.org/nobel_prizes/physics/laureates/2005/hansch_lecture.pdf/

128. http://www.menlosystems.com/

129. http://www.allanstime.com/AllanVariance/

130. http://www.cvimellesgriot.com/products/Documents/Catalog/Dispersion_Equations.pdf

131. J. Senior, *Optical Fiber Communications, Principles and Practice, 2nd Ed.* (Prentice-Hall, New York, 1992.), p.65

132. G. P. Agrawal, *Nonlinear fiber optics, 4th Ed.* (Academic Press, New York, 2007), p.41

133. M. Bass, et al., *Handbook of Optics Vol. 4, 2nd Ed.* (McGraw Hill, New York), p.3.3

134. http://www.nufern.com/fiber_detail.php/66

135. A. E. Siegman, *in Lasers, edited by A. Kelly* (University Science Books, Sausalito, CA, 1986), p.1041-1103

136. K. R. Tamura, *Thesis: Additive Pulse Mode-Locked Erbium-Doped Fiber Lasers,* MIT (1994)

137. E. O. Goebel, *Ultrafast Spectroscopy of Semiconductors*, in Advances in Solid State Physics 30, p. 269-294 (1990)

138. A. E. Siegman, *in Lasers, edited by A. Kelly* (University Science Books, Sausalito, CA, 1986), p.102-115

139. E. Desurvire, *Erbium-Doped Fiber Amplifiers, Prinples and Applications,* (Wiley-Interscience, New York, 1994)

140. LEE. M. Frantz and John S. Nodvik*, Theory of Puls Propagation in a Laser Amplifier,* Journal of applied physics (1963), **34**(8), p. 2346-2349

141. G. P. Agrawal, *Nonlinear fiber optics, 4th Ed.* (Academic Press, New York, 2007), p.51-55

142. Y. Wang, J. Lim, R. Amezcua-Correa, J. C. Knight, and B. R. Washburn, *Sub-33 fs Pulses from an All-Fiber Parabolic Amplifier Employing Hollow-Core Photonic Bandgap Fiber,* in Proceedings of Frontiers in Optics, (Optical Society of America, 2008)

143. http://tf.nist.gov/general/glossary.htm

144. J. Ye and S. T. Cundiff, *Femtosecond optical frequency comb technology: Principle, operation, and application.* (Springer, New York, 2005)

145. S. O. Kasap, *Optoelectronics and photonics: Principle and Practices.* (Pearson, 2001)

146. B. R. Washburn, *Dispersion and nonlinearities associated with supercontinuum generation in microstructure fibers,* (Dissertation, 2002)

147. G. P. Agrawal, *Nonlinear fiber optics, 4th Ed.* (Academic Press, New York, 2007), p.31-62

148. http://chemwiki.ucdavis.edu/Wikitexts/UCD_Chem_205:_Larsen/

149. David W. Allan et al., *The science of time keeping, Application note 1289*, Hewlett-Packard (1997)

Appendix A – Notations

a	Fiber core radius
$\tilde{A}(t)$	Complex electric field of a transform-limited pulse
$A_0(t)$	Pulse envelope with the slowly varying envelope approximation
c	Speed of light
C	Capacitance
D	Dispersion parameter
D_{slope}	Dispersion slope
$\tilde{D}$	Complex electric displacement
$\hat{D}$	Dispersion operator
e	Charge of an electron
$\tilde{\mathrm{E}}(t)$	Complex electric field of the train of pulses in the time domain
$\tilde{\mathrm{E}}(\omega)$	Complex electric field of the train of pulses in the frequency domain
f	Focal length
f_{beat}	RF beatnote between two CNFL combs
f_{r}	Pulse repetition frequency
f_0	Carrier envelope frequency
$g_{\mathrm{m}}(\omega)$	Atomic gain coefficient
$G_{dB}(\omega)$	Power gain in decibels (dB)
G_0	Small signal gain
h	Small step size in SSFM
$\hbar$	Planck constant
i	Imaginary number ($i = \sqrt{-1}$)
I_{sat}	Saturation intensity
k_0	Propagation constant in vacuum
L_{D}	Dispersion length
L_{NL}	Nonlinear length
m_e	Mass of an electron

n	Index of refraction
n_2	Nonlinear index of refraction
n_{core}	Index of refraction of a core
n_{clad}	Index of refraction of a cladding
n	Mode number
N_{g}	Group index
N_{s}	Soliton order
$\hat{N}$	Nonlinear operator
$\tilde{P}(\text{r},\omega)$	Total polarization in the intense electric filed
P_0	Initial peak power
R	Resistance
$\text{S}_v(f)$	Frequency power spectral density
$\text{S}_\phi(f)$	Phase power spectral density
T_r	Cavity round trip time
T_0	Initial temporal pulse duration
U_{sat}	Saturation energy
v_{g}	Group velocity
v_{p}	Phase velocity
V	V number
$w(z)$	Beam waist
w_0	Beam waist at the focal point
z_{R}	Rayleigh range
α	Decaying constant
α_0	Material loss
β	Propagation constant in a medium
β_2	Second order dispersion (Group velocity dispersion)
β_3	Third order dispersion
$\Delta\beta_{\text{m}}(\omega)$	Atomic gain disperison
$\tilde{\chi}_{at}(\omega)$	Atomic susceptibility

$\chi'(\omega)$	Real part of atomic susceptibility
$\chi''(\omega)$	Imaginary part of atomic susceptibility
$\chi^{(3)}$	Third order susceptibility
$\delta\omega$	Frequency chirp
Δ	Normalized index difference
ε_0	Electric permittivity in vacuum
$\Delta\varphi$	Phase slip between pulses
Λ	Poling period
λ	Wavelength
λ_c	Center wavelength (or carrier wavelength)
λ_0	Zero dispersion wavelength
μ	Magnetic permeability in a medium
σ	Transition cross section
ν	Frequency
ν_n	n^{th} comb tooth
ν_{fix}^{X}	Fixed point frequency related to a variable, X
ν_{3dB}	Laser 3 dB roll-off frequency
γ	Effective nonlinearity
τ	Averaging time in second
τ_{eff}	Effective recovery time
ω_c	Carrier angular frequency
ω_a	Atomic resonant angular frequency
$\Delta\omega_a$	Width of resonant angular frequency
$\Delta\omega_{3dB}$	Full width half maximum of the gain narrowing bandwidth

Appendix B - Abbreviations

AC	Intensity attocorrelation
AM	Amplitude modulation
ASE	Amplified spontaneous emission
dB	Decibel
BPF	Band pass filter
CEO	Carrier envelope offset
CNFL	Carbon nanotube fiber laser
CW	Continuous wavelength
DCF	Dispersion compensation fiber
EDF	Erbium doped fiber
EDFA	Erbium doped fiber amplifier
ESA	Electric spectrum analyzer
FBG	Fiber Bragg grating
FFT	Fast Fourier transformation
FWHM	Full width half maximum
F8L	Figure eight laser
GPS	Global positioning system
GVD	Group velocity dispersion
HNFL	Highly nonlinear fiber
IR	Infrared
LD	Laser diode
LP	Linearly polarized
MFD	Mode field diameter
NA	Numerical aperture
NALM	Nonlinear amplifying loop mirror
NLSE	Nonlinear Schrödinger equation
NPR	Nonlinear polarization rotation
P-APM	Polarization additive pulse mode-locking
PBGF	Photonic bandgap fiber

PCF	Photonic crystal fiber
PD	Photodetector
PLC	Phase-lead compensation
PLL	Phase lock loop
PPLN	Periodically poled lithium niobate
PSD	Power spectral density
PZT	Piezo-electric transducer
RF	Radio frequency
RBW	Resolution bandwidth
RIN	Relative intensity noise
RIN_p	Relative intensity noise of a pump laser
SAS	Saturated absorption spectroscopy
SBR	Semiconductor Bragg reflector
SESAM	Semiconductor saturable absorber mirror
SHG	Second harmonic generation
SMF	Single mode fiber
SNR	Signal to noise ratio
SPM	Self phase modulation
SRS	stimulated Raman scattering
SS	Self steepening
SSFM	Split step Fourier method
SSG	Small signal gain
SWCNT	Single walled carbon nanotube
TIR	Total internal reflection
TL	Transform-limited
TOD	Third order dispersion
WDM	Wavelength division multiplexer
XPM	Cross phase modulation

Appendix C - Derivation of the Nonlinear Schrödinger Equation

The nonlinear Schrödinger equation (NLSE) can be derived from the Maxwell's equation. Here we are assuming the paraxial pulse propagation of the fundamental linearly polarized (LP) mode in a fiber, so that the transverse component of the electric field is ignored. Another assumption is that the dispersion and nonlinearity is small enough and therefore the contribution of the high order dispersion terms and the high order nonlinearity terms are insignificant. Hence the group velocity dispersion (GVD) and self phase modulation (SPM) are only considered in this derivation. One can see Ref. [147] for more detailed discussion about NLSE.

A complex electric field $\tilde{A}(z,t)$ is defined as

$$\tilde{A}(z,t) = A_0(z,t)\,\mathrm{e}^{i(\omega_c t-\beta(\omega_c)z+\varphi_0)}, \tag{A.1.1}$$

where $A_0(z,t)$ is the pulse envelope of the complex electric field and φ_0 is the initial temporal phase of the pulse. Here we set $\varphi_0 = 0$. The tilde was used to stand for the complex electric field. z is the propagation axis and ω_c is the carrier angular frequency. The Fourier transformation of Eq. (A.1.1)

$$\tilde{A}(z,\omega) = \int_{-\infty}^{\infty} \tilde{A}(z,t)\,\mathrm{e}^{-i\omega t}\,dt, \tag{A.1.2}$$

where E(z,ω) is the electric field in the frequency domain. Therefore Eq. (A.1.2) becomes

$$\tilde{A}(z,\omega) = \int_{-\infty}^{\infty} A_0(z,t')\,\mathrm{e}^{-i(\omega-\omega_c)t'}\,\mathrm{e}^{-i\beta(\omega_c)z}\,dt' \tag{A.1.3}$$

For a small increment (dz) in propagation length, the electric field in the frequency domain is that

$$
\begin{aligned}
\tilde{A}(z+dz,\omega) &= \tilde{A}(z,\omega)\,\mathrm{e}^{-i\beta(\omega)dz} \\
&= \left[\int_{-\infty}^{\infty} A_0(z,t')\,\mathrm{e}^{-i(\omega-\omega_c)t'}\,\mathrm{e}^{-i\beta(\omega_c)z}\,dt'\right]\mathrm{e}^{-i\beta(\omega)dz} \\
&= \int_{-\infty}^{\infty} A_0(z,t')\,\mathrm{e}^{-i(\omega-\omega_c)t'}\,\mathrm{e}^{-i\beta(\omega_c)(z+dz-dz)}\,dt'\,\mathrm{e}^{-i\beta(\omega)dz} \\
&= \mathrm{e}^{-i\beta(\omega_c)(z+dz)}\int_{-\infty}^{\infty} A_0(z,t')\,\mathrm{e}^{-i(\omega-\omega_c)t'}\,\mathrm{e}^{-i\left[\beta(\omega)-\beta(\omega_c)\right]dz}\,dt'
\end{aligned}
\tag{A.1.4}
$$

Take the inverse Fourier transform and look at the electric field in the time domain then,

$$
\begin{aligned}
\tilde{A}(z+dz,t) &= \frac{1}{2\pi}\int_{-\infty}^{\infty}\tilde{A}(z+dz,\omega)\mathrm{e}^{i\omega t}d\omega \\
&= \frac{1}{2\pi}\int_{-\infty}^{\infty} d\omega \mathrm{e}^{i\omega t}\left[\mathrm{e}^{-i\beta(\omega_c)(z+dz)}\right]\int_{-\infty}^{\infty} A_0(z,t')\mathrm{e}^{-i(\omega-\omega_c)t'}\mathrm{e}^{-i\left[\beta(\omega)-\beta(\omega_c)\right]dz}dt' \\
&= \frac{1}{2\pi}\mathrm{e}^{i\omega_c t}\mathrm{e}^{-i\beta(\omega_c)(z+dz)}\int_{-\infty}^{\infty} d\omega\left[\int_{-\infty}^{\infty} A_0(z,t')\mathrm{e}^{-i(\omega-\omega_c)t'}\mathrm{e}^{-i\left[\beta(\omega)-\beta(\omega_c)\right]dz}dt'\right]\mathrm{e}^{i(\omega-\omega_c)t} \\
&= \mathrm{e}^{i\left[\omega_c t-\beta(\omega_c)(z+dz)\right]}\,\frac{1}{2\pi}\int_{-\infty}^{\infty} d(\omega-\omega_c)\left[\int_{-\infty}^{\infty} A_0(z,t')\mathrm{e}^{i(\omega-\omega_c)(t-t')}\mathrm{e}^{-i\left[\beta(\omega)-\beta(\omega_c)\right]dz}dt'\right]
\end{aligned}
\tag{A.1.5}
$$

Carrier term **Envelope term**

Let us use the slow varying envelope approximation, then we just consider the envelope term and the complex envelope $\tilde{A}(z+dz,t)$ is defined as

$$
\begin{aligned}
\tilde{A}(z+dz,t) &= \frac{1}{2\pi}\int_{-\infty}^{\infty} d(\omega-\omega_c)\left[\int_{-\infty}^{\infty} A_0(z,t')\mathrm{e}^{i(\omega-\omega_c)(t-t')}\mathrm{e}^{-i\left[\beta(\omega)-\beta(\omega_c)\right]dz}dt'\right] \\
&= \frac{1}{2\pi}\int_{-\infty}^{\infty} d\Delta\omega\left[\int_{-\infty}^{\infty} A_0(z,t')\mathrm{e}^{i\Delta\omega(t-t')}\mathrm{e}^{-i\Delta\beta dz}dt'\right]
\end{aligned}
\tag{A.1.6}
$$

where $\Delta\beta = \beta(\omega)-\beta(\omega_c)$ and $\Delta\omega = \omega-\omega_c$. Further simplification can be done by letting $z = z'+dz$, then Eq. (A.1.6) is rewritten as

$$
\tilde{A}(z,t) = \frac{1}{2\pi}\int_{-\infty}^{\infty} d\Delta\omega\left[\int_{-\infty}^{\infty} A_0(z,t')\mathrm{e}^{i\Delta\omega(t-t')}\mathrm{e}^{-i\Delta\beta(z-z')}dt'\right] \tag{A.1.7}
$$

Now one can take a derivative of Eq (A.1.7) with respect to z, then

$$\frac{\partial}{\partial z}\tilde{A}(z,t) = -i\Delta\beta\tilde{A}(z,t) \tag{A.1.8}$$

Suppose that both dispersion and Kerr effect are weak, then β is written as

$$\beta(\omega, I) = \beta_0(\omega_c) + \beta_1(\omega_c)\Delta\omega + \frac{1}{2}\beta_2(\omega_c)\Delta\omega^2 + \gamma I(z,t) \tag{A.1.9}$$

where γ is the effective nonlinear coefficient and I is the intensity defined as $|A|^2$. Then Eq. (A.1.8) becomes

$$\begin{aligned}\frac{\partial}{\partial z}\tilde{A}(z,t) &= -i\Delta\beta\tilde{A}(z,t) \\ &= -i\tilde{A}(z,t)\left[\beta_1\Delta\omega + \frac{1}{2}\beta_2\Delta\omega^2 + \gamma I(z,t)\right] \\ &= \tilde{A}(z,t)\left[-\beta_1\frac{\partial}{\partial t} + i\frac{\beta_2}{2}\frac{\partial^2}{\partial t^2} - i\gamma I(z,t)\right]\end{aligned} \tag{A.1.10}$$

where $\frac{\partial}{\partial t} = i\Delta\omega$ and $\frac{\partial^2}{\partial t^2} = -\Delta\omega^2$. Therefore, the nonlinear Schrödinger equation is derived.

$$\frac{\partial\tilde{A}}{\partial z} + \beta_1\frac{\partial\tilde{A}}{\partial t} - i\frac{\beta_2}{2}\frac{\partial^2\tilde{A}}{\partial t^2} + i\gamma|A|^2\tilde{A} = 0 \tag{A.1.11}$$

Appendix D - Derivation of the Third Order Dispersion

Typically fiber manufacturers provide $D(\lambda)$ and D_{slope} ($dD/d\lambda$) but we use β_2 (GVD) and β_3 (TOD) for numerical simulations. Therefore the dispersion parameter should be changed into the forms of β_2 and β_3. Especially the consideration of TOD is required for pulse compensation using the hollow core photonic bandgap fiber (HC-PBGF) because HC-PBGF has the relatively large TOD and affects the shape of the compressed pulse. Here we will show the derivation of the TOD (β_3). From Eq. (2.8), the dispersion parameter (D) is

$$D(\lambda) \equiv \frac{1}{c}\frac{dN_g}{d\lambda} = -\frac{2\pi c}{\lambda^2}\frac{d^2\beta}{d\omega^2}.$$

Take a derivative Eq. (2.8) with respect to λ. Then D_{slope} is derived as

$$\begin{aligned} D_{slpoe} &= \frac{dD(\lambda)}{d\lambda} = -\frac{d}{d\lambda}\left[\frac{2\pi c}{\lambda^2}\frac{d^2\beta}{d\omega^2}\right] \\ &= \frac{4\pi c}{\lambda^3}\frac{d^2\beta}{d\omega^2} - \frac{2\pi c}{\lambda^2}\frac{d}{d\lambda}\left(\frac{d^2\beta}{d\omega^2}\right) \\ &= \frac{4\pi c}{\lambda^3}\frac{d^2\beta}{d\omega^2} - \frac{2\pi c}{\lambda^2}\frac{d}{d\omega}\left(\frac{d^2\beta}{d\omega^2}\right)\frac{d\omega}{d\lambda} \\ &= \frac{4\pi c}{\lambda^3}\frac{d^2\beta}{d\omega^2} + \frac{4\pi^2 c^2}{\lambda^4}\left(\frac{d^3\beta}{d\omega^3}\right). \end{aligned} \tag{B.1.1}$$

So D_{slope} at λ_0 is that

$$D_{slope}\Big|_{\lambda=\lambda_c} = \frac{4\pi c}{\lambda_c^{\,3}}\beta_2 + \frac{4\pi^2 c^2}{\lambda_c^4}\beta_3. \tag{B.1.2}$$

Therefore, β_3 is derived from Eq. (B.1.2) as

$$\beta_3 = \frac{\lambda^4}{4\pi^2 c^2}\left(D_{slope} + \frac{2}{\lambda} D \right). \qquad \text{(B.1.3)}$$

Appendix E - Power Spectral Density and Quantification of Noise

For many stabilization experiments, one desires to have a pure single frequency source. However, even for a very good synthesizer, noise exists. The noise of frequency source can be quantified by the power spectral density (PSD). The PSD shows the power of noise sources per unit Hertz. Therefore the integration of PSD provides total power produced by noise. Mathematically, the PSD can be represented by

$$S(\nu) = \lim_{t\to\infty} \frac{1}{T} \left\langle \left| \int_{-T/2}^{T/2} V(t) e^{i2\pi\nu t} dt \right|^2 \right\rangle, \tag{C. 1}$$

which is the time average of the Fourier transform of an arbitrary signal. $V(t)$ denotes the signal we want to measure and it is defined as

$$V(t) = \left[V_0 + \varepsilon(t)\right] \sin\left[2\pi\nu_0 t + \phi(t)\right], \tag{C. 2}$$

where V_0 = nominal peak output voltage

$\varepsilon(t)$ = amplitude deviation

ν_0 = nominal frequency

$\phi(t)$ = phase deviation

and the frequency and the phase have the relationship written as

$$\nu(t) = \nu_0 + \frac{1}{2\pi} \frac{d\phi(t)}{dt}. \tag{C. 3}$$

The PSD can experimentally be measured with a fast Fourier transform (FFT) spectrum analyzer. In the case of the stabilization of our frequency comb, both f_r and f_0 should be stabilized to the local oscillators (or called the frequency synthesizer). The difference between f_0 (or f_r) and a local oscillator is created due to either noise in the comb or noise in the local

oscillator. The PSD shows possible noise sources in the Fourier frequency domain. The unit of the PSD of frequency noise is Hz^2/Hz which represents the frequency noise per unit Hz. The square in the unit is related to the power signal (P) we measure ($P=V^2/R$, where R: Resistance).

Appendix F - Arc Fusion Splicer Program Parameter for HNFL

The Ti:Sapphire laser uses a photonic crystal fiber (PCF). In practice, the pulse is coupled into the PCF in the free space. This method has problems that the beam pointing undergoes fluctuation by technical noise and degrades the reliability for the supercontinuum (SC) generation. Contrary to that for Er^{3+} doped fiber lasers, the SC can be generated by directly splicing a SMF-28e to the highly nonlinear fiber (HNFL) using a commercial arc fusion splicer (Ericsson FSU-995FA). The loss is typically less than 1.5 dB but 0.2 dB loss is possible using the recipe here. This makes the SC generation stable and reliable and allows very simple experimental set-up.

The low loss splicing between HNFL and SMF-28e

Prefuse time: 0.2 sec

Prefuse curr: 10.0 mA

Gap: 50.0 μm

Overlap: 12.0 μm

Fusion time 1: 0.3 sec

Fusion curr 1: 10.5 mA

Fusion time 2: 30.0 sec

Fusion curr 2: 14.0 mA

Fusion time 2: 0.0 sec

Fusion time 3: 0.0 mA

Data sheet of highly nonlinear fiber (OFS)

External ID	Unit	7160467001
Dispersion @ 1550 nm	ps/(nm-km)	4.94
Dispersion slope @ 1550 nm	ps/(nm^2-km)	0.022
Attenuation @ 1550 nm	dB/km	0.94
Cut-off wavelength	nm	1220
Effective area	μm^2	12.2
Effective nonlinearity (γ)	$(W\text{-}km)^{-1}$	10.9

Appendix G - MATLAB Codes for Pulse Propagation in Er^{3+} Doped Fiber Amplifiers

The "F8L_EDFA_thesis.m" code is used to simulate the pulse propagation in the EDFA in Sec. 4.1.3.4. The normalized gain shape is imported from the experimentally measured data. The gain shape can also be created by the code, "absorption_emission_creator.m". This code generates a gain function which is the sum of multiple Lorentzians since the erbium doped fiber gain medium has multiple resonance frequencies. The "ssfm_et_gain_spm_Er110_F8L*.m" is used to solve the ultashort pulse propagation in the EDFA using the split step Fourier method. The possible pulse gain is experimentally measured and the gain coefficient ($g(\omega)$) can be calculated from the equation, $g(\omega)=\ln G(\omega)/2L$, where $G(\omega)$ is the measured gain (ratio of input power and out power) and L is the length of EDF in the amplifier.

F8L_EDFA_thesis.m

```
% Split-Step Fourier Method: Modeling of Er3+ doped fiber laser amplifier system
% version 3.0, by JKL 10/20/2010
% Program solves the NLSE for the pulse propagation through an EDFA.
<Four sections>
% 1) Pre-chirp SMF28
% 2) Pre-chirp Flexcore 1060
% 3) EDF (Er110-Liekki)
% 4) Post-chirp SMF28

% Unit of time : fs
% Unit of wavelength/length : nm
% Unit of power : W
% Unit of energy : fJ

clear all;
close all;
```

```
% Define general parameters
c=300;                                  % c=300 nm/fs
l0=1569;                                % Center wavelength 1569 nm
w0=(2*pi*c)/l0;                         % Center frequency
% Define array parameters and time/freq. arrays
num=2^12;                               % # points in fft array: 2^12
range=40000;                            % time range/window in fs, 40000
dt=range/num;                           % temporal increment
dw=2*pi/range;                          % spectral increment
time=((1:num)-(num/2))*dt;              % time array
freq=((1:num)-(num/2))*dw;              % frequency array
wave=2*pi*c./(freq+w0);                 % wavelength array
dl=2*pi*c*dw/w0^2;                      % wavelength increment
% DEFINE FIBER PARAMETERS

% Fiber #1: SMF28
n2=(3*10^-20)*10^18;                    % n2 for fused-silica
r0_smf28=10400/2;                       % mode field radius in nm, physical diameter of 10400 nm
aeff_smf28=pi*r0_smf28^2;               % effective core area, 84.95 um^2
g_smf28=n2*w0/(c*aeff_smf28);           % effective nonlinearity in unit of 1/(W nm), 1.43 1/(W km)
D_smf28=corning_smf28(l0)*10^-9;        % dispersion parameter in fs/nm-nm, 17.3493 ps/km-nm
dDdl=0.092;                             % disperion slope parameter in fs/nm^2-nm
b2_smf28=-(l0.^2/(2.*pi.*c)).*D_smf28;  % beta2 (fs^2/nm), -22.113 ps^2/km
b3_smf28=0*1.38e-4;                     % beta3 (fs^3/nm) 1.38e-4 fs^3/nm
a0=0*4.600*10^-14;                      % 0.2 dB/km
disop_smf28=dop(freq,b2_smf28,b3_smf28,0,0,0,0,a0);      % compute dispersion operator

% Fiber #2: Er110-Liekki
r0_EDF=6500/2;                          % mode field radius in nm, mfd 6500 nm for Liekke Er110
aeff_EDF=pi*r0_EDF^2;                   % core area
g_EDF=n2*w0/(c*aeff_EDF);               % effective nonlinearity in unit of 1/(W nm)
[b2_EDF,b3_EDF,b4_EDF,b5_EDF,b6_EDF,b7_EDF]=Liekke_EDF_bcoeff(w0);      % beta2 (fs^2/nm)
b3_EDF=0*5.6907e-5;                     % beta3 (fs^3/nm) 5.6907e-5 fs^3/nm
a0=0*4.600*10^-14;                      % 0.2 dB/km
disop_EDF=dop(freq,b2_EDF,b3_EDF,0,0,0,0,a0);            % compute dispersion operator
```

```
% EDF GAIN PARAMETERS
% importgain=1: Import normalized wavelength dependent gain

importgain=1;                                   % import EDF gain spectrum
if importgain==1,
        fn='C:\Documents and Settings\jinkang lim\My Documents\_Laboratory Items\2_MATLAB
        CODES\ssfm_code\EDF_dispersion\wavelength_dep_gain3.dat';
    data=dlmread(fn,',');                       % read rows and columns
    absfreq_data=data(:,2)';                    % choose second columns
    freq_data=absfreq_data-w0;                  % Center frequency of gain function was subtracted
    gain_data=data(:,3)';
    f_gain=interp1(freq_data,gain_data,freq,'linear',0);    % interpolate spectrum data
    malpha_Er110=(log(15)*(1/(2*1.00))*10^-9).*f_gain;  % G(w)=exp[2g(w)L] => g(w)=lnG(w)/2L
        d_beta=0;                                   % gain induced dispersion
  else
    [N1,N2,Amp_ab1,Amp_ab2,Amp_ab3,Amp_ab4,Amp_em1,Amp_em2,Amp_em3,Amp_em4,...
        wa_ab1,wa_ab2,wa_ab3,wa_ab4,dwa_ab1,dwa_ab2,dwa_ab3,dwa_ab4,...
        wa_em1,wa_em2,wa_em3,wa_em4,dwa_em1,dwa_em2,dwa_em3,dwa_em4,p,q,d_beta,malpha]=abs
        orption_emission_creator*(freq,w0,c);           % Create a gain using mulitple lorentzians
end

% Fiber #3: Flexcore 1060
r0_flex=6200/2;                 % mode field radius in nm, MFD=6.2 for Corning HI1060
aeff_flex=pi*r0_flex^2;         % core area
g_flex=n2*w0/(c*aeff_flex);     % effective nonlinearity in unit of 1/(W nm)
b2_flex=-4.5*10^-6;             % beta2 (fs^2/nm), -4.5 ps^2/km from JILA, -7 ps^2/km from Tamura
% b2_flex=-7*10^-6;
a0=0*4.600*10^-14;              % 0.2 dB/km
disop_flex=dop(freq,b2_flex,b3_flex,0,0,0,0,a0);  % compute dispersion operator

% Parameters for Raman Response Function
t1=12.2;                % Raman response time 1
t2=32.0;                % Raman response time 2
Ram=hR_t(time,t1,t2);           % Import Raman response, same for all fibers
```

```
% GENERATE INPUT ELECTRIC FIELD
% First determine Dto of pulse with spectral width of Dlo
% Assume a transform-limited pulse
% OR, use imported spectrum and assume a transform-limited pulse
% Signal Pulse Parameters
T=(1/(56.57*10^6))*10^15;          % 1/Repetition rate (56.57 MHz)
phi2=0;                            % Pulse phase distortion, 0
phi3=0;                            % Pulse phase distortion, 0
Paveo=0.011;                       % Initial average Power, 10 mW

generate_spectrum=0;
if generate_spectrum==1,                          % generate sech^2 spectrum with possible chirp
   Dlo=12.2;                                      % Pulse spectral FWHM 14.2 in nm
   [Eto,Ito,pto,Ewo,Iwo,pwo]=sech_et_chirped(time,freq,Dlo,l0,1,0,0);
   Dto=fwhm(time,Ito);
   P_TL=(Paveo*(T/Dto))/1.134;                    % transform-limited peak power from average power
   [Eto,Ito,pto,Ewo,Iwo,pwo]=sech_et_chirped(time,freq,Dlo,l0,P_TL,phi2,phi3);
   Ilo=(2.*pi.*c./wave.^2).*Iwo;                  % resize bin from frequency to wavelength
   Po=max(Ito);                                   % Initial power
   Eno=sum(Eto.*conj(Eto)).*dt;
else
      fn='C:\Documents and Settings\jinkang lim\My Documents\_Laboratory Items\2_MATLAB
      CODES\ssfm_code\input_fields\F8L_spec_123107.dat';          % import spectrum
   data=dlmread(fn,',');
   absfreq_data=data(:,2)';
   freq_data=absfreq_data-w0;
   Iw_data=data(:,3)';
   Iwo=interp1(freq_data,Iw_data,freq,'linear',0);                % interpolate spectrum

   % create field with correct peak power
   Eto=fftshift(ifft(fftshift(sqrt(Iwo))));
   Dto=fwhm(time,Eto.*conj(Eto));
   Po=(Paveo*(T/Dto))/1.134;
   Eto=sqrt(Po).*(Eto./max(Eto));                        % time domain with correct peak power
   [Ito,pto,Iwo,pwo,Ilo]=intensity_n_phase(freq,wave,Eto,w0);
   Po=max(Ito);
```

```
   Eno=sum(Eto.*conj(Eto)).*dt;
end

-----------------------------------------------------------------------------------------------------------------------------------
% MAIN SSFM PROGRAM
-----------------------------------------------------------------------------------------------------------------------------------
disp(sprintf('SSFM simulation of pulse propagation thru the amplifer'))
disp(sprintf('Initial Peak Power = %0.5g W, Initial Average Power= %0.5g W, Pin/Psat : %0.5g',Po,Paveo))

tot_cputime=0;
Dtall=[];
Pall=[];
% try to do 2000 steps per meter, h=500000 nm or h=5e-4 m or h=0.5 mm
h=10^9/2000;

% Section 1: pre-chirp smf28, length 0.42 m
len1=1*0.42*10^9;                          % pre-chirp fiber length of smf28
numsteps1=len1/h;                          % determine # of steps
disp(sprintf('Section 1: Pre-chirp smf28, length %0.5g m, stepsize %0.5g m',len1/10^9,h/10^9))
[At,Dtall,Pall,cputime]=ssfm_et_spm(time,Eto,disop_smf28,w0,g_smf28,Ram,dt,h,numsteps1,freq,Dtall,Pall);
tot_cputime=tot_cputime+cputime;

% Section 2: prechirp flexcore 1060, length 0.51 m
len2=1*0.51*10^9;                          % pre-chirp fiber length of flexcore 1060
numsteps2=len2/h;                          % determine # of steps
disp(sprintf('Section 2: Pre-chirp flexcore, length %0.5g m, stepsize %0.5g m',len2/10^9,h/10^9))
[At,Aw,Dtall,Pall,cputime]=ssfm_et_spm_pre_JK(time,At,disop_flex,w0,g_flex,Ram,dt,dw,h,numsteps2,freq,
Dtall,Pall);
tot_cputime=tot_cputime+cputime;

% Section 3: EDF, length 1.0 m
len3=1*1.0*10^9;                           % Er110 length
numsteps3=len3/h;                          % determine # of steps
disp(sprintf('Section 3: EDF, length %0.5g m, stepsize %0.5g m',len3/10^9,h/10^9))
[At,Dtall,Pall,cputime]=ssfm_et_gain_spm_Er110_F8L*(time,At,Aw,disop_EDF,w0,g_EDF,dt,dw,h,numsteps3
,freq,Ram,d_beta,malpha_Er110,Po,Dtall,Pall);
tot_cputime=tot_cputime+cputime;
```

```
% Section 4 : postchirp flexcore 1060
len4=0*0.49*10^9;                          % post-chirp fiber length of flexcore 1060
numsteps4=len4/h;                          % determine # of steps
disp(sprintf('  Section 4: Post-chirp flexcore, length %0.5g m, stepsize %0.5g m',len4/10^9,h/10^9))
[At,Dtall,Pall,cputime]=ssfm_et_spm_post_JK(time,At,disop_flex,w0,g_flex,Ram,dt,h,numsteps4,freq,Dtall,P
all);
tot_cputime=tot_cputime+cputime;

% Section 5: post-chirp smf28, 0.57 m
len5=1*0.57*10^9;                          % post-chirp fiber length of smf28
numsteps5=len5/h;                          % determine # of steps
disp(sprintf('Section 5: Post-chirp smf28, length %0.5g m, stepsize %0.5g m',len5/10^9,h/10^9))
[At,Dtall,Pall,cputime]=ssfm_et_spm_post_JK(time,At,disop_smf28,w0,g_smf28,Ram,dt,h,numsteps5,freq,Dt
all,Pall);
tot_cputime=tot_cputime+cputime;

% Section 6: post-chirp PBG, length 0 m
len6=0*0.125*10^9;                         % post-chirp fiber length of PBG
numsteps6=len6/h;                          % determine # of steps
disp(sprintf('Section 6: Post-chirp PBG fiber, length %0.5g m, stepsize %0.5g m',len6/10^9,h/10^9))
[At,Dtall,Pall,cputime]=ssfm_et_spm_post_JK(time,At,disop_PBG,w0,g_PBG,Ram,dt,h,numsteps6,freq,Dtall,
Pall);
tot_cputime=tot_cputime+cputime;

% Final Length
totlen=(len1+len2+len3+len4+len5+len6)./10^9;    % total fiber length in meters

z=(([1:length(Dtall)]).*(5*h./10^9));      % need 5h since Dt is taken every fifth step
zrt=z./totlen;

% Final Fields
[It,pt,Iw,pw,Il]=intensity_n_phase(freq,wave,At,w0);
P=max(It);                                 % final peak power
ACIto=autocorr(Ito);                       % initial intensity autocorrelation
ACIt=autocorr(It);                         % final intensity autocorrelation
Dt=fwhm(time,It);                          % final pulse width
Pave=P*(sum(It./max(It).*dt))/T;           % final average power
```

```
%-------------------------------------------------------------------------------------------------------------------------------
% RESULTS:
%-------------------------------------------------------------------------------------------------------------------------------
% Peak Power Results
disp(sprintf(' '))
disp(sprintf('Initial Peak Power: %0.5g W',Po))
disp(sprintf('Final Peak Power: %0.5g W',P))
disp(sprintf('Peak Power Gain: %0.5g ',10.*log10(P/Po)))
% Peak Power Results
disp(sprintf(' '))
disp(sprintf('Initial Average Power: %0.5g W',Paveo))
disp(sprintf('Final Average Power: %0.5g W',Pave))

% Energy results
Eno=sum(Ito).*dt; % initial energy, Here sum*dt means integral of area
Enf=sum(It).*dt;  % final energy
disp(sprintf(' '))
disp(sprintf('Initial Energy: %0.5g fJ',Eno))
disp(sprintf('Final Energy: %0.5g fJ',Enf))
disp(sprintf('Energy Gain: %0.5g ',10.*log10(Enf/Eno)))          % 10*log10(Enf/Eno) -> convert energy gain into log scale
% AC resutls
disp(sprintf(' '))
disp(sprintf('Initial AC FWHM: %0.5g fs',fwhm(time,ACIto)))          % Initial AC trace widths
disp(sprintf('Final AC FWHM: %0.5g fs',fwhm(time,ACIt)))             % Final AC trace widths
disp(sprintf(' '))

% Plot temporal and spectral changes
plotresults=1;
if plotresults==1,
   figure(1);
   plot(time,Ito)
   axis([-500,500,0,1.5*max(Ito)])
   xlabel('Time (fs)','FontSize',17,'FontName','times');
   ylabel('Initial Temporal Intensity','FontSize',17,'FontName','times');
   figure(2)
   plot(wave,Ilo)
```

```
axis([1500,1600,0,1.5*max(Ilo)])
xlabel('Wavelength (nm)','FontSize',17,'FontName','times');
ylabel('Initial Spectral Intensity','FontSize',17,'FontName','times');
figure(3)
plotyy(time,It,time,pt)
xlabel('Time (fs)','FontSize',17,'FontName','times');
ylabel('Final Temporal Intensity','FontSize',17,'FontName','times');
figure(4)
plot(wave,Il)
axis([1400,1700,0,max(Il)])
xlabel('Wavelength (nm)','FontSize',17,'FontName','times');
ylabel('Final Spectral Intensity','FontSize',17,'FontName','times');
figure(5)
plot(time,Ito./max(Ito),time,It./max(It))
axis([-1000,1000,0,1.5*1])
xlabel('Time (fs)','FontSize',17,'FontName','times');
ylabel('Final Normalized Temporal Intensity','FontSize',17,'FontName','times');
figure(6)
plot(wave,Ilo./max(Ilo),wave,Il./max(Il))
axis([1400,1800,0,1.1])
xlabel('Wavelength (nm)','FontSize',17,'FontName','times');
ylabel('Final Normalized Spectral Intensity','FontSize',17,'FontName','times');
figure(7)
plot(time,ACIto,time,ACIt);
axis([-2000,2000,0,1.5*1])
xlabel('Time (fs)','FontSize',17,'FontName','times');
ylabel('Final Normalized Intensity Autocorrelation','FontSize',17,'FontName','times');
figure(8)
plot(wave,10.*log10(Ilo/max(Ilo)),wave,10.*log10(Il/max(Il)));
axis([1400,1800,-50,5])
xlabel('Wavelength (nm)','FontSize',17,'FontName','times');
ylabel('Spectral Intensity (dB)','FontSize',17,'FontName','times');
figure(9)
[AX,H1,H2]=plotyy(z,Dtall,z,10.*log10(Pall./Po));
line(ones(1,501).*len1.*10^-9,[0:500],'Color','r','LineWidth',2)
line(ones(1,501).*(len1+len2).*10^-9,[0:500],'Color','r','LineWidth',2)
line(ones(1,501).*(len1+len2+len3).*10^-9,[0:500],'Color','r','LineWidth',2)
```

```
    line(ones(1,501).*(len1+len2+len3+len4).*10^-9,[0:500],'Color','r','LineWidth',2)
    line(ones(1,501).*(len1+len2+len3+len4+len5).*10^-9,[0:500],'Color','r','LineWidth',2)
    xlabel('Propagation Distance (m)');
    set(get(AX(1),'Ylabel'),'String','Temporal FWHM (fs)')
    set(get(AX(2),'Ylabel'),'String','Peak Power Gain (dB)')
end
```

ssfm_et_gain_spm_Er110_F8L*.m

```
Version 1.0, Oct/09/2010 JKL
Generic main program that implements the Split-Step Fourier Method (SSFM)
The nonlinearity only includes SPM, incorporate gain per step

% units of time: fs
% units of wavelength/length: nm
% units of power : W

function[At,Dtall,Pall,cputime]=ssfm_et_gain_spm_Er110_F8L(time,At,Aw,dop,w0,g,dt,dw,h,numsteps,freq,
Ram,d_beta,malpha_Er110,Po,Dtall,Pall)

% Input:
% Eto is the initial complex electric field E(t)
% dop is the dispersion operator, which includes the fiber dispersion
% h is the step-size in nm
% w0 is the center angular frequency in 1/fs
% g is the effective nonlinearity in 1/(W nm)
% numstep is the # of steps
% Output:
% At temporal electric field
% Dtall, Pall, Pulse duration and peak power per step

tic;
```

```
----------------------------------------------------------------------------------------------------------------------------
% main program loop
----------------------------------------------------------------------------------------------------------------------------
% non-gain-saturated regime.
for s=1:numsteps,
        At=exp(h.*nop_spm_gain(At,w0,g,dt,Ram)).*At;
        Aw=fftshift(fft(fftshift(At)));
        Aw=exp(h.*dop).*Aw;
        Aw=exp(h.*malpha_Er110).*Aw;
        Aw=exp(h.*i.*d_beta).*Aw;                    % Assume d_beta=0
        At=fftshift(ifft(fftshift(Aw)));

    if mod(s,5)==0,
      It=At.*conj(At);
      Dti=fwhm(time,It);
      Dtall=[Dtall,Dti];
      Ppi=sum(At.*conj(At)).*dt;       % output pulse energy instead of power
      Pall=[Pall,Ppi];
      Iw=Aw.*conj(Aw);
      figure(1)
      plot(freq,Iw)
      axis([-0.1,0.1,0,max(Iw)+1])
           title('GAIN fiber section');
end

cputime=toc;
```

Note: Gray-shadowed codes can be found in Ref. [146] and gray-letter codes are not used for simulations.

Appendix H – Dispersion and Nonlinearity Values of Optical Fibers Used in This Thesis

We have evaluated the dispersion values and effective nonlinearity values at 1550 nm for fibers in our laboratory. It is very important to know those values in order to design mode-locked laser oscillators, fiber amplifiers, and pulse compression. The fibers are sorted by three groups such that gain fibers, step index fibers, and photonic bandgap fibers (PBGF).

EDF Fibers	Gain (dB/m)	D(ps/nm/km)	Dslope(ps/nm/nm/km)	β2(fs2/nm)	β3(fs3/nm)	MFD (μm)	γ(1/W km)
Liekki Er110	110	-8.9		1.14E-05		6.5	3.664
Liekki Er30	30	-9.8		1.25E-05		6.5	3.664
OFS LSL	17	-16.64		2.12E-05		5.2	5.726
Nurfern EDFL	15	-17.6		2.24E-05		5.5	5.118
OFS EDF80	80	-48		6.12E-05		4.3	8.374
OFS EDF150	150	-48		6.12E-05		4.3	8.374

Step Index Fibers	Gain (dB/m)	D(ps/nm/km)	Dslope(ps/nm/nm/km)	β2(fs2/nm)	β3(fs3/nm)	MFD (μm)	γ(1/W km)
SMF-28e		17.929	0.092	-2.29E-05	0.000187	10.4	1.431
HNLF(UNFO)		4.94	0.022	-6.30E-06	4.61E-05	3.9	10.1806
HNLF(LUMOS)		1.19	0.00818	-1.52E-06	1.58E-05	3.9	10.1806
HI1060		3.4	0.0534	-4.34E-06	9.40E-05	6.2	4.028

PBGF	Gain (dB/m)	D(ps/nm/km)	Dslope(ps/nm/nm/km)	β2(fs2/nm)	β3(fs3/nm)	MFD (μm)	γ(1/W km)
HC-1550		85.56	0.54	-1.09E-04	0.001056	10.2	0
Bath 5-25		20	0.3	-2.55E-05	0.000529	12	0

All dispersion values and effective nonlinearity values are evaluated at 1550 nm